

CONTROL OF INTERNAL LOOPS IN CONVERTERS OPERATING AS VIRTUAL SYNCHRONOUS MACHINES FOR IMPROVED DYNAMIC RESPONSE

Amiron Wolff dos Santos Serra

São Luís, Maranhão, Brazil 2025

Amiron Wolff dos Santos Serra

CONTROL OF INTERNAL LOOPS IN CONVERTERS OPERATING AS VIRTUAL SYNCHRONOUS MACHINES FOR IMPROVED DYNAMIC RESPONSE

Doctoral Thesis submitted to the Coordination of the Graduate Program in Electrical Engineering at the Federal University of Maranhão, as a partial requirement for the attainment of the Doctoral degree in Science in the field of Electrical Engineering.

Advisor: Prof. Dr. Luiz Antonio de Souza Ribeiro

Co-advisor: Prof. Dr. Mehdi Savaghebi

São Luís, Maranhão, Brazil

Ficha gerada por meio do SIGAA/Biblioteca com dados fornecidos pelo(a) autor(a). Diretoria Integrada de Bibliotecas/UFMA

Wolff dos Santos Serra, Amiron.

CONTROL OF INTERNAL LOOPS IN CONVERTERS OPERATING AS VIRTUAL SYNCHRONOUS MACHINES FOR IMPROVED DYNAMIC RESPONSE / Amiron Wolff dos Santos Serra. - 2025.

160 p.

Coorientador(a) 1: Mehdi Savaghebi Firoozabadi. Orientador(a): Luiz Antonio de Souza Ribeiro. Tese (Doutorado) - Programa de Pós-graduação em Engenharia Elétrica/ccet, Universidade Federal do Maranhão, Auditório do Instituto de Energia Elétrica Ufma, 2025.

1. Fontes Renováveis de Energia. 2. Inversores Formadores de Rede. 3. Máquina Síncrona Virtual. 4. Microrrede. 5. Malhas Internas de Controle. I. de Souza Ribeiro, Luiz Antonio. II. Savaghebi Firoozabadi, Mehdi.

Control of Internal Loops in Converters Operating as Virtual Synchronous Machines for Improved Dynamic Response

Amiron Wolff dos Santos Serra

Doctoral Thesis submitted to the Coordination of the Graduate Program in Electrical
Engineering at the Federal University of Maranhão, as a partial requirement for the attainment of
the Doctoral degree in Science in the field of Electrical Engineering.
Prof. Dr. Luiz Antonio de Souza Ribeiro, UFMA
(Advisor)
Prof. Dr. Mehdi Savaghebi, DTU
(Co-Advisor)
Member of the Thesis Committee:

Prof. Dr. Alexandre Cunha Oliveira, UFCG

Prof. Dr. Luís Guilherme Barbosa Rolim, UFRJ

Prof. Dr. José Gomes de Matos, UFMA

To my family, for their unconditional support.

ACKNOWLEDGEMENT

To God for the gift of life, and for guiding me during my PhD journey.

To my parents Amandio and Célia, for being my greatest supporters in the pursuit of knowledge, and for always going above and beyond to provide me with everything I needed, especially during difficult times. To you, my warmest and most heartfelt thanks. A special thanks to my family, especially Arthur, Conceição, and Pedro Lucas.

To my fiancée and future wife, Lívia, thank you so much for your companionship and care throughout all these years. You have witnessed all my achievements and have always supported me in moments when nothing seemed to make sense. Thank you for never letting me give up.

To my advisor, Professor Luiz Antonio, for his unwavering support since the outset of my Master's journey, for placing his trust in me, and for the invaluable teachings, guidance, and opportunities provided. I am also deeply grateful for the continuous support provided during the revision of this thesis. I am immensely grateful to you.

To my co-advisor, Professor Mehdi Savaghebi, thank you for trusting me to join your research group and for never sparing any effort to ensure that, during my time at DTU, I had the best possible working conditions. My most sincere thanks.

To the professors of the IEE, especially Professor José Gomes: Thank you for each lesson throughout all these years. Working with you has made me a better professional.

To my friends at IEE: Alyston Nascimento, César Augusto, Diego Leonardo, Hellen Souza, Hércules Araujo, Khristian Freitas, Luis Felipe, Nerval Santos, Rafael Quezada, Rodrigo Pereira, and Yury Damaceno. Thank you for the daily interactions, great conversations, and shared knowledge. You made this journey more enjoyable.

To UFMA, CAPES, DTU, and Equatorial Energia Group for the technical and financial support during the development of this research.

And finally, to all those who were not mentioned but who contributed in some way to the completion of this research.

Abstract

The increasing integration of renewable energy sources into modern power systems, driven by environmental concerns and the global pursuit of sustainable energy, has significantly transformed the power generation landscape. In this context, inverter-based resources have become essential for interfacing renewable energy sources with the grid. These inverter-based resources are typically controlled using either grid-following or grid-forming strategies. While grid-following inverters rely on phase-locked loops and require an external voltage source for synchronization, grid-forming inverters can independently establish voltage and frequency references, making them suitable for both grid-connected and islanded microgrid operations.

Among various grid-forming strategies, virtual synchronous machines stand out for their ability to emulate the inertial and damping behavior of traditional synchronous generators. This enables more robust system dynamics in grids with high renewable energy sources penetration and low inertia. Virtual synchronous machines-based inverters offer the capability to support voltage and frequency regulation while operating autonomously or in coordination with the main grid.

This thesis proposes the design and refinement of the inner control loops of a virtual synchronous machine-based inverter, aiming to enhance power system stability and dynamic response. Specifically, a current controller is developed to provide high bandwidth, attenuate LCL filter resonance, and improve disturbance rejection. A voltage controller with disturbance input decoupling is also introduced to improve the virtual synchronous machine dynamic response. With the designed inner control loops, the virtual synchronous machine exhibits enhanced dynamic performance when connected to the grid across a wide range of short circuit ratios, as well as during load variations in islanded mode. The virtual synchronous machine also exhibits improved performance when operating in a microgrid, both in coordination with a grid-following inverter and when running in parallel with another virtual synchronous machine.

In general, this thesis aims to improve the inner control loops of a virtual synchronous machine, enabling it to serve as an effective power control strategy in electrical systems that are increasingly dominated by inverter-based resources.

Keywords: Renewable Energy Sources, Grid-Forming Inverters, Virtual Synchronous Machine, Microgrid, Inner Control Loops.

Resumo

A crescente integração de fontes renováveis de energia aos sistemas elétricos modernos, impulsionada por preocupações ambientais e pela busca global por soluções sustentáveis, tem transformado significativamente o panorama da geração de energia. Nesse cenário, os recursos baseados em inversores tornaram-se essenciais para a conexão dessas fontes à rede elétrica. Tais recursos geralmente são controlados por estratégias do tipo seguidores de rede ou formadores de rede. Enquanto os inversores seguidores de rede dependem de malha de detecção de fase e requerem uma fonte externa de tensão para sincronização, os inversores formadores de rede são capazes de estabelecer de forma autônoma referências de tensão e frequência, sendo, portanto, adequados para operação tanto conectada à rede quanto isolada.

Dentre as estratégias de formadores de rede, destacam-se as máquinas síncronas virtuais por sua capacidade de emular o comportamento inercial e de amortecimento dos geradores síncronos convencionais. Essa característica permite uma resposta dinâmica mais robusta em sistemas com alta penetração de fontes renováveis e baixa inércia. Inversores baseados em máquinas síncronas virtuais são capazes de sustentar a regulação de tensão e frequência, tanto em operação autônoma quanto em coordenação com a rede principal.

Esta tese propõe o projeto e o aprimoramento das malhas internas de controle de um inversor baseado em máquina síncrona virtual, com o objetivo de melhorar a estabilidade do sistema elétrico e a resposta dinâmica. Especificamente, é desenvolvido um controlador de corrente com alta largura de faixa, capaz de atenuar a ressonância do filtro LCL e melhorar a rejeição a perturbações. Também é proposto um controlador de tensão com desacoplamento da entrada de perturbação, visando aprimorar a resposta dinâmica da máquina síncrona virtual. Com as malhas de controle internas projetadas, a máquina síncrona virtual apresenta desempenho dinâmico aprimorado quando conectada à rede, mesmo em uma ampla faixa de razões de curto-circuito, assim como durante variações de carga em modo isolado. A máquina síncrona virtual também demonstra melhor desempenho quando operando em uma microrrede, tanto em coordenação com um inversor seguidor de rede quanto em paralelo com outra máquina síncrona virtual.

De modo geral, esta tese busca aprimorar as malhas internas de uma máquina síncrona virtual, permitindo que ela atue como uma estratégia eficaz de controle de potência em sistemas elétricos cada vez mais dominados por recursos baseados em inversores.

Palavras-chave: Fontes Renováveis de Energia, Inversores Formadores de Rede, Máquina Síncrona Virtual, Microrrede, Malhas Internas de Controle.

LIST OF FIGURES

Figure 1-1 – Simplified representation of the IBR control technique. (a) grid-following	
forming	31
Figure 2-1 – Block diagram of the VISMA control	39
Figure 2-2 – Control Block Diagram of the IEPE Topology	40
Figure 2-3 – Electronic part of a Synchronverter without the controls	43
Figure 2-4 – Control block diagram of the Synchronverter	44
Figure 2-5 – Control block diagram of the KHI topology	46
Figure 2-6 – Control block diagram of the ISE laboratory topology	48
Figure 2-7 – SPC control block diagram	49
Figure 2-8 – Control block diagram of the VSG	51
Figure 2-9 – Control block diagram of the VSYNC topology	52
Figure 3-1— Single-phase equivalent circuit of the LCL filter	60
Figure 3-2 – Block diagram of the LCL filter model	60
Figure $3-3$ – Frequency response of the LCL filter ($ig(s)/vinv(s)$)	62
Figure 3-4 – Effect of increasing Rd on the frequency response of an LCL Filter	63
Figure 3-5 – Block diagram of ig control using the Notch filter	64
Figure 3-6 – Frequency response of the system with and without the Notch filter	64
Figure 3-7 – Block diagram of ig control using state feedback as active damping	65
Figure 3-8 – Frequency response of the system with and without ic feedback	66
Figure 3-9 – Equivalent circuit	67
Figure 3-10 – Plot of Req and Xeq as a function of frequency	68
Figure 3-11— Circuit for passivity analysis	70
Figure 3-12 – Equivalent impedance-admittance model	70
Figure 3-13 – ReVi ω as a function of ω	72

Figure 3-14 – ReYj ω as a function of ω with $T=4KTdelay2\pi 2L1$	73
Figure 3-15 – Bidirectional GFM converter topology	74
Figure 3-16 – Control block diagram of the current loop	75
Figure 3-17 – Open-loop frequency response of the LCL filter and the equivalent L filter	76
Figure 3-18 – Closed-loop block diagram used for controlling $ig\alpha\beta$.	77
Figure 3-19 – Frequency response of Gad(s).	79
Figure 3-20 – Block diagram simplifications to derive Zo(s)	80
Figure 3-21 – Frequency response of Zo(s) in four cases. (a) without CCFAD and CVD. (b) with CCFAD and CVD as a constant function. (c) with CFFAD and CVD as a lead-lag compensator.	
Figure 3-22 – Lab setup for obtaining experimental results.	85
Figure 3-23 – Step response of the current controller. (a) without lead compensation. (b) with lead compensation. Blue curve – current reference in α -axis (i α *), lilac curve – injected curre of phase 'b' (ib), yellow curve – error (e α)	87
Figure 3-24 – Injected current of phase 'b'. (a) Lg changes from 1 mH to 6 mH. (b) Lg change from 6 mH to 1 mH	
Figure 3-25 – THD of the injected current in the presence of voltage harmonics. (a) without	
Gcvd. (b) with Gcvd as a constant value. (c) with Gcvd as a lead-lag compensator	
lilac curve – injected current of phase 'b'.	93
Figure 3-27 – Control block diagram of the voltage loop.	94
Figure 3-28 – Root locus for the voltage control loop	95
Figure 3-29 – Closed-loop diagram to assess the effect of Gff(z)	96
Figure 3-30 – Bode magnitude plot of the loop gain with and without $Gff(z)$	97
Figure 3-31 – Virtual impedance implementation.	98
Figure 3-32 – APC and RPC loops.	99

Figure 3-33 – Voltage step responses (blue) and equivalent second-order function (c	orange) 101
Figure 3-34 – Small-signal model of the power control loops with VSM control	103
Figure 3-35 – Step responses of the active power.	103
Figure 3-36 – Capacitor voltage during a load variation: (a) without DID; (b) with	DID. Blue
curves – νcα *; Green curves – νcα: Yellow curves – error	106
Figure 3-37 – Injected active power, reactive power and current: (a) without DID; (b) with DID.
Green curves – P ; Blue curves – Q : Lilac curves – current. $SCR = 2.57$	108
Figure 3-38 – Injected active power, reactive power and current: (a) without DID; (
Green curves – P ; Blue curves – Q : Lilac curves – current. $SCR = 3.85$	110
Figure 3-39 – Injected active power, reactive power and current: (a) without DID; (b) with DID.
Green curves – P ; Blue curves – Q : Lilac curves – current. $SCR = 7.7$	111
Figure 3-40 – Injected active power, reactive power and current: (a) without DID; (b) with DID.
Green curves – P ; Blue curves – Q : Lilac curves – current. $SCR = 19.25$	112
Figure 4-1 – DC-link power flow with ideal conversion	115
Figure 4-2 – Block diagram of the DC-link voltage control	115
Figure 4-3 – Block diagram for IL control.	116
Figure 4-4 – Block diagram for Vdc control.	117
Figure 4-5 – Pe and Qe curves without the strategy – $SCR = 6.38$	119
Figure 4-6 – Pe and Qe curves with the strategy – $SCR = 6.38$.	120
Figure 4-7 – Pe and Qe curves without the strategy – $SCR = 12.76$	121
Figure 4-8 – Pe and Qe curves with the strategy – $SCR = 12.76$	122
Figure 5-1 – Microgrid schematic diagram	123
Figure 5-2 – (a) Injected current of the GFL inverter without Gcvd, operating in part	rallel with a
GFM inverter without Gcvd; (b) Zoomed-in view	124
Figure 5-3 – (a) Injected current of the GFL inverter with Gcvd, operating in parall	el with a
GFM inverter with Gcvd; (b) Zoomed-in view	125
Figure 5-4 – (a) Injected current of the GFM inverter without Gcvd, operating in pa	ırallel with a

GFL inverter without Gcvd; (b) Zoomed-in view.	126
Figure $5-5-(a)$ Injected current of the GFM inverter with Gcvd, operating in parallel with a GFL inverter with Gcvd; (b) Zoomed-in view.	
Figure 5-6 – Injected current of the GFL inverter without Gcvd during a voltage sag	128
Figure 5-7 – Injected current of the GFL inverter with Gcvd during a voltage sag	129
Figure 5-8 – Injected current of the GFM inverter during a voltage sag, with the GFL inverted operating without Gcvd	
Figure 5-9 – Injected current of the GFM inverter during a voltage sag, with the GFL inverted operating with Gcvd.	
Figure 5-10 – Active powers of the GFM inverters during parallel operation without DID	132
Figure 5-11 – Active powers of the GFM inverters during parallel operation with DID	132
Figure 5-12 – Total harmonic distortion of the current injected into the grid in one of the phase	
Figure 5-13 – Total harmonic distortion of the voltage at the PCC in one of the phases	134
Figure 5-14 – Total harmonic distortion of the current at the PCC in one of the phases	135
Figure B-1 – Full schematic of the experimental setup. Source: Author	157
Figure B-2 – Inverters used in the experimental setup.	158
Figure B-3 – L1, C of the LCL filter and grid impedance connectors	158
Figure B-4 – L2 and grid impedance inductors	159
Figure B-5 – DC voltage source.	159

LIST OF TABLES

Table 2-1 – Advantages and disadvantages of VISMA	39
Table 2-2 – Advantages and disadvantages of the IEPE Topology	41
Table 2-3 – Advantages and disadvantages of Synchronverter.	45
Table 2-4 – Advantages and disadvantages of KHI Topology	46
Table 2-5 – Advantages and disadvantages of the ISE laboratory topology	48
Table 2-6 – Advantages and disadvantages of the SPC	50
Table 2-7 – Advantages and disadvantages of the VSG	52
Table 2-8 – Advantages and disadvantages of the VSYNC topology	53
Table 2-9 – Summary of VSM emulation techniques.	54
Table 3-1 – LCL filter parameters.	61
Table 3-2 – Current Controller Gains.	77
Table 3-3 – Comparison of Maximum Closed-Loop Bandwidths With and Without Lead	
Compensation Under Different Switching Frequencies	<i>78</i>
Table 3-4 – System Parameters	86
Table 3-5 – Voltage Controller Gains	95
Table 3-6 – DID Control Gains.	97
Table 3-7 – System and Control Parameters.	104
Table 4-1 – System and Control Parameters for the DC-DC Converter.	117

LIST OF ABBREVIATIONS

AC Alternating Current

APC Active Power Controller

AVR Automatic Voltage Regulator

CCFAD Capacitor Current Feedback Active Damping

CVD Capacitor Voltage Decoupling

DC Direct Current

DG Distributed Generation

DID Disturbance Input Decoupling

DSP Digital Signal Processing

EMF Electromotive Force

EMS Energy Management System

ESR Equivalent Series Resistance

GFL Grid-Following

GFM Grid-Forming

IBR Inverter-Based Resource

IEPE Institute of Electrical Power Engineering

KHI Kawasaki Heavy Industries

LPF Low-Pass Filter

MPC Model Predictive Control

NERC	North American Electric Reliability Corporation
PCC	Point of Common Coupling
PI	Proportional Integral
PLC	Power Loop Controller
PLL	Phase-Locked Loop
PR	Proportional Resonant
PSC	Power Synchronization Control
PWM	Pulse Width Modulation
RES	Renewable Energy Sources
RPC	Reactive Power Controller
SOC	State of Charge
SPC	Synchronous Power Controller
SSG	Static Synchronous Generator
THD	Total Harmonic Distortion
UPS	Uninterruptible Power Supply
VOC	Virtual Oscillator Control
VSG	Virtual Synchronous Generator
VSM	Virtual Synchronous Machine
VSYNC	Virtual Synchronous Control
ZOH	Zero-Order Hold

LIST OF SYMBOLS

 C_{NL} Nonlinear load capacitance

 C_{dc} DC bus capacitance

 C_p Generic power controller

 C_v Generic voltage controller

 D_p Active power-frequency damping coefficient

 D_{po} Damping factor for the complex conjugate poles

 D_q Reactive power voltage droop coefficient

 D_z Damping factor for the complex conjugate zeros

*E** Voltage amplitude reference

 E_p Voltage amplitude in VISMA and in the IEPE topology

 G_{PLC} Swing equation function in the SPC

*G*_{ad} CCFAD function

 G_{cvd} CVD function

 G_d Delay function

 G_{ff} DID function

 G_i Current controller

 G_v Voltage controller

 I_L L_{dc} current

K_{ad} CCFAD proportional gain

 K_d Mechanical damping factor

 K_{dp} VSG damping characteristic constant

 K_{ff} DID gain

 K_{gd} KHI topology droop coefficient of the active power control

loop

K_i VSG inertial characteristic constant

*K*_i KHI topology integral gain

 K_{iL} Integral gain of the current controller in L_{dc}

 K_{iVdc} Integral gain of the voltage controller in C_{dc}

*K*_p KHI topology proportional gain

 K_{pL} Proportional gain of the current controller in L_{dc}

 K_{pVdc} Proportional gain of the voltage controller in C_{dc}

 K_{pv} Voltage controller proportional gain

 K_q Synchronverter droop coefficient of Q-v

 K_{rv} Voltage controller resonant gain

 L_1 Converter side inductance

 L_2 Grid side inductance

 L_{NL} Nonlinear load inductance

 L_V Virtual inductance

 L_{Vi} Fixed virtual inductance

 L_{dc} DC-DC converter inductance

 L_g Grid inductance

 L_s Stator self-inductance

 M_{af} , M_{bf} , M_{cf} Mutual inductances between the field winding and each of the

stator windings

M_f Maximum mutual inductance

 M_p Overshoot percentage

 N_n Notch filter function

 P^* Active power reference

 P_{VSG} VSG active power output

P_{bat} Battery bank power

 P_e Active power

 P_m Mechanical power

 P_n Nominal power

 Q^* Reactive power reference

 Q_d Droop equation reactive power

 Q_e Reactive power

 R_1 ESR of L_1

 R_2 ESR of L_2

 R_C ESR of C

 R_{NL} Resistance of the nonlinear load Virtual resistance

 R_V Virtual resistance

 R_{Vi} Fixed virtual resistance

R_a Current controller proportional gain

R_d Damping resistor

 R_{dc} ESR of L_{dc}

 S_N SPC nominal power

 T_a KHI topology AVR time constant

 T_d Droop equation torque

T_e Electromagnetic torque

 T_g KHI topology governor time constant

 T_m Mechanical torque

 T_s Sampling period

 U_n Effective value of the rated voltage amplitude

 V_B Battery bank voltage

 V_{dc} DC-link voltage

 V_{dc}^* DC-link voltage reference value

Z_o Output impedance

 a_6 to a_1 Z_o Denominator coefficients of Z_o

 b_7 to b_0 Z_o Numerator coefficients of Z_o

 $d\Delta\omega/dt$ Rate of change of angular velocity

 $\vec{e} = [e_a \quad e_b \quad e_c]^T$ Vector that represents the EMF

 f_g Grid frequency

 f_r Resonance frequency

 f_s Sampling frequency

 f_{sw} Switching frequency

 $\vec{t} = [i_a \quad i_b \quad i_c]^T$ Vector of the measured currents at the PCC

 $\vec{i}^* = [i_a^* \quad i_b^* \quad i_c^*]^T$ Reference three-phase currents

*i** Current reference

 i_1 Current in L_1

 i_c Current in C

 i_d^* Current reference in the d-axis

 i_g Current in L_2

 i_q^* Current reference in the q-axis

 k_L Current controller lead gain

 t_p Peak time

 $\vec{v} = [v_a \quad v_b \quad v_c]^T$ Three-phase voltages measured at the PCC

 v^* AC voltage reference

 v_c Voltage across C

v_g	Grid voltage
v_{inv}	Inverter voltage
v_m	Voltage amplitude in the Synchronverter
v_{pcc}	PCC voltage
v_r^*	Voltage reference in the Synchronverter
$lpha_L$	Compensation parameter of CCFAD
δ_p	DID pole
δ_z	DID zero
$ au_L$	Compensation parameter of CCFAD
$ au_p$	CVD denominator parameter
$ au_z$	CVD numerator parameter
ω^*	Frequency reference
ω_c	Low-pass filter cutoff frequency
ω_n	Natural frequency
ω_n	Rated rotor angular frequency
ω_{nf}	Notch frequency
ω_o	Grid nominal frequency
ω_{res}	Resonance frequency in rad/s
ω_s	Nominal angular speed in the SPC
Z	Impedance

Rotor frequency deviation $\Delta \omega$ Viscous damping coefficient В Filter capacitance \mathcal{C} Power damping coefficient D Inertia constant Н J Moment of inertia Regulator coefficient of reactive power K Effective value of the actual voltage amplitude U Phase compensation term f Damping factor ζ Phase reference $\overrightarrow{\Phi} = [\Phi_a \quad \Phi_b \quad \Phi_c]^T \quad \text{Flux linkage vector}$

Actual rotor angular frequency

ω

CONTENTS

ΑJ	bstract .		7
Re	esumo		8
LI	ST OF	FIGURES	10
LI	ST OF	TABLES	14
LI	IST OF	ABBREVIATIONS	15
Ll	IST OF	SYMBOLS	17
1	Intro	oduction	28
	1.1	Contextualization	28
	1.2	Motivation	30
	1.3	Objective	32
	1.3.1	Main Objective	32
	1.3.2	Specific Objectives	33
	1.4	Main Contributions	33
	1.5	Research Methodology	33
	1.6	Thesis Structure	34
	1.7	List of Publications	35
	1.7.1	Journal Papers:	35
	1.7.2	Conference papers:	35
	1.7.3	Journal Papers	36
	1.7.4	Conference Papers	36
2	Liter	rature Review	37
	2.1	Types of VSM	37
	2.1.1	VSM based on the synchronous machine model	37
	2 1	1.1 VISMA	37

2.1	.1.2 IEPE topology40
2.1	.1.3 Synchronverter41
2.1	.1.4 KHI topology45
2.1.2	VSM based on the swing equation
2.1	.2.1 ISE Laboratory topology47
2.1	.2.2 Synchronous Power Controller
2.1.3	VSM based on the frequency-power response model
2.1	.3.1 Virtual Synchronous Generator
2.1	.3.2 Virtual Synchronous Control Topology
2.2	State of the Art55
2.3	Chapter Summary58
3 Virtu	al Synchronous Machine Control – Inverter Side59
3.1	Introduction59
3.2	LCL Filter Modelling59
	LCL Filter Modelling59 LCL Filter Resonance and Damping Techniques61
3.3]	LCL Filter Resonance and Damping Techniques61
3.3.1 3.3.2	LCL Filter Resonance and Damping Techniques
3.3.1 3.3.2 3.3	LCL Filter Resonance and Damping Techniques
3.3.1 3.3.2 3.3 3.3	ACL Filter Resonance and Damping Techniques 61 Resonance Effect 61 Resonance Damping Techniques 62 2.1 Passive Damping 62
3.3 1 3.3.1 3.3.2 3.3 3.3	LCL Filter Resonance and Damping Techniques61Resonance Effect61Resonance Damping Techniques62.2.1 Passive Damping62.2.2 Active Damping63
3.3 1 3.3.2 3.3 3.3	LCL Filter Resonance and Damping Techniques61Resonance Effect61Resonance Damping Techniques62.2.1 Passive Damping62.2.2 Active Damping633.3.2.2.1 Cascaded Transfer Function63
3.3 1 3.3.1 3.3.2 3.3 3.3 3.4	LCL Filter Resonance and Damping Techniques61Resonance Effect61Resonance Damping Techniques62.2.1 Passive Damping62.2.2 Active Damping633.3.2.2.1 Cascaded Transfer Function633.3.2.2.2 State Feedback of the Plant65
3.3 1 3.3.1 3.3.2 3.3 3.3 3.4	LCL Filter Resonance and Damping Techniques61Resonance Effect61Resonance Damping Techniques62.2.1 Passive Damping62.2.2 Active Damping633.3.2.2.1 Cascaded Transfer Function633.3.2.2.2 State Feedback of the Plant65Effect of Computational Delay on Active Damping Through Capacitor
3.3 1 3.3.1 3.3.2 3.3 3.3 3.4 Current Feedle	ACCL Filter Resonance and Damping Techniques 61 Resonance Effect 61 Resonance Damping Techniques 62 2.1 Passive Damping 62 2.2 Active Damping 63 3.3.2.2.1 Cascaded Transfer Function 63 3.3.2.2.2 State Feedback of the Plant 65 Effect of Computational Delay on Active Damping Through Capacitor eack 66

3.6 Current Control Loop Design	73
3.6.1 System Description	73
3.6.2 Current Controller Design	75
3.6.3 Capacitor Current Feedback Active Damping Design	78
3.6.4 Capacitor Voltage Decoupling Design	79
3.6.4.1 Without Capacitor Current Feedback Active Damping and Capaci	tor
oltage Decoupling	82
3.6.4.2 With Capacitor Current Feedback Active Damping as a Lead	
ompensator and Capacitor Voltage Decoupling as a constant function	82
3.6.4.3 With Capacitor Current Feedback Active Damping and Capacitor	Voltage
ecoupling as a lead compensator	83
3.6.4.4 With Capacitor Current Feedback Active Damping and Capacitor	Voltage
ecoupling as a lead-lag compensator	83
3.6.5 Experimental Results	85
3.6.5.1 Current controller dynamic response assessment	86
3.6.5.2 Line impedance variation assessment	88
3.6.5.3 Disturbance rejection assessment – grid voltage harmonics	90
3.6.5.4 Disturbance rejection assessment – grid voltage sag	92
3.7 Voltage Control Loop Design	94
3.7.1 Voltage Controller Design	94
3.7.2 Disturbance Input Decoupling	95
3.8 Virtual Impedance Loop	97
3.9 Active and Reactive Power Controllers	99
3.10 Voltage Controller Influence on the Power Control Loops	101
3.11 Experimental Results	104
3.11.1 Grid-Forming Inverter Assessment – Isolated Operation	

	3.11	.2 Grid-Forming Inverter Assessment – Grid-Connected Operation	107
	3.12	Chapter Summary	113
4	Virt	tual Synchronous Machine Control – DC Side	114
	4.1	System Description	114
	4.2	DC-Link Voltage Control	114
	4.2.1	1 Tuning of the Current Controller in <i>Ldc</i>	115
	4.2.2	2 Tuning of the Voltage Controller in <i>Vdc</i>	116
	4.3	Simulation Results	118
	4.4	Chapter Summary	122
5	Ana	alysis of Converter Operation in a Microgrid	123
	5.1	Scenario 1 – Parallel Operation of GFM and GFL Inverters	123
	5.2	Scenario 2 – Low-Voltage Ride-Through Capability Assessment	127
	5.3	Scenario 3 – Parallel Operation of GFM Inverters	131
	5.4	Scenario 4 – Power Quality Assessment of the Microgrid	133
	5.5	Chapter Summary	135
6	Con	nclusions and Future Works	136
	6.1	Conclusions	136
	6.2	Future Works	137
R	eferenc	ces	138
A	PPENI	DIX A	153
A	. Coe	efficients of the transfer function of $Zo(s)$	153
A	PPENI	DIX B	156
В	. Exp	perimental setup	156

CHAPTER I

1 Introduction

This chapter begins by providing a general context of the problem to be addressed, as well as the motivations behind its development. It outlines the objectives, contributions, methodology, and structure of the thesis, followed by a list of publications.

1.1 Contextualization

The share of renewable energy sources (RESs) in power generation, compared to conventional sources (e.g., coal, gas, and oil), has increased significantly in recent years, as evidenced by strict environmental regulations, limited access to fossil fuels, and the need to meet the growing global energy demand [1]. By 2021, the global installed capacity of RES had increased to around 3146 GW, with solar photovoltaic and wind energy for the first time in history accounting for more than 10 % of the world's electricity supply [2]. It is also noteworthy that Brazil ranked as the fifth and third largest producer of solar photovoltaic and wind energy, respectively, in 2021 [2].

The RES, in turn, are incorporated into the electrical grid in the form of distributed generation (DG), and their application can improve the reliability and stability of the local electrical grid. Additionally, it can provide benefits to suppliers by reducing losses in the system along long transmission lines and decreasing the total investment required for the creation of a new transmission line due to the growing energy consumption. [3].

The rise of microgrids has facilitated the widespread adoption of DGs by enabling more efficient control of multiple DGs as a unified system. Microgrids can both connect to and disconnect from the grid, operating in grid-connected or isolated modes [4]. In grid-connected mode, they support the main grid and meet part of the load demand, while in isolated mode, their focus shifts from economic benefits to ensuring a stable electricity supply for customers [5].

In the grid-connected operating mode, the voltage and frequency control of the microgrid's electrical system is managed by the existing conventional electrical grid, which is usually considered an infinite power source relative to the microgrid. In the isolated operating mode, the

microgrid needs to generate and control its own voltage and, if operating in alternating current (AC), it also needs to control the frequency [6]. When operating isolated and in AC, the microgrid must maintain voltage and frequency values regulated according to the standards established for the conventional power distribution grid [7]. Electrical parameters (frequency, voltage, etc.) must also be kept within the limits specified by the local utility during the transition state between both operating modes, i.e., from the connected mode to the isolated mode and vice versa [8].

Due to the growing development of RESs, the electrical grid—which was traditionally dominated by rotating generators (e.g., synchronous generators)—is currently tending toward a scenario with an increasing presence of inverter-based resources (IBRs) [9]. Generation from RESs generally requires IBRs in order to align the generated energy with standardized grid requirements and to form the grid in isolated systems. Although in Brazil most electricity generation is still carried out by large generators, the increasing integration of RESs—which typically provide little to no mechanical inertial response—may compromise the stability of the electrical system [10], [11], [12].

The RESs, unlike traditional power generation, are highly susceptible to environmental variables, making their output inherently intermittent. For example, solar power is significantly affected by cloud cover, while wind power fluctuates with wind speed and direction. These variations can lead to rapid and significant changes in power generation over short periods of time, even within the same day. Such irregularities not only disrupt the balance between supply and demand but can also exacerbate challenges like grid congestion, as the fluctuating energy supply may not align with demand patterns. In addition to frequency and voltage instability, rapid fluctuations may cause problems in grid synchronization, and trigger cascading failures across interconnected systems [13].

When there is an imbalance between generation and consumption in an energy system, IBRs cannot respond instantly to rebalance the system. In conventional systems, the kinetic energy stored in the rotors of electromechanical generators is responsible for neutralizing this imbalance through inertial response until primary frequency control is activated. In such systems, the inertial response can support frequency and voltage regulation of the grid for up to approximately ten seconds during disturbances that cause an imbalance between demand and generation [14]. As there is an increasing penetration of RES, the system's inertial response and damping characteristics are declining [9].

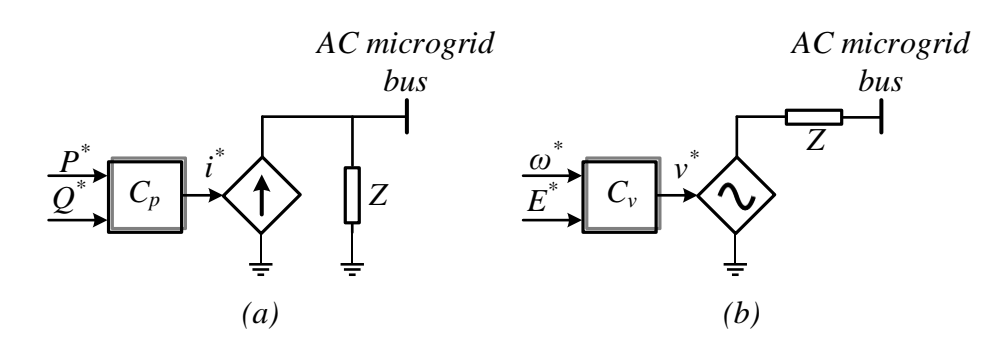
The reduction in inertia causes an increase in the rate of change of frequency (RoCoF), which is a measure of how quickly the frequency changes after an unexpected imbalance between generation and demand, and to a low frequency nadir (minimum frequency point) in a short period of time [9]. These events are detrimental to the stable operation of an electrical system, as they can trigger frequency protection relays and, in more extreme cases, may lead to a blackout.

As an example of a real case of instability in the power grid, the blackout that occurred in South Australia in 2016 can be cited. It was caused by the loss of the Heywood interconnector (a 275 kV AC interconnector between the states of South Australia and Victoria). This incident occurred due to the system's low inertia, with significant penetration of RESs [15]. Another example is the blackout that took place on August 9, 2019, in the United Kingdom, caused by the disconnection of DG units due to a lightning strike on a transmission line (Eaton Socon – Wymondley Main). Due to the system's low inertia, the frequency reached values outside the specified range, which triggered the activation of low-frequency demand disconnection relays [16].

1.2 Motivation

Depending on the control technique used to control the IBRs, they can be generally divided into grid-following (GFL) inverters and grid-forming (GFM) inverters. GFL inverters are controlled as current sources in parallel with high impedance, Z, as shown in Figure 1-1 (a), whereas GFM inverters are controlled as voltage sources in series with low impedance, as shown in Figure 1-1 (b). P^* and Q^* are the active and reactive power references, C_p is the power controller and i^* is the current reference. ω^* and E^* are the frequency and voltage amplitude reference, C_v is the voltage controller and v^* is the AC voltage reference.

Figure 1-1 – Simplified representation of the IBR control technique. (a) grid-following, (b) grid-forming.



Source: Adapted from [17].

A GFL inverter operates by synchronizing its output to the grid's voltage and frequency. This synchronization is achieved through measurements at the point of common coupling (PCC) using a phase-locked loop (PLL). However, the PLL can adversely affect system stability, particularly in weak grid conditions [18], [19]. GFL inverters are generally configured to operate at rated output power and inject it into an energized grid. They rely on cascaded control loops, where power control loops regulate the active P and reactive Q power to generate current references for the inner current control loop. This inner loop, typically implemented using a proportional-integral (PI) controller in the dq frame or a proportional-resonant (PR) controller in the $d\beta$ frame, tracks these current references. In addition to the disadvantages associated with the use of the PLL, the GFL inverter also lacks the capability to operate in island mode, perform black-start, and generate a regulated output voltage [20].

The GFM inverters, on the other hand, have the capability to operate both in islanded mode and connected to the grid, and do not rely on a PLL to maintain synchronization with the grid. Instead, most reported GFM inverters use the power synchronization mechanism of synchronous machines to stay synchronized with the grid [21]. They can maintain a regulated output voltage and can perform black-start. A GFM inverter can be defined according to the North American Electric Reliability Corporation (NERC) as "an internal voltage phasor that is constant or nearly constant in the sub-transient to transient time frame" [20]. Although the term GFM has been widely used in recent years, its concept, which is based on regulating voltage and frequency, was proposed many years ago [22].

Among the GFM strategies, those that stand out the most are: the Virtual Synchronous

Machine (VSM) [23], [24], [25], [26], that emulates the behavior of a synchronous machine, adding inertia and damping of a traditional synchronous machine to IBRs; droop control [27], [17], [28], that adjusts P/Q power output based on local frequency/voltage deviations (P-f and Q-V droops), enabling decentralized load-sharing among distributed resources without communication; Power Synchronization Control (PSC) [29], [30], [31], that enables IBRs to synchronize their output power with the grid by adjusting voltage, frequency, and phase; Virtual Oscillator Control (VOC) [32], [33], [34], that leverages nonlinear oscillator dynamics to self-synchronize IBRs with the grid autonomously, enabling decentralized operation without PLL; Synchronverter [35], [36], [37], [38], that replicates exactly the mathematical model of a synchronous machine (electromechanical equations, flux dynamics, and excitation control) in IBRs and Synchronous Power Controller (SPC) [39], [40], [41], that combines droop characteristics with virtual inertia and damping, blending static power-frequency regulation.

Whereas GFL inverters face more challenges when operating in weak grids, GFM inverters are more susceptible to instability when operating in strong grids. Many studies have been conducted with the goal of enhancing the dynamic response of GFM inverters, especially with regard to reducing power oscillations. However, in most of the studies conducted (to be explored in the next chapter), the investigation focused almost entirely on the power control loops, without a deep analysis of the inner loops to improve the dynamic response and stability of the GFM inverter.

In this thesis, the specific type of GFM inverter chosen was the VSM. This choice is due to the well-established applicability of synchronous machines in conventional power generation systems, as well as the possibility of emulating virtual inertia, damping, and other ancillary services.

1.3 Objective

1.3.1 Main Objective

The main objective of this work is to develop a control strategy for power converters using virtual synchronous machines, with a focus on the design of inner control loops, to enhance the dynamic response and stability of the converter.

1.3.2 Specific Objectives

- Survey and analyze the state of the art regarding control techniques that emulate VSM;
- Design and implement the inner control loops of the VSM;
- Design and implement the power control loops of the VSM;
- Analyze the operation of the VSM in a microgrid.

1.4 Main Contributions

- Development of a current controller with the capabilities of high bandwidth—achieved for converters in the range of a few tens of kilowatts—, mitigation of the resonance frequency effect of the LCL filter, and improved response to disturbances that may occur in the power grid.
- Development of a voltage controller with disturbance input decoupling, which enhances the dynamic response of the VSM's electrical parameters when connected to the grid and subjected to transients, such as power reference variations. Specifically, it improves the control of active power, reactive power, and current. Additionally, the voltage dynamics of the VSM are enhanced during operation in isolated mode and undergoing load variations.

1.5 Research Methodology

The methodology of this work was divided into four main stages:

I – Theoretical Foundation

In this stage, documentary research was conducted to gain knowledge and mastery of the topic being addressed, namely, VSMs. Thus, the goal was to understand what has already been produced on the subject, what is currently being studied and published, and potential problems that remain unsolved and are feasible for resolution. In addition to the study of VSMs, a deeper theoretical understanding was also developed regarding the issue of resonance in LCL-type filters and active damping techniques for IBRs.

II - Control Strategy Proposal

In the second stage, the internal loops of the VSM were designed and implemented. This phase was carried out using the MATLAB/Simulink software, which was chosen for its high fidelity in simulating physical systems in a virtual environment.

III - Validation of the Control Strategy in an Experimental Environment

After the validation of the VSM operating in a simulation environment, it was tested and validated in a testbench. Several scenarios were created and analyzed to ensure the effectiveness of the proposed strategy.

IV – Operation of the VSM in a Microgrid

After completing the previous steps, the proposed power control strategy based on the VSM was evaluated in a simulated microgrid using MATLAB/Simulink software.

1.6 Thesis Structure

This thesis is organized into six chapters, with the content of each outlined below:

- Chapter I presents the general context and motivation for the development of this
 thesis. It begins by discussing the increasing integration of RESs into modern power
 systems and the resulting shift toward IBRs, particularly in microgrids. The chapter
 highlights the main challenges posed by IBRs, such as reduced inertia and damping,
 which impact grid stability and dynamic performance.
- Chapter II presents a literature review of strategies that emulate VSM. The advantages and disadvantages of each approach are discussed. The state of the art in power control strategies is also presented to identify existing research gaps.
- Chapter III presents the control strategy for the VSM on the inverter side. It includes the modelling of the converter's inner control loops, as well as the outer loop.
- Chapter IV presents the control strategy for the VSM on the DC side. It includes the
 modelling of the battery current control and the DC-link voltage control.
- Chapter V presents the performance of the VSM operating in a microgrid with other

sources and loads.

• Chapter VI presents the main conclusions of the thesis and potential future works.

1.7 List of Publications

This thesis has resulted in the following publications:

1.7.1 Journal Papers:

JP1. A. W. d. S. Serra, L. A. d. S. Ribeiro and M. Savaghebi, "Disturbance Decoupling in Grid-Forming Inverters for Enhanced Dynamic Response," Eletrônica de Potência, vol. 30, no. e202528, pp. 1-10, March 2025.

1.7.2 Conference papers:

- **CP1. A. W. Dos Santos Serra**, K. Augusto Freitas Nascimento, J. Gomes de Matos, L. Antonio de Souza Ribeiro and H. Araújo Oliveira, "Improved Power Performance in Bidirectional Grid-Forming Converters via Modified Voltage Control," 18th Brazilian Power Electronics Conference (COBEP), Vitória, Brazil, 2025. (accepted)
- **CP2. A. W. Dos Santos Serra**, K. Augusto Freitas Nascimento, J. Gomes de Matos, L. Antonio de Souza Ribeiro, M. Savaghebi and H. Araújo Oliveira, "Bidirectional Grid-Forming Converter with Modified Voltage Control for Enhanced Power Dynamics," IECON 2025 51th Annual Conference of the IEEE Industrial Electronics Society, Madrid, Spain, 2025. (accepted)
- **CP3. A. W. Dos Santos Serra**, L. Antonio de Souza Ribeiro and M. Savaghebi, "Current Controller for LCL-Type Grid-Following Inverter with Active Damping and Capacitor Voltage Decoupling," IECON 2024 50th Annual Conference of the IEEE Industrial Electronics Society, Chicago, IL, USA, 2024, pp. 1-6, doi: 10.1109/IECON55916.2024.10905892.
- **CP4. A. W. D. S. Serra**, L. A. d. S. Ribeiro and M. Savaghebi, "An Improved Control for Grid-Following Inverter with Active Damping and Capacitor Voltage Decoupling," 2024 IEEE Energy Conversion Congress and Exposition (ECCE), Phoenix, AZ, USA, 2024, pp. 3678-3684, doi: 10.1109/ECCE55643.2024.10861181.
- **CP5. A. W. Dos Santos Serra**, L. A. De Souza Ribeiro and M. Savaghebi, "A Multi-Loop Control for Grid-Forming Converters with Enhanced Dynamics," 2024 Energy Conversion

Congress & Expo Europe (ECCE Europe), Darmstadt, Germany, 2024, pp. 1-7, doi: 10.1109/ECCEEurope62508.2024.10751951.

CP6. A. W. Dos Santos Serra, L. A. De Souza Ribeiro and J. G. De Matos, "An Enhanced Current Controller for Grid-Connected Inverters based on Capacitor Current Feedback Active Damping and Capacitor Voltage Decoupling," 2023 25th European Conference on Power Electronics and Applications (EPE'23 ECCE Europe), Aalborg, Denmark, 2023, pp. 1-9, doi: 10.23919/EPE23ECCEEurope58414.2023.10264543.

Below are other publications by the author in areas co-related to the thesis.

1.7.3 Journal Papers

JP1. A. W. dos S. Serra, H. A. Oliveira, L. A. de S. Ribeiro, J. G. de Matos, A. C. Oliveira, and O. R. Saavedra, "Mission-critical microgrids: Strategies for safe and reliable operations," Electric Power Systems Research, vol. 245, p. 111625, 2025, doi: 10.1016/j.epsr.2025.111625.

1.7.4 Conference Papers

CP1. A. W. dos Santos Serra, L. A. de Souza Ribeiro and M. Savaghebi, "Grid-Forming Converter with Improved Dynamic and Disturbance Rejection Capability," 2024 IEEE 15th International Symposium on Power Electronics for Distributed Generation Systems (PEDG), Luxembourg, Luxembourg, 2024, pp. 1-6, doi: 10.1109/PEDG61800.2024.10667424.

CHAPTER II

2 Literature Review

This chapter presents the main techniques that emulate VSMs and their respective classifications, based on the similarities they share. The three models presented are the VSM based on the synchronous machine model, the VSM based on the swing equation, and the VSM based on the frequency-power response model. The VSM based on the swing equation was selected due to its simplicity and was used to implement the proposed VSM in this thesis, which will be described in more detail in the next chapter. Then, the state of the art on power control strategies using GFM inverters is presented, along with research opportunities derived from the presented advancements.

2.1 Types of VSM

2.1.1 VSM based on the synchronous machine model

The VSMs based on this model are characterized by emulating the electrical and mechanical characteristics of the synchronous machine with high fidelity. Essentially, the techniques in this group reproduce the electrical and mechanical equations of the synchronous machine. The main algorithms found in the literature are: VISMA, Institute of Electrical Power Engineering (IEPE) Topology, Synchronverter, and Kawasaki Heavy Industries (KHI) Topology.

2.1.1.1 VISMA

VISMA was the first algorithm proposed in the literature with the goal of making an IBR operate as a VSM. It was proposed by Hans-Peter Beck and Ralf Hesse in 2007 and implements a 5th-order model of the synchronous machine [42].

The input and output of this algorithm are the three-phase voltages measured $\vec{v} = [v_a \quad v_b \quad v_c]^T$ at the PCC between the VISMA and the grid, and the reference three-phase currents $\vec{t}^* = [i_a^* \quad i_b^* \quad i_c^*]^T$, respectively. A hysteresis-type current controller is used to achieve the desired operation of the VISMA. Unlike the conventional synchronous generator, the VISMA allows for the bidirectional flow of active and reactive power [43]. The equations governing the electromechanical model of VISMA are given by (2.1) - (2.3).

$$\vec{e} = \vec{v} + \vec{\iota}^* r_s + L_s \frac{d\vec{\iota}^*}{dt} \tag{2.1}$$

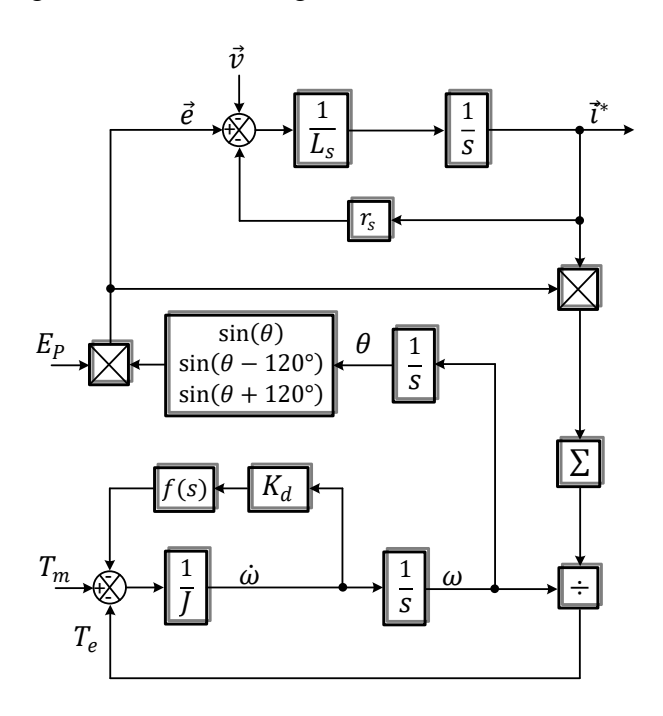
$$T_m - T_e = \frac{1}{I} \frac{d\omega}{dt} + K_d f(s) \frac{d\omega}{dt}$$
 (2.2)

$$\theta = \int \omega dt \tag{2.3}$$

Where $\vec{e} = [e_a \quad e_b \quad e_c]^T$ is the vector that represents the electromotive force (EMF) induced in the stator windings (in *abc* coordinates) and L_s is the stator self-inductance. The notations T_m , T_e , J, K_d , f(s), ω and θ represent the mechanical torque, electromagnetic torque, moment of inertia, mechanical damping factor, phase compensation term (which ensures that the virtual damping force neutralizes any oscillatory rotor movement in the opposite phase), angular velocity in mechanical radians per second, and the rotational angle, respectively. The induced EMF is given by amplitude E_p and as a function of θ , as presented in (2.4). From (2.1) – (2.4), it is possible to obtain the block diagram of the VISMA control, which is shown in Figure 2-1.

$$\vec{e} = E_p \begin{bmatrix} \sin(\theta) \\ \sin\left(\theta - \frac{2\pi}{3}\right) \\ \sin\left(\theta + \frac{2\pi}{3}\right) \end{bmatrix}$$
 (2.4)

Figure 2-1 – Block diagram of the VISMA control.



Source: Adapted from [44].

From Figure 2-1, it can be observed that there is no reactive power control, meaning that reactive power cannot be injected into the grid. Since VISMA operates as a current source, there is the disadvantage of operating only in grid-connected mode, thus not allowing isolated operation. To address this issue, the authors in [45] proposed the addition of capacitors in the inverter filter to form an LC filter, with the aim of feeding back the voltages on the capacitor to the VISMA model. In addition, frequency and voltage regulation loops are added to allow stable long-term operation. Table 2-1 presents the advantages and disadvantages of this control strategy.

Table 2-1 – Advantages and disadvantages of VISMA.

Advantages	Disadvantages
Overcurrent protection	Requires high computational effort
Reproduces the characteristics of a synchronous machine with a high level of detail	Complex model and requires the synchronous machine's constructive parameters
PLL is not required for synchronization	

Source: Author.

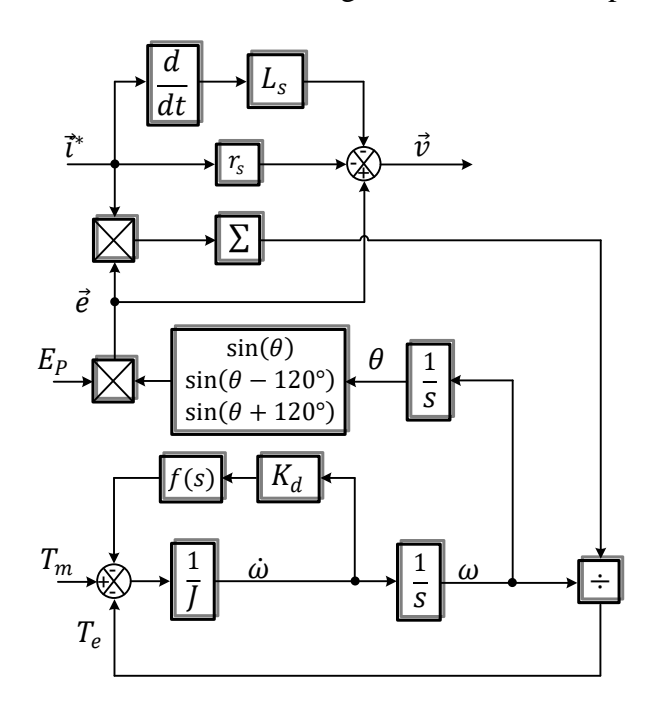
2.1.1.2 IEPE topology

The IEPE topology is equivalent to a VISMA operating as a voltage source. The equations presented for the operation of the VISMA are the same for this strategy; however, unlike the former, it is not the voltages at the PCC that are measured, but rather the currents. Therefore, (2.1) can be rewritten as (2.5), where \vec{v} is now the reference voltage vector for the Pulse Width Modulation (PWM) block and $\vec{t} = [i_a \quad i_b \quad i_c]^T$ is the vector of the measured currents at the PCC.

$$\vec{v} = \vec{e} - \vec{i}r_s - L_s \frac{d\vec{i}}{dt} \tag{2.5}$$

The IEPE topology has the capability to operate independently without the need for the addition of capacitors to the output filter as is done in the VISMA. However, frequency and voltage control loops must still be used to ensure stable operation of the converter. In Figure 2-2, the control block diagram of the IEPE topology is presented, and it can be observed that the derivative of the measured currents is taken, which may lead to amplification of the noise signals present in the measurement.

Figure 2-2 – Control Block Diagram of the IEPE Topology.



Source: Adapted from [45].

Table 2-2 presents the advantages and disadvantages of this control strategy.

Table 2-2 – Advantages and disadvantages of the IEPE Topology.

Advantages	Disadvantages
Allows operation in isolated mode without changes in the hardware	Requires high computational effort
Reproduces the characteristics of a synchronous machine with a high level of detail	Complex model and requires the synchronous machine's constructive parameters
PLL is not required for synchronization	No overcurrent protection
	May amplify noise due to the use of a differentiator

2.1.1.3 Synchronverter

Zhong and Weiss proposed a control strategy based on VSM known as Synchronverter in 2011 [36]. The same authors had already proposed this same control strategy in 2009, however, under the name Static Synchronous Generator (SSG) [46].

Like the previously presented strategies, the Synchronverter also features a detailed model of a synchronous generator and is considered equivalent to a synchronous generator with a small capacitor bank. It operates as a voltage source and has frequency and voltage droop control loops, allowing for parallel operation with multiple converters and control of both active and reactive power.

The Synchronverter is modelled as a synchronous generator with a cylindrical-type rotor, without damper windings, a pole number of two, and neglecting the effects of eddy currents and magnetic saturation in the core. These considerations are meant to simplify the emulation of the control strategy.

The mutual inductances between the field winding and each of the stator windings (M_{af}, M_{bf}, M_{cf}) are given by (2.6) - (2.8), where M_f is the maximum mutual inductance between the stator windings and the field winding.

$$M_{af} = M_f \cos(\theta) \tag{2.6}$$

$$M_{bf} = M_f \cos(\theta - 120^\circ) \tag{2.7}$$

$$M_{cf} = M_f \cos(\theta - 240^\circ) \tag{2.8}$$

The flux linkage in each phase can be described in vector form. Defining the current vector $\vec{t} = [i_a \quad i_b \quad i_c]^T$ and the flux linkage vector $\vec{\Phi} = [\Phi_a \quad \Phi_b \quad \Phi_c]^T$, and considering that $i_a + i_b + i_c = 0$, the stator flux linkages equation can be rewritten as (2.9). Here, $L_s = L + M$ represents the total self-inductance of the stator winding, where L is the self-inductance of the armature winding, M is the mutual inductance between each armature winding and i_f is the field current.

$$\vec{\Phi} = L_s \vec{i} + M_f i_f \begin{bmatrix} \cos(\theta) \\ \cos(\theta - 120^\circ) \\ \cos(\theta - 240^\circ) \end{bmatrix}$$
(2.9)

From (2.9), the terminal voltage $\vec{v} = [v_a \quad v_b \quad v_c]^T$ can be obtained as (2.10), where $\vec{e} = [e_a \quad e_b \quad e_c]^T$ is the induced EMF vector and is given by (2.11).

$$\vec{v} = -r_s \vec{i} - \frac{d\vec{\Phi}}{dt} = -r_s \vec{i} - L_s \frac{d\vec{i}}{dt} + \vec{e}$$
 (2.10)

$$\vec{e} = M_f i_f \frac{d\theta}{dt} \begin{bmatrix} \sin(\theta) \\ \sin(\theta - 120^\circ) \\ \sin(\theta - 240^\circ) \end{bmatrix} - M_f \frac{di_f}{dt} \begin{bmatrix} \cos(\theta) \\ \cos(\theta - 120^\circ) \\ \cos(\theta - 240^\circ) \end{bmatrix}$$
(2.11)

It is assumed that the field winding is supplied by a direct current (DC) source; therefore, the second term of (2.11) is zero, and (2.11) can be rewritten as (2.12) [36].

$$\vec{e} = M_f i_f \frac{d\theta}{dt} \begin{bmatrix} \sin(\theta) \\ \sin(\theta - 120^\circ) \\ \sin(\theta - 240^\circ) \end{bmatrix}$$
 (2.12)

The equation governing the mechanical behavior of the Synchronverter is given by (2.13), with T_e obtained from (2.14) and B representing the viscous damping coefficient. The reactive power Q_e of the Synchronverter is given by (2.15).

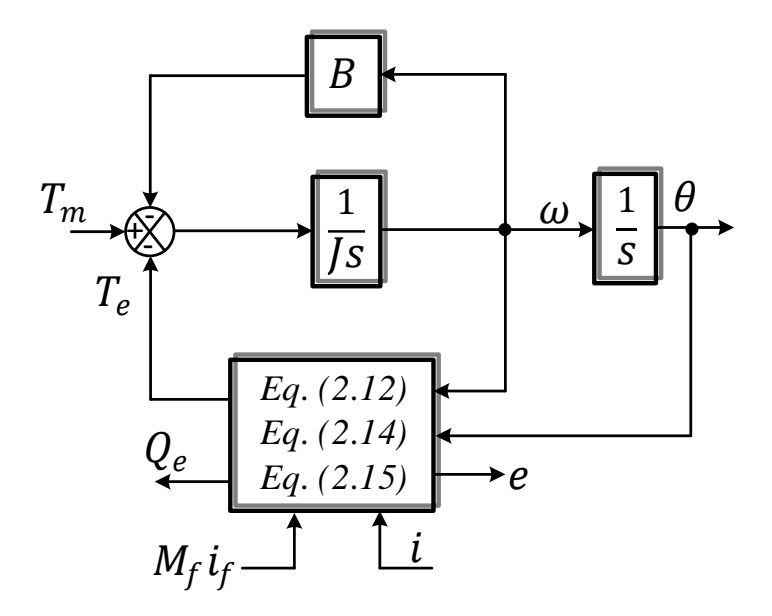
$$J\frac{d\omega}{dt} = T_m - T_e - B\omega \tag{2.13}$$

$$T_e = M_f i_f \begin{bmatrix} \sin(\theta) \\ \sin(\theta - 120^\circ) \\ \sin(\theta - 240^\circ) \end{bmatrix}^T \cdot \begin{bmatrix} i_a \\ i_b \\ i_c \end{bmatrix}$$
 (2.14)

$$Q_e = -\frac{d\theta}{dt} M_f i_f \begin{bmatrix} \cos(\theta) \\ \cos(\theta - 120^\circ) \\ \cos(\theta - 240^\circ) \end{bmatrix}^T \cdot \begin{bmatrix} i_a \\ i_b \\ i_c \end{bmatrix}$$
 (2.15)

In Figure 2-3, the electronic part of a Synchronverter is shown without the controls, which will be presented later.

Figure 2-3 – Electronic part of a Synchronverter without the controls.



Source: Adapted from [36].

In Figure 2-4, the control block diagram of the Synchronverter is shown with the addition of the control loops for active and reactive powers, which are governed by the droop equations shown in (2.16) e (2.17).

$$T_d = (\omega^* - \omega)K_d \tag{2.16}$$

$$Q_d = (v_r^* - v_m) K_q (2.17)$$

Where T_d is the torque produced by the droop equation, ω^* is the angular frequency

reference, Q_d is the reactive power provided by the droop equation, v_r^* is the voltage reference, v_m is the amplitude of v measured at the PCC, and K_q is the voltage droop coefficient.

 P^* T_d T_d T_d T_e T_e

Figure 2-4 – Control block diagram of the Synchronverter.

Source: Adapted from [46].

The angle θ must be limited to 2π through a reset to avoid numerical overflow. The voltage v_m can be obtained from (2.18), and the voltage is applied to the PWM block to generate the gate trigger signals for the semiconductor switches of the converter.

$$v_m = \frac{2}{\sqrt{3}} \sqrt{-(v_a v_b + v_b v_c + v_c v_a)}$$
 (2.18)

The Synchronverter operates as a voltage source and, therefore, can function in isolated mode. When operating in grid-connected mode, a PLL is used to synchronize with the grid; however, several improvements have been made to the operation of the Synchronverter, one of which is the methodology proposed in [47] that allows for synchronization of the Synchronverter with the grid without using a PLL. The fundamental principle is to make the phase difference between the Synchronverter and the grid voltage at the PCC null, while ensuring that the magnitudes of the voltages of both are equal. Initially, P^* and Q^* are adjusted to zero, and PI controllers are used to eliminate this phase difference. This methodology solves the problem of resetting the integrator during grid reconnection. Additionally, a virtual impedance is used to equalize the magnitudes of the voltages [43].

In [48], the authors propose an improvement to the Synchronverter by adding a fast current loop, and the results show that there was a reduction in the sensitivity of the Synchronverter to measurement errors, processing delays, and grid voltage imbalance. In [49], the authors demonstrated that using the damping factor as a droop coefficient is not the most suitable solution, since the converter's response cannot be adjusted without altering the characteristics of the steady-state droop curve. Therefore, they proposed adding a derivative term to the active power control loop, which allows the Synchronverter to be freely modified without interfering with the droop curve.

In Table 2-3, the main advantages and disadvantages of the Synchronverter are presented.

Table 2-3 – Advantages and disadvantages of Synchronverter.

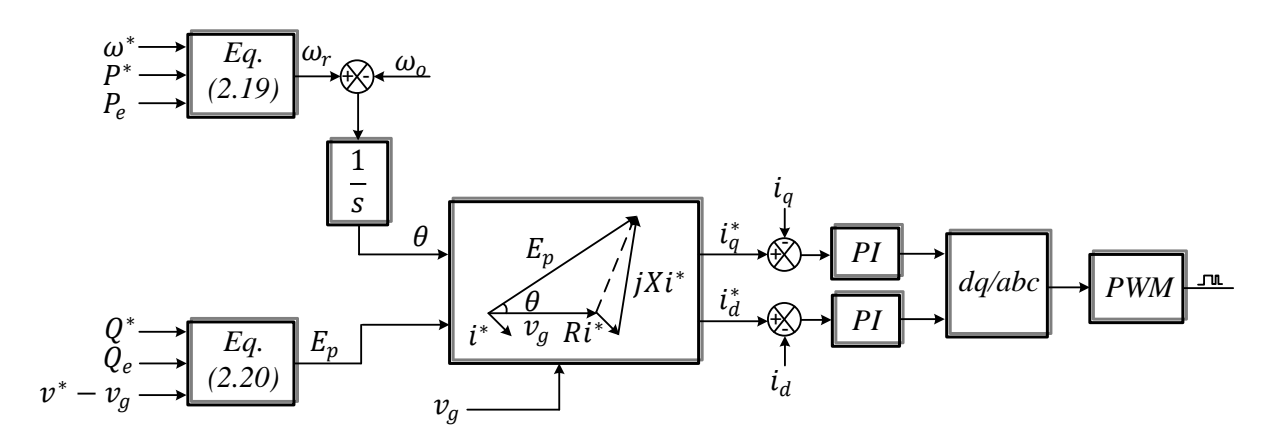
Disadvantages	
Requires high computational effort	
Numerical instabilities may occur due to the complex mathematical model of the algorithm	
No overcurrent protection (depending on the model used)	

Source: Author.

2.1.1.4 *KHI topology*

Researchers from KHI proposed in [50] an algebraic model of the VSM, which consists of the phasor representation of the synchronous generator, while the dynamic equations of the generator are neglected. This topology assumes that the rotor is of the cylindrical type and that the impedance of the VSM is low over a wide range of frequencies [43]. The block diagram of the control structure is shown in Figure 2-5, and the dynamics of the governor and the Automatic Voltage Regulator (AVR) are given by (2.19) and (2.20).

Figure 2-5 – Control block diagram of the KHI topology.



Source: Adapted from [43].

$$\omega_r = \omega^* + K_{gd}(P^* - P) \left(\frac{1}{1 + T_q s}\right)$$
 (2.19)

$$E_p = \left[v^* - v_g + K_{aq}(Q^* - Q)\left(\frac{1}{1 + T_a s}\right)\right] \left(K_p + \frac{K_i}{s}\right)$$
(2.20)

Where T_g is the governor time constant, K_{gd} is the droop coefficient of the active power control loop, v_g is the grid voltage, K_{aq} is the droop coefficient of the reactive power control loop, T_a is the AVR time constant, K_p is the proportional gain and K_i is the integral gain.

The governor is responsible for generating the phase reference, and the AVR for the voltage amplitude, both of which are used to generate the current references $(i_q^* e i_d^*)$ from the phasor representation.

In Table 2-4, the main advantages and disadvantages of the KHI topology are presented.

Table 2-4 – Advantages and disadvantages of KHI Topology.

Advantages	Disadvantages
Simple implementation	Requires switching control from grid- connected mode to isolated mode
Overcurrent protection	PLL required

Source: Author.

2.1.2 VSM based on the swing equation

The techniques that emulate VSM within this group are characterized by solving the swing equation and its variants, which is generally presented in (2.21). They differ fundamentally from the machine-based model by not adopting a very detailed model of the machine. The main control techniques that use this model are the ISE Laboratory topology and the SPC.

$$J\omega \frac{d\omega}{dt} = P_m - P_e - D\Delta\omega \tag{2.21}$$

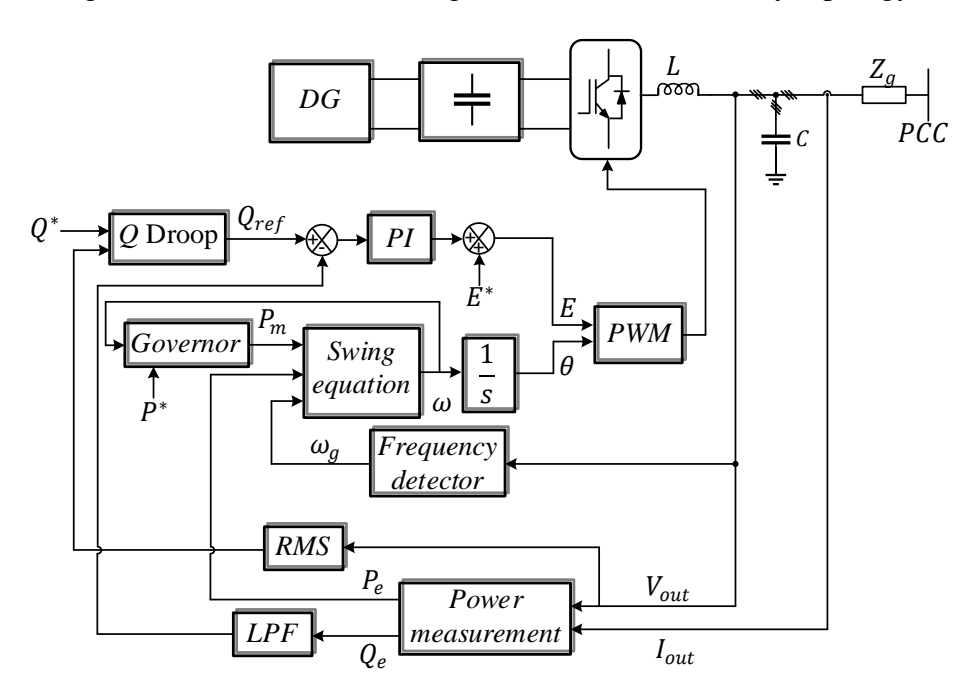
Where P_m is the mechanical power, P_e is the electromagnetic power, $D = B\omega$ is the power damping coefficient, and $\Delta\omega$ is the rotor frequency deviation.

2.1.2.1 ISE Laboratory topology

This topology was developed by the research group of the ISE laboratory at Osaka University [51]. The block diagram of this control strategy is shown in Figure 2-6. The "frequency detector" block for estimating ω_g is a conventional PLL. The "power measurement" block is responsible for calculating P_e and Q_e from the voltage measurements on the filter capacitor (V_{out}) and the output current (I_{out}). The "Q Droop" block performs the conventional Q-v droop control and is responsible for generating Q_{ref} , which is controlled by a PI controller. The "Governor" block (implements the conventional P- ω droop control) has the function of generating P_m , which is part of the balance equation, and is responsible for calculating ω and generating θ through an integrator. These, along with the magnitude of the VSM voltage, E, are the input parameters for the PWM block to generate the trigger signals.

This topology functions as a voltage source converter and, therefore, allows for isolated operation. Several improvements have been made to its control structure over the years, with the following being noteworthy: in [52], the authors propose the addition of a virtual inductance to improve active power sharing and dampen the oscillation it causes. Moreover, reactive power sharing is improved based on an inverse droop control v-Q and the estimation of a common AC bus voltage. In [53], the authors use a particle swarm optimization algorithm to adjust the system parameters to minimize the phase angle deviation and allow for smooth transitions after disturbances for the parallel operation of VSMs.

Figure 2-6 – Control block diagram of the ISE laboratory topology.



Source: Adapted from [52].

In Table 2-5, the main advantages and disadvantages of the ISE laboratory topology are presented.

Table 2-5 – Advantages and disadvantages of the ISE laboratory topology.

Advantages	Disadvantages
Simple replication of synchronous generator dynamics	No overcurrent protection
PLL required for initial synchronization	Possible system oscillation if parameters are incorrectly tuned
Allows operation in isolated mode	

Source: Author.

2.1.2.2 Synchronous Power Controller

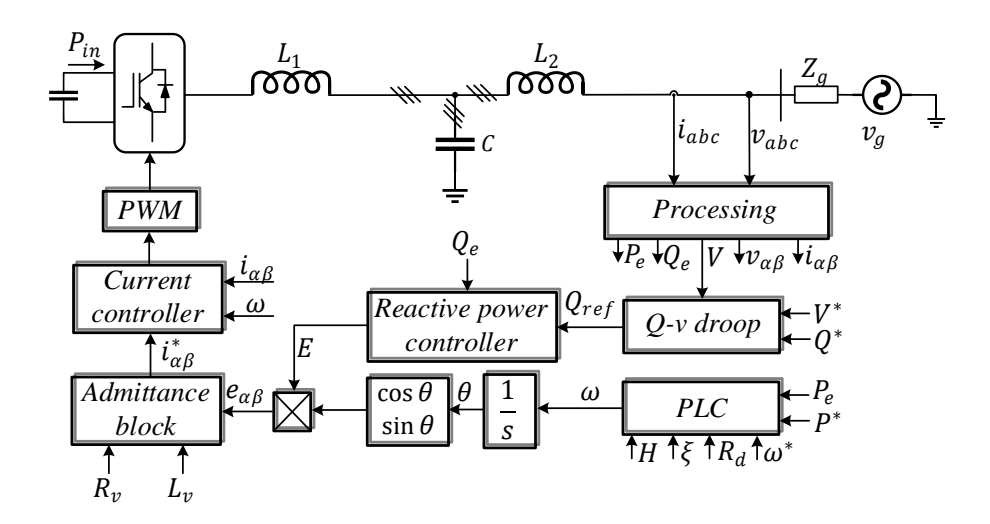
The SPC is another control algorithm that solves the synchronous generator swing equation and was proposed by Rodriguez et al. in [54]. Its structure is similar to that presented in the ISE laboratory topology; however, it differs by having a current control loop and a virtual admittance block that defines the current reference to be injected into the grid. The SPC control block diagram can be seen in Figure 2-7.

The SPC uses a power-based synchronization method, which ensures power balance in the converter and inherently synchronizes the system with the grid. Since the Power Loop Controller (PLC) regulates synchronization with the electrical grid, there is no need for any additional synchronization mechanism, such as a PLL [55].

The PLC block solves the swing equation in the form presented in (2.22), where H is the inertia constant, S_N is the nominal power of the generator and ω_S is the nominal angular speed.

$$\omega = \omega^* + \frac{1}{(2HS_N/\omega_s)s + D}(P^* - P)$$
(2.22)

Figure 2-7 – SPC control block diagram.



Source: Adapted from [56].

The droop Q-v control loop generates the reactive power reference, Q_{ref} , which is an input parameter for the reactive power controller and that provides the amplitude value, E, through a PI controller. With E and θ , resulting from the integration of ω generated by the PLC, the internal

EMF in the $\alpha\beta$ coordinate axis, $e_{\alpha\beta}$, interacts with the grid through the virtual admittance. A PR current controller is used to control the current, $i_{\alpha\beta}$, to be injected into the grid.

Some modifications have been proposed in the literature regarding the function that implements the PLC. In [57], the authors propose a PI controller as the transfer function for $G_{PLC}(s)$ (function that implements the swing equation and is contained in the PLC block), such that tracking of active and reactive powers is achieved with zero error despite variations in the grid frequency. In [58], the authors compare three structures for $G_{PLC}(s)$, where a PI controller was used to eliminate the inherent droop response of the initial P- ω PLC structure, and a lead-lag transfer function was used to configure three parameters: inertia, damping coefficient, and droop gain in steady state, which can be adjusted independently [55].

In Table 2-6, the main advantages and disadvantages of the SPC are presented.

Table 2-6 – Advantages and disadvantages of the SPC.

Advantages	Disadvantages
Simple replication of synchronous generator dynamics	The initial approach of the PLC results in an inherent frequency droop
No PLL required	Multiple control loops for tuning
Allows operation in isolated mode	
Overcurrent protection	

Source: Author.

2.1.3 VSM based on the frequency-power response model

Control strategies that emulate VSM and fit this type of model are characterized by reproducing the inertial response of synchronous generators based on frequency changes. Therefore, they can simulate the ability to store or release kinetic energy just like a synchronous generator. VSMs that follow this model operate connected to the power grid, thus requiring the use of a PLL to obtain the grid phase angle. The control strategies that use this model include the Virtual Synchronous Generator (VSG) and the Virtual Synchronous Control (VSYNC) topology.

2.1.3.1 Virtual Synchronous Generator

A VSG consists of an energy storage element, a converter, and a control strategy that makes the DC source be seen by the grid as a synchronous generator from the perspective of inertia and damping properties [59].

In Figure 2-8, the control block diagram of the VSG is shown, and in (2.23) the active power output of the VSG, P_{VSG} , is presented, where $d\Delta\omega/dt$ is the rate of change of angular velocity, K_{dp} and K_i are the constants that emulates the damping and inertial characteristics, respectively.

 $\begin{array}{c|c} P_{VSG} \rightarrow I_d^* & I_d^* & Current \\ (2.23) & controller \\ (2.24) & A\omega \end{array}$

Figure 2-8 – Control block diagram of the VSG.

Source: Adapted from [9].

$$P_{VSG} = K_{dp} \Delta \omega + K_i \left(\frac{d\Delta \omega}{dt}\right) \tag{2.23}$$

After calculating P_{VSG} , the current references are calculated, and the injected current vector \vec{t} is controlled in the synchronous dq reference frame. Equation (2.24) shows the calculation of the current reference I_d^* , where v_d and v_q are the voltages at the PCC in dq coordinates. Since only the active power is regulated, the q-axis current reference I_q^* and Q are both zero.

$$I_d^* = \frac{2}{3} \left(\frac{v_d P_{VSG}}{v_d^2 + v_q^2} \right) \tag{2.24}$$

In Table 2-7, the main advantages and disadvantages of the VSG are presented.

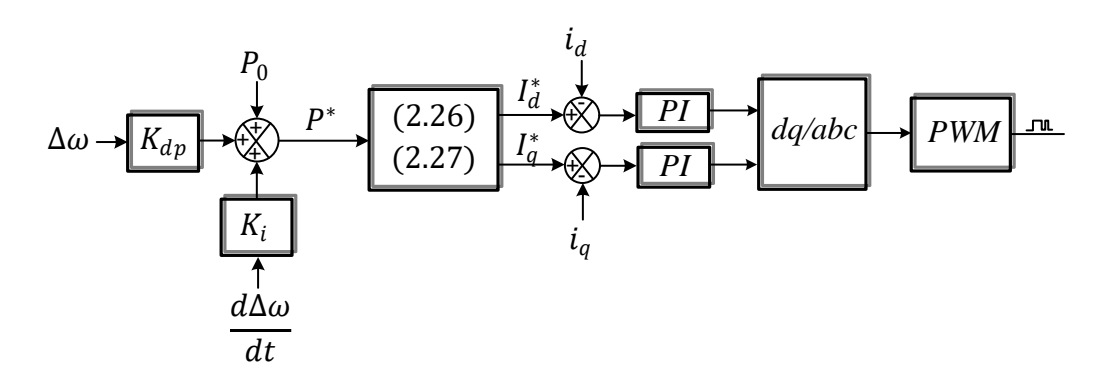
Table 2-7 – Advantages and disadvantages of the VSG.

Advantages	Disadvantages	
Simple implementation	Susceptible to noise due to the use of frequency derivative	
Low computational effort	Islanded operation not supported	
Overcurrent protection	PLL required	
	Reactive power control not supported	

2.1.3.2 Virtual Synchronous Control Topology

This topology was developed by the VSYNC research group [60], and they proposed an approach to emulate the behavior of a synchronous generator in converters by adding an energy storage element. This strategy performs synchronous generator emulation based on a PLL. The control block diagram of this topology is shown in Figure 2-9.

Figure 2-9 – Control block diagram of the VSYNC topology.



Source: Adapted from [43].

This topology does not implement reactive power control, and the system dynamics are described by (2.25)-(2.27).

$$P^* = P_0 + K_{dp} \Delta \omega + K_i \left(\frac{d\Delta \omega}{dt}\right)$$
 (2.25)

$$I_d^* = \frac{2}{3} \left(\frac{v_d P^*}{v_d^2 + v_q^2} \right) \tag{2.26}$$

$$I_q^* = \frac{2}{3} \left(\frac{v_q P^*}{v_d^2 + v_q^2} \right) \tag{2.27}$$

The variable P_0 is directly related to the energy storage element and is defined as (2.28), where K_{SOC} must be chosen such that the converter's nominal output power equals P^* when the State of Charge (SOC) deviation Δ_{SOC} of the energy storage element reaches its maximum level.

$$P_0 = K_{SOC}(\Delta_{SOC}) \tag{2.28}$$

In [61], the authors implemented an Energy Management System (EMS) to enable multiple converters to support the grid proportionally, without supervisory control or communication.

In Table 2-8, the main advantages and disadvantages of the VSYNC topology are presented.

Table 2-8 – Advantages and disadvantages of the VSYNC topology.

Advantages	Disadvantages	
Simple implementation	Susceptible to noise due to the use of frequency derivative	
Low computational effort	Islanded operation not supported	
Overcurrent protection	PLL required	
	Reactive power control not supported	

Source: Author.

Table 2-9 presents a summary of the techniques discussed, highlighting their main advantages and disadvantages, as well as their applicability as either GFM or GFL converters.

Table 2-9 – Summary of VSM emulation techniques.

Technique	Advantages	Disadvantages	Applicability
VISMA	 Overcurrent protection. High-fidelity emulation of synchronous-machine behavior. No PLL required. 	 High computational effort. Complex model and requires the synchronous machine's constructive parameters. 	GFM
IEPE Topology	 Enables islanded operation without hardware modification. Accurate synchronous-machine emulation. No PLL required. 		
Synchronv erter	 Capable of islanded operation. Faithful emulation of synchronous generator dynamics. Operates without PLL. Well established in the literature. 	 High computational demand. Possible numerical instability. Lacks overcurrent protection in some implementations. 	GFM
KHI Topology	Simple implementation.Overcurrent protection.	PLL required.Needs switching between grid-connected and islanded modes.	GFM
ISE Laboratory Topology	• Simplified replication of synchronous generator dynamics.	No overcurrent protection.Possible oscillations if parameters are not properly	GFM

	• Supports islanded operation.	tuned.	
SPC	 Simple structure and implementation. No PLL required. Provides overcurrent protection. Supports islanded operation. 	 Inherent frequency droop in its original form. Requires accurate tuning of multiple loops. 	GFM
VSG	 Simple implementation. Low computational effort. Overcurrent protection. 	 Sensitive to measurement noise. Limited reactive-power control. Requires PLL. Cannot operate in islanded mode. 	GFL
VSYNC Topology	 Simple implementation. Overcurrent protection. 	 Sensitive to measurement noise. Limited reactive-power control. Requires PLL. Cannot operate in islanded mode. 	GFL

2.2 State of the Art

Control strategies for power control in AC systems have been extensively studied over past years. The concept of GFM inverter is not new, since the authors in [22] have already proposed a strategy to control inverters operating in parallel in standalone AC supply systems, specifically in Uninterruptible Power Supply (UPS) systems.

More recently, new strategies have emerged, with droop control standing out as one of the

most widely used. This strategy adjusts P/Q power output based on local frequency/voltage deviations (P-f and Q-V droops), enabling decentralized load-sharing among distributed resources without communication. In this context, a wireless controller is proposed in [62] with three nested loops to achieve stable output impedance and proper power balance in parallel-connected UPS inverters. The controller ensures good-quality output voltage waveforms, effective harmonic power sharing, and minimal frequency and amplitude deviations during load transients. However, this strategy only considers the operation of two inverters in parallel without connection to the power grid. In [63], the method relies on feeder current sensing and virtual impedance for islanded microgrids, where current measurements are used to estimate the feeder impedance of distributed generation units. However, since real microgrids exhibit feeder impedances that can vary over time due to configuration changes, this strategy depends on accurately measuring a parameter that is inherently time-varying. Furthermore, this strategy does not consider operation under grid-connected conditions.

The previously mentioned papers utilize virtual impedance, which aims to shape the output impedance of the converter and provides several advantages [64], such as power flow control [65], grid fault/disturbance ride-through [66], harmonic/unbalance compensation [67], and enhanced stability and robustness of the converters in response to varying grid and load conditions [68]. In fact, virtual impedance has been widely used over the years in conjunction with other control strategies for power control of GFM inverters, due to the advantages previously mentioned. However, droop control is not exclusive to this, and more recent techniques, particularly virtual synchronous machines, which is the focus of this thesis, are also seeing widespread adoption. This adoption is mainly driven by characteristics of damping and inertia, similar to those exhibited by synchronous machines. The following presents various control strategies proposed in recent years for GFM inverters, including those based on VSMs.

In [69], an active-damping control method based on self- and mutual-damping controllers to attenuate both self- and mutually induced low-frequency power oscillations was proposed. This method improved the damping ratio and inertial response of multiple grid-tied VSMs, thereby supporting grid frequency stability. In [70], it was proposed a virtual inductance control strategy based on energy conservation principles to mitigate the unstable oscillation of frequency and powers, which differs from conventional virtual inductance strategies in that it does not dependent on a dual-loop control architecture. In [71], it was implemented virtual reactance instead of using

virtual resistance to dampen the low-frequency resonance of the GFM inverter. It is revealed that the passivity index can be enhanced by increasing the coupling inductance, and adding virtual reactance is an effective way to achieve this. The work presented in [72] adopted a different approach based on artificial intelligence to predict oscillation modes and enhance the damping of electromechanical inter-area oscillations, thereby improving system stability and ensuring robust performance under grid variations. Basically, the strategy presented in [73] aims to predict and adaptively tune a dedicated loop of the SPC to damp oscillations and enhance system stability. In [74], it was proposed a control strategy using virtual damping for enhancing the system damping and virtual reactance to suppress oscillations without altering the synchronverters' fundamental characteristics. In [75], it was proposed a strategy based on virtual damper winding applied to GFM inverter to decrease the low-frequency oscillations, utilizing existing state variables without requiring a PLL. In [76], it was proposed a generic voltage control scheme for GFM inverters that enhances voltage tracking and power regulation in both grid-tied and stand-alone modes, addressing conflicts in power loop dynamics and improving overall system stability and performance. In the papers mentioned before, the investigation was carried out almost entirely on the power control loops, without a deep analysis of the inner loops to improve the dynamic response of the GFM inverter.

In addition to control strategies that use internal current and voltage control loops, there are also strategies known as open-loop control [31], [32], [36]. These strategies, although simpler to implement since there is no need to tune the internal loops, have the disadvantage of being more prone to overload ride-through problems and can even become unstable when connected to strong grids [31], [77].

The inner control loops and the power control loops interact with each other, which might lead to unsatisfactory power control dynamics. The interaction between these loops can cause two types of oscillation: synchronous and subsynchronous. Synchronous oscillations are oscillations at fundamental frequency, and subsynchronous oscillations are oscillations below the fundamental frequency [71], [78]. This PhD thesis proposes a VSM with internal current and voltage control loops. However, it is known from [79] that subsynchronous oscillations can arise in strong grids due to interactions between the internal voltage control loop and the external *P* and *Q* control loops.

Therefore, based on what has been presented, there is a gap in the literature regarding the

improvement of the dynamic response of VSMs, focusing on enhancing their inner loops (voltage and current) to improve the dynamic response of the VSM and enable it to provide ancillary services to the grid. Additionally, it is necessary to improve the performance of the VSM both when connected to the grid and operating autonomously. It is also important to analyze the operation of the VSM in a microgrid, considering not only the VSM functioning with the grid but also its interaction with other elements that constitute it, such as other converters.

2.3 Chapter Summary

This chapter initially provided a literature review on VSMs. Based on the common characteristics they share, these systems were classified in groups, where the particularities of each were presented, along with their advantages and disadvantages.

The chapter reviewed the state of the art in control strategies for GFM inverters. It emphasized the importance of improving the performance of the inner loops—such as the voltage and current controllers—to enhance the overall dynamic response of VSMs and improve their ability to provide ancillary services to the grid.

Moreover, it is crucial to enhance VSM performance, not only when they are connected to the grid but also during isolated operation. Additionally, the chapter emphasized the need to examine how the VSM operates within a microgrid, considering not just its interaction with the grid but also its connection with other components that make up the system.

CHAPTER III

3 Virtual Synchronous Machine Control – Inverter Side

This chapter presents the control strategy for the VSM on the inverter side. It includes the modelling of the converter's inner control loops, as well as the outer loop. The following chapter introduces the control strategy for the DC bus.

3.1 Introduction

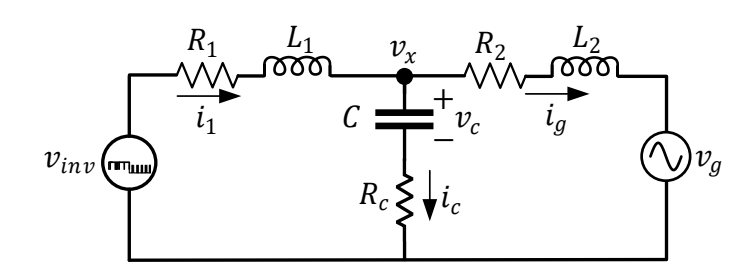
Power electronic converters are pivotal in interfacing RESs with the electrical grid, enabling efficient power transfer while adhering to grid codes [80]. However, they face significant challenges in real-world scenarios, particularly due to voltage harmonics at the PCC and variations in grid impedance, which can degrade performance and stability [81].

In grid-connected converters, LCL filters are favored over L filters due to their enhanced harmonic attenuation and reduced inductance size requirements [82]. Nevertheless, the LCL filter introduces an inherent resonance peak at its resonance frequency f_r , accompanied by a sharp phase drop of -180° [83]. This resonance can lead to oscillations in the injected current and, in more extreme cases, to instability.

3.2 LCL Filter Modelling

Figure 3-1 shows the single-phase equivalent circuit of a three-phase LCL filter, which serves as the interface between the converter and the power grid. The variables presented are as follows: v_{inv} , the modulated output voltage of the converter; L_1 and L_2 , the inductances on the converter side and the grid side, respectively; R_1 and R_2 , the equivalent series resistances (ESR) of L_1 and L_2 , respectively; C, the filter capacitance; R_C , the ESR of C; v_g , the grid voltage; v_c , the voltage across the capacitor; i_1 , the current through L_1 ; i_g , the current injected into the grid and i_c , the current through the capacitor.

Figure 3-1– Single-phase equivalent circuit of the LCL filter.



By applying Kirchhoff's Voltage Law to the left side of the circuit shown in Figure 3-1, (3.1) is obtained:

$$v_{inv}(s) = R_1 i_1(s) + L_1 s i_1(s) + v_x(s)$$
(3.1)

Where $v_x(s)$ is given by (3.2).

$$v_x(s) = (R_c + \frac{1}{sC})i_c(s)$$
(3.2)

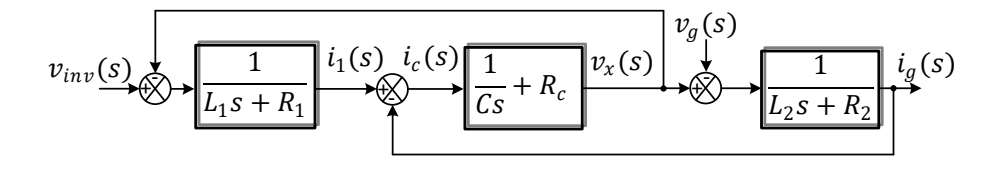
By applying Kirchhoff's Current Law, (3.3) is obtained, and by applying Kirchhoff's Voltage Law to the right side of Figure 3-1, (3.4) is obtained.

$$i_c(s) = i_1(s) - i_g(s)$$
 (3.3)

$$i_g(s) = \frac{1}{L_2 s + R_2} [v_x(s) - v_g(s)]$$
(3.4)

From the previously derived equations, the block diagram representing the LCL filter model can be obtained, as shown in Figure 3-2.

Figure 3-2 – Block diagram of the LCL filter model.



Source: Author.

After several mathematical manipulations of Equations (3.1)-(3.4), the transfer functions relating $i_1(s)/v_{inv}(s)$ and $i_g(s)/v_{inv}(s)$ can be obtained, given by (3.5) and (3.6), respectively.

$$\frac{i_1(s)}{v_{inv}(s)}_{v_g=0} = \frac{CL_2s^2 + C(R_2 + R_c)s + 1}{s^3(L_1L_2C) + s^2C[L_1(R_c + R_2) + L_2(R_c + R_1)] + s[L_1 + L_2 + C(R_cR_1 + R_cR_2 + R_1R_2)] + (R_1 + R_2)}$$
(3.5)

$$\frac{i_g(s)}{v_{inv}(s)_{v_g=0}} = \frac{CR_c s + 1}{s^3 (L_1 L_2 C) + s^2 C [L_1 (R_c + R_2) + L_2 (R_c + R_1)] + s[L_1 + L_2 + C (R_c R_1 + R_c R_2 + R_1 R_2)] + (R_1 + R_2)}$$
(3.6)

3.3 LCL Filter Resonance and Damping Techniques

3.3.1 Resonance Effect

Figure 3-3 shows the frequency response of the transfer function $i_g(s)/v_{inv}(s)$, for the parameters shown in Table 3-1. The per-unit system uses the base values $S_B = 11 \, kVA$ as the three-phase apparent power base, $V_{B,f} = 220 \, V$ as the base phase voltage (line-to-neutral), and $f_B = 60 \, Hz$ as the base frequency. The ESR values of the components were neglected, as the worst-case damping scenario is considered.

Figure 3-3 shows a high magnitude peak at f_r , with its value in Hz given by (3.7), as well as a sharp phase shift that causes a pair of right-half-plane poles in the closed-loop when the phase angle reaches -180° [84]. Resonance is an undesired effect, as it indicates low filter impedance at f_r ; therefore, the converter must not excite the resonance, since this can even lead to instability of the entire system. To ensure stability, the magnitude peak at f_r should be damped below 1 (S).

$$f_r = \frac{1}{2\pi} \sqrt{\frac{L_1 + L_2}{L_1 L_2 C}} \tag{3.7}$$

Table 3-1 − LCL filter parameters.

Parameter	Value (real)	Value (pu)
L_1	1 mH	0.028
L_2	300 μΗ	0.008
С	15 μF	0.074

Source: Author.

Frequency (Hz): 2.71e+03
Mag. (abs): 6.6e+05

Mag. -135

-270

10

Frequency (Hz): 2.71e+03

Mag. (abs): 6.6e+05

10

Frequency (Hz): 2.71e+03

10

Figure 3-3 – Frequency response of the LCL filter $(i_g(s)/v_{inv}(s))$.

3.3.2 Resonance Damping Techniques

There are basically two ways to dampen the resonance produced by the LCL filter: passive damping and active damping. The first strategy involves the insertion of a resistor into the filter, which can be done in several ways (a resistor in series or in parallel with L_1 , C ou L_2), but one of the most used methods is the addition of a resistor in series with the capacitor. The second strategy is based on control algorithms, which can be implemented in two ways: 1 – by inserting a transfer function in cascade with the closed-loop plant transfer function, or 2 – by feeding back plant states into the closed-loop control diagram. These two forms of active damping will be detailed later.

3.3.2.1 Passive Damping

As previously mentioned, this strategy can be based on the addition of a damping resistor, R_d , in series with C. According to [85], the value of R_d can be calculated using (3.8).

$$R_d = \frac{1}{6\pi f_r C} \tag{3.8}$$

Figure 3-4 presents the frequency response of a generic LCL filter, $i_g(s)/v_{inv}(s)$, for different values of R_d , to observe its influence.

It can be observed from Figure 3-4 that R_d was varied between 0Ω e 5Ω , and that its

increase leads to a reduction in the resonance peak. The value of 5 Ω corresponds to 37.8 % of the base impedance, or 0.378 pu. In other words, it positively affects the influence of resonance. However, it can also be seen that in the high-frequency region, the filter's admittance increases as R_d increases, which means a reduction in the attenuation of high-frequency harmonic components. Another drawback of using passive damping is the increase in circuit losses, since the resistor dissipates power.

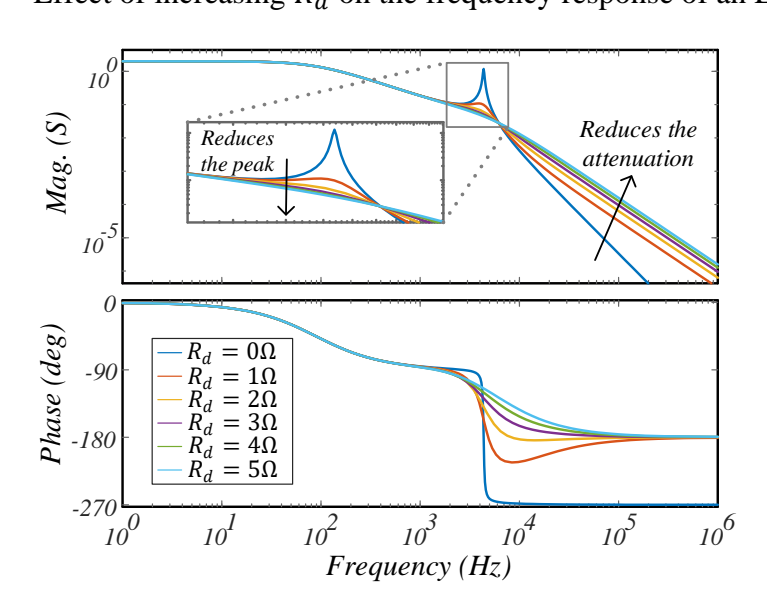


Figure 3-4 – Effect of increasing R_d on the frequency response of an LCL Filter.

Source: Author.

3.3.2.2 Active Damping

3.3.2.2.1 Cascaded Transfer Function

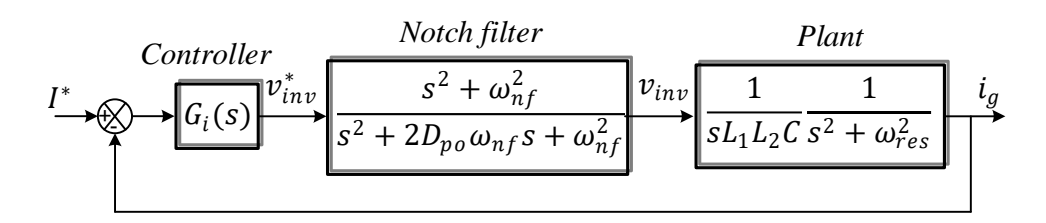
One of the active damping solutions is the insertion of a transfer function in cascade with the transfer function of the LCL filter, with the aim of cancelling out the effects of the plant's resonant poles. This function is known in the literature as a Notch filter and is defined in (3.9) [86]:

$$N_n(s) = \left(\frac{s^2 + 2D_z \omega_{nf} s + \omega_{nf}^2}{s^2 + 2D_{po} \omega_{nf} s + \omega_{nf}^2}\right)^n$$
(3.9)

Where ω_{nf} is the Notch frequency, D_z and D_{po} are the damping factors for the complex conjugate zeros and poles, respectively, and n is the number of sections.

In digital implementations, $D_z = 0$ to force the complete cancellation of the low-damped resonant poles of the filter. Figure 3-5 shows the block diagram for i_g control using the Notch filter as active damping. The function $G_i(s)$ represents a current controller, which will be discussed in more detail throughout this work, and ω_{res} represents the resonance frequency of the LCL filter in rad/s.

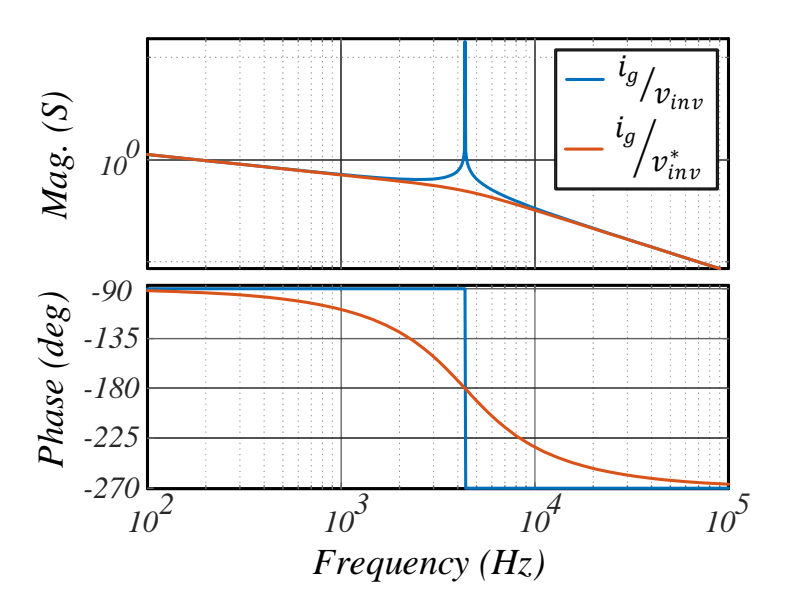
Figure 3-5 – Block diagram of i_g control using the Notch filter.



Source: Author.

Figure 3-6 shows the frequency response of the plant transfer function $i_g(s)/v_{inv}(s)$ and the transfer function of the Notch filter with the plant $i_g(s)/v_{inv}^*(s)$. It can be observed that with the use of the filter, the resonance effect was mitigated, and the issue of reduced high-frequency attenuation—present in passive damping—did not occur.

Figure 3-6 – Frequency response of the system with and without the Notch filter.



Source: Author.

It is worth noting that ω_{res} must be accurately known for the Notch filter to function

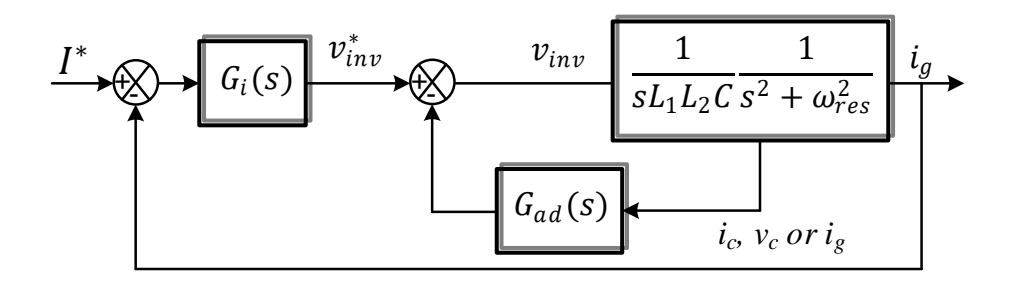
properly. However, due to parameter variations in the filter components or changes in the grid impedance, the exact cancellation of the resonant poles may not occur, which can result in an ineffective strategy in practice. To address this issue, ω_{res} should be detected online so that ω_{nf} can be accordingly selected. Reference [87] presents a methodology for detecting ω_{res} .

3.3.2.2.2 State Feedback of the Plant

Active damping solutions based on plant state feedback are primarily built upon the use of one of the following signals: feedback of i_c , v_c or i_g . In [83], it is shown that a resistor in parallel with C appears to be the most effective form of passive damping. Based on this premise, expressions for active damping solutions are derived so that they are equivalent to virtually placing a resistor in parallel with C.

It is demonstrated that feedback of i_c , v_c or i_g provides damping to the system when each of these states is used as the input to a feedback function $G_{ad}(s)$. For $i_c(s)$, $v_c(s)$ and $i_g(s)$, $G_{ad}(s)$ can be a constant, a differentiator, or a second-order differentiator, respectively [83]. Figure 3-7 shows the generic block diagram for i_g control using plant state feedback.

Figure 3-7 – Block diagram of i_g control using state feedback as active damping.



Source: Author.

Figure 3-8 shows the frequency response of the system presented in Figure 3-7, comparing the cases with and without i_c feedback as an active damping strategy. With i_c feedback, the transfer function is $i_g(s)/v_{inv}^*(s)$, while without i_c feedback, the transfer function is $i_g(s)/v_{inv}(s)$. As was shown for the Notch filter, it can be observed that i_c feedback also attenuated the resonance effect and did not reduce the filter's high-frequency attenuation. For this case, $G_{ad}(s) = 2D_{po}\omega_{nf}L_1$.

(S) (S)

Figure 3-8 – Frequency response of the system with and without i_c feedback.

3.4 Effect of Computational Delay on Active Damping Through Capacitor Current Feedback

In the previous section, some active damping techniques for mitigating the effect of resonance in LCL filters were shown and analyzed. However, computational delay was not considered and cannot be disregarded in digitally controlled systems. In this section, the influence of computational delay on capacitor current feedback active damping (CCFAD) is analyzed.

3.4.1 Delay Model

The delay can be modelled as a function of the control processing time and the digital PWM modulation. Considering symmetric sampling, the delay due to control processing is in general one sampling period, T_s , and the delay introduced by the PWM is $0.5T_s$, totaling $T_{delay} = 1.5T_s$. With these considerations, the delay function, $G_d(s)$, is modelled as (3.10) [88].

$$G_d(s) = e^{-1.5sT_s} (3.10)$$

The model presented in (3.10) is unsuitable for analysis using classical control tools, such as root locus and frequency response, as it is a non-linear function. Therefore, the delay $G_d(s)$ was approximated using the first-order Padé approximation with a zero in the right half-plane [89],

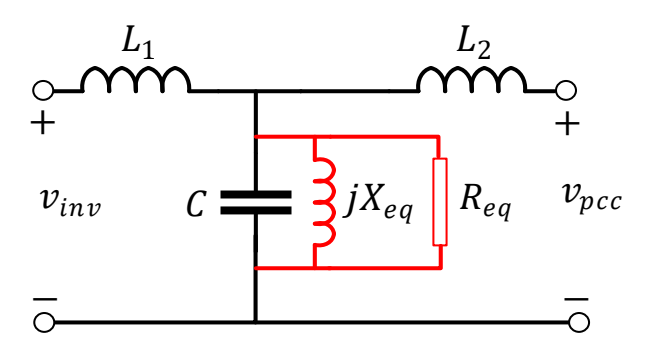
given by (3.11).

$$G_d(s) \cong \frac{1 - sT_{delay}/2}{1 + sT_{delay}/2} \tag{3.11}$$

3.4.2 The Delay and the Capacitor Current Feedback Active Damping

CCFAD is a simple and commonly used approach to mitigate the LCL filter resonance. However, when CCFAD is implemented in control systems, the inherent delay causes it to behave as if a virtual impedance Z_v is inserted in parallel with C [83]. Figure 3-9 shows the equivalent circuit, where R_{eq} is the equivalent resistor, X_{eq} is the equivalent reactance, and v_{pcc} is the voltage at the PCC.

Figure 3-9 – Equivalent circuit.



Source: Adapted from [83].

The expression of Z_v is given by (3.12) [90].

$$Z_v = \frac{L_1}{CK_{ad}} e^{1.5T_S s} (3.12)$$

Being K_{ad} the proportional gain of CCFAD, in other words, $G_{ad}(s) = K_{ad}$ for this case. Making $s = j\omega$ into (3.12), yields to (3.13).

$$Z_v(j\omega) = \frac{jX_{eq}(\omega)R_{eq}(\omega)}{R_{eq}(\omega) + X_{eq}(\omega)} = \frac{L_1}{CK_{ad}}\cos(1.5\omega T_s) + j\frac{L_1}{CK_{ad}}\sin(1.5\omega T_s)$$
(3.13)

By analyzing (3.13), (3.14) and (3.15) are obtained:

$$R_{eq}(\omega) = \frac{L_1}{CK_{ad}\cos(1.5\omega T_s)}$$
(3.14)

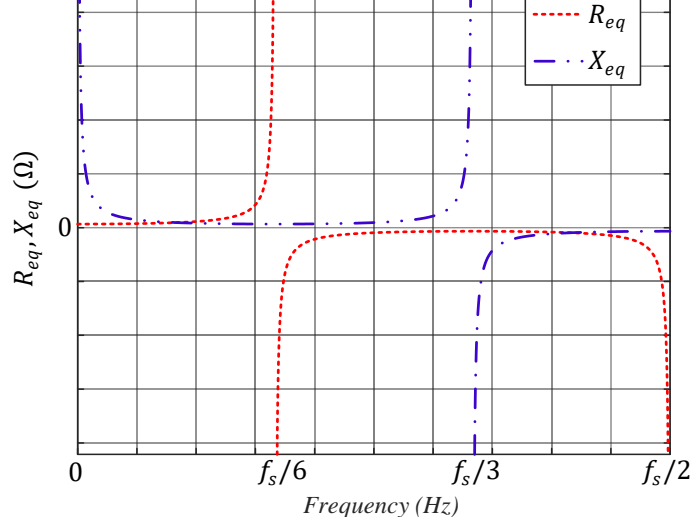
$$X_{eq}(\omega) = \frac{L_1}{CK_{ad}\sin(1.5\omega T_s)}$$
(3.15)

According to these equations, it can be observed that R_{eq} is positive in the range $(0, f_s/6)$ and negative in the range $(f_s/6, f_s/2)$, where f_s is the sampling frequency. It is also observed that X_{eq} is inductive in the range $(0, f_s/3)$ and capacitive in the range $(f_s/3, f_s/2)$. Figure 3-10 shows the plot of R_{eq} and X_{eq} , and it is possible to observe the behavior described in the previous statements. The region with negative resistance leads to the insertion of open-loop unstable poles at the current loop [91].

The work presented in [92] shows that if the f_r of the LCL filter is above $f_s/6$, the use of active damping techniques is not necessary. However, the value of the line impedance, which is in series with L_2 , may change, consequently altering the value of f_r and moving it into a prohibited region.

Figure 3-10 – Plot of R_{eq} and X_{eq} as a function of frequency.

 \overline{R}_{eq} X_{eq}



Source: Author.

3.5 Passivity

This section will introduce the concept of passivity as applied to power converters, which will be important for the subsequent analysis of the proposed enhanced current control strategy.

Passivity in control systems is an energy-based property, where a system is said to be passive if it does not generate more energy than it receives [93]; this characteristic makes passivity the foundation for passivity-based control, which emerges as an alternative to provide sufficient conditions for the stability of complex systems, regardless of the configuration or the number of converters connected to the grid.

The passivity theory in the frequency domain states that a linear system G(s) is passive if the following conditions are satisfied [94]:

- 1. $Re\{p_i\} \leq 0, i = 1, ..., n$
- 2. $Re\{G(j\omega)\} \ge 0, \forall \omega$
- 3. $-\pi/2 \le \angle G(j\omega) \le \pi/2$

where p_i are the poles of G(s), and ω is the frequency.

The block diagram shown in Figure 3-11 (which considered a simplified L filter) will serve as the basis for the analysis of the passivity concept, and the analysis to be presented follows the approach used in [95]. It is emphasized that the dynamics of the DC link were neglected. Here, $G_{ff}(s)$ is the voltage decoupling function, and Z_q is the grid impedance.

The block diagram in Figure 3-11 can be represented by the equivalent impedance-admittance model shown in Figure 3-12, where $G_{CL}(s)$ is the internal closed-loop transfer function that relates $i_g(s)/I^*(s)$ and Y(s) is the input admittance as "seen" from the PCC.

Applying Kirchhoff's voltage law to Figure 3-12 yields (3.16):

$$i_g(s) = \frac{G_{CL}(s)}{1 + Z_g(s)Y(s)}I^*(s) - \frac{Y(s)}{1 + Z_g(s)Y(s)}v_g(s)$$
(3.16)

Figure 3-11– Circuit for passivity analysis.

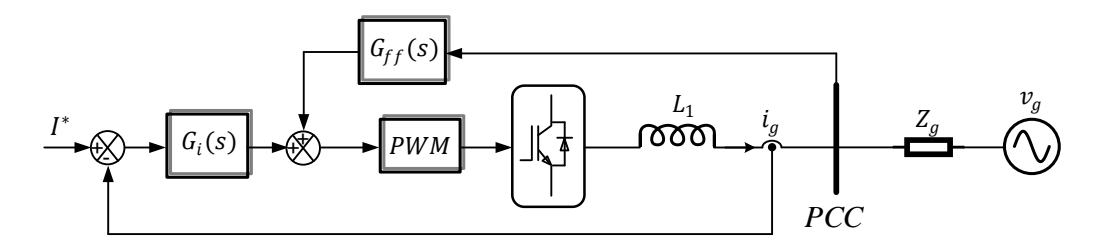
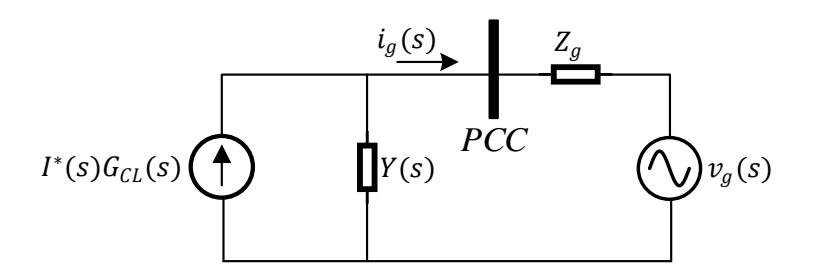


Figure 3-12 – Equivalent impedance-admittance model.



Source: Author.

The closed-loop stability (Figure 3-12) can be analyzed by applying the Nyquist criterion to the open-loop transfer function $Y(s)Z_g(s)$ in (3.16). Therefore, an expression for Y(s) must be obtained, since $Z_g(s)$ is passive as it consists of passive elements.

Equation (3.17) and (3.18) can be derived by analyzing Figure 3-11and Figure 3-12, respectively.

$$G_{CL}(s) = \frac{G_i(s)e^{-sT_{delay}}}{sL_1 + G_i(s)e^{-sT_{delay}}}$$
(3.17)

$$Y(s) = \frac{G_{CL}(s)I^{*}(s) - i_{g}(s)}{v_{pcc}(s)}$$
(3.18)

By substituting (3.17) into (3.18), (3.19) is obtained:

$$Y(s) = \frac{G_i(s)e^{-sT_{delay}}[I^*(s) - i_g(s)] - sL_1i_g(s)}{v_{pcc}(s)(sL_1 + G_i(s)e^{-sT_{delay}})}$$
(3.19)

From Figure 3-11, (3.20) can be obtained, and substituting (3.20) into (3.19) yields (3.21):

$$v_{pcc}(s) = \frac{G_i(s)[I^*(s) - i_g(s)]e^{-sT_{delay}} - sL_1 i_g(s)}{1 - G_{ff}(s)e^{-sT_{delay}}}$$
(3.20)

$$Y(s) = \frac{1 - G_{ff}(s)e^{-sT_{delay}}}{sL_1 + G_i(s)e^{-sT_{delay}}}$$
(3.21)

The passivity method will be analyzed considering a proportional controller K and $G_{ff}(s) = 0$. Therefore, (3.21) can be rewritten as (3.22):

$$Y(j\omega) = \frac{1}{\{K\cos(\omega T_{delay}) + j[L_1\omega - K\sin(\omega T_{delay})]\}}$$
(3.22)

By multiplying (3.22) by the complex conjugate in the numerator and denominator, we obtain (3.23):

$$Y(j\omega) = \frac{K\cos(\omega T_{delay}) - j[L_1\omega - K\sin(\omega T_{delay})]}{\left\{K^2\cos^2(\omega T_{delay}) + [L_1\omega - K\sin(\omega T_{delay})]^2\right\}}$$
(3.23)

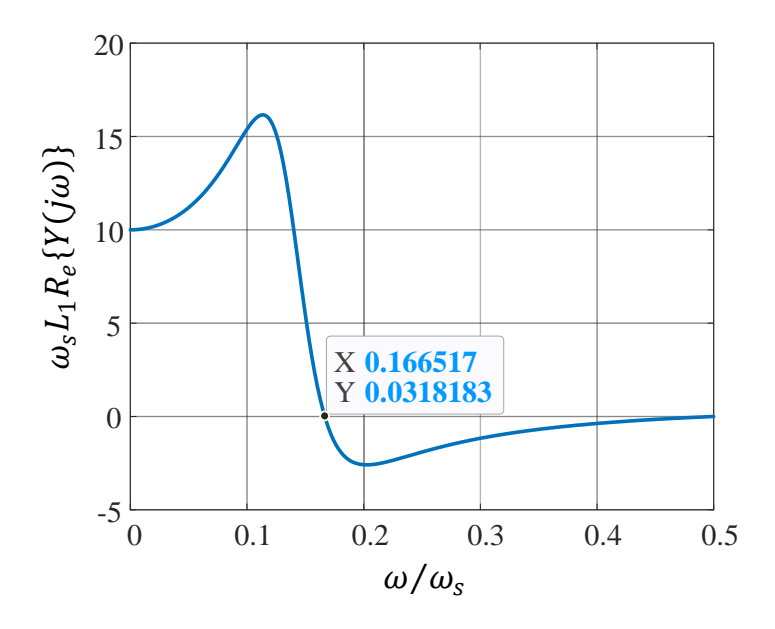
The real part of (3.23) is shown in (3.24):

$$R_e\{Y(j\omega)\} = \frac{K\cos(\omega T_{delay})}{\left[K^2 + L_1^2\omega^2 - 2L_1\omega K\sin(\omega T_{delay})\right]}$$
(3.24)

Applying the passivity condition $R_e\{Y(j\omega)\} \ge 0$, it can be observed that this condition is satisfied when $\omega T_{Delay} \le \frac{\pi}{2}$. Since $T_{delay} = 1.5T_s$, the system is passive for all $\omega \le \frac{\omega_s}{6}$, where ω_s is the sampling frequency in rad/s.

Figure 3-13 shows the normalized real part of Y(s) as a function of normalized ω . It can be observed that from approximately $\omega_s/6$ onward, the function presents negative values up to the Nyquist frequency. Therefore, the system would be unstable for resonance frequencies in the range $\omega_s/6 \le \omega_{res} \le \omega_s/2$, where ω_{res} is the resonance frequency in rad/s.

Figure 3-13 – $R_e\{Y(j\omega)\}$ as a function of ω .



It can be observed that the frequency $\omega_s/6$ appears as a critical frequency for ensuring stability; therefore, the passivity region must be extended to improve robustness of stability against variations in grid impedance. One way to increase this region is to consider a proportional controller K and $G_{ff}(s) = sT$, where T is an arbitrary constant [95]. Equation (3.21) is then rewritten as (3.25):

$$Y(j\omega) = \frac{\left[1 - j\omega T \times \cos(\omega T_{delay}) - \omega T \times \sin(\omega T_{delay})\right] \times \left\{K\cos(\omega T_{delay}) - j\left[\omega - K\sin(\omega T_{delay})\right]\right\}}{\left\{K^{2}\cos^{2}(\omega T_{delay}) + \left[\omega L_{1} - K\sin(\omega T_{delay})\right]^{2}\right\}}$$
(3.25)

The real part of (3.25) is given by (3.26):

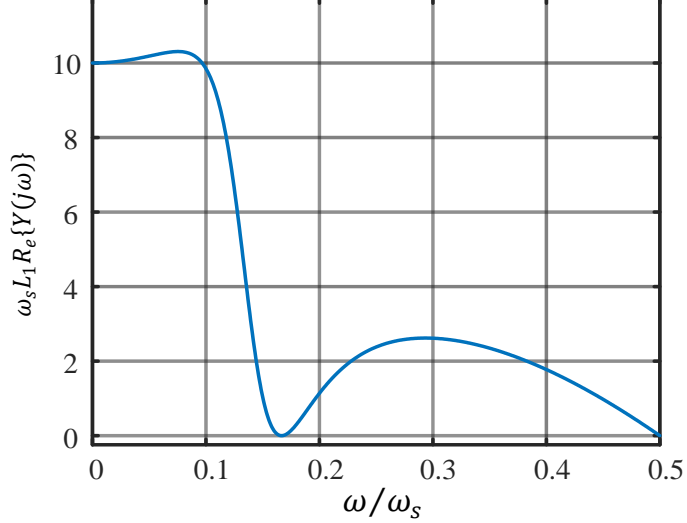
$$R_e\{Y(j\omega)\} = \frac{(K - \omega^2 T L_1) \times \cos(\omega T_{delay})}{\left[K^2 + \omega^2 L_1^2 - 2\omega L_1 K \sin(\omega T_{delay})\right]}$$
(3.26)

The sign change in (3.26) occurs at $\omega = \frac{\pi}{2T_{delay}}$. Therefore, the parameter T can be chosen to shift this sign change, which occurs under the condition given in (3.27):

$$(K - \omega^2 T) = 0 \Rightarrow T = \frac{4KT_{delay}^2}{\pi^2 L_1}$$
(3.27)

Figure 3-14 shows the normalized real part of Y(s) as a function of normalized ω , with the gain T adjusted accordingly. It can be observed that with $G_{ff}(s)$ included, the system became stable for all $\omega \leq \omega_s/2$.

Figure 3-14 – $R_e\{Y(j\omega)\}$ as a function of ω with $T = \frac{4KT_{delay}^2}{\pi^2L_1}$.



Source: Author.

3.6 Current Control Loop Design

This section presents the proposed current control strategy based on CCFAD and Capacitor Voltage Decoupling (CVD). The use of CCFAD aims to mitigate the effect of f_r , while the use of CVD is intended to enhance the converter's disturbance rejection capability.

3.6.1 System Description

The topology of the bidirectional GFM converter is shown in Figure 3-15. This converter is composed of two stages: one battery bank with a bidirectional DC-DC converter (this stage will be explained later), and a three-phase inverter. The inverter is connected to the grid through an LCL filter, where L_1 is the converter-side inductance, C is the filter capacitance and, L_2 is the grid-side inductance. The resistances R_1 and R_2 are the ESRs of L_1 and L_2 , respectively. Additionally, L_g represents the grid inductance and v_g represents the grid voltage.

Power calculation SPWM APC RPC $V_{c\alpha\beta} \longrightarrow G_{cvd}$ Curent Voltage Virtual controller controller impedan ce Generator LPF LPF Current controller Voltage controller Virtual impedance APCRPC

Figure 3-15 – Bidirectional GFM converter topology.

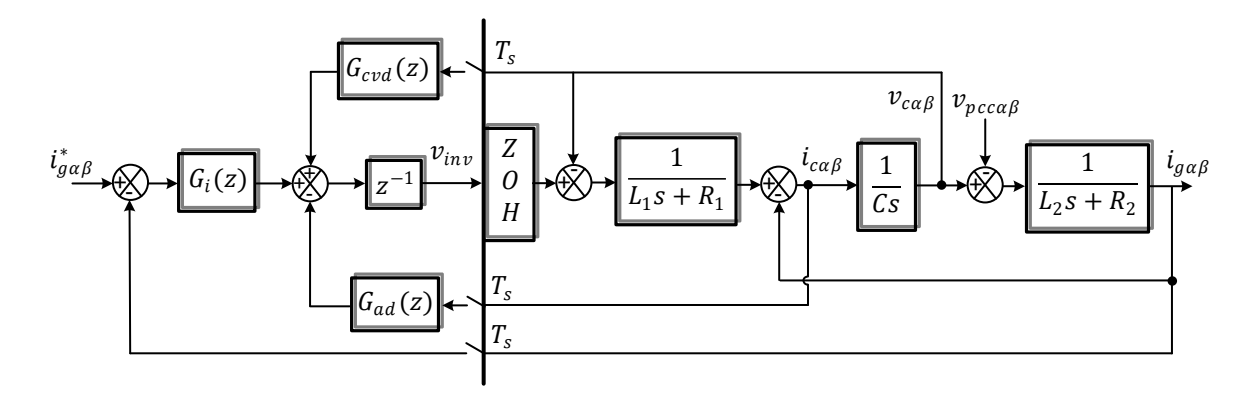
The control strategy used for the inverter is VSM. The outer control loops consist of the Active Power Controller (APC) and the Reactive Power Controller (RPC). The APC is responsible for regulating the active power P_e , with the active power reference denoted as P^* , and generates the phase reference θ as its output. The measured active power P_e is filtered by a low-pass filter (LPF) with a cutoff frequency of 100 Hz. The other parameters of this block, J, ω_n , ω and D_p , represent the moment of inertia, the rated rotor angular frequency, the actual rotor angular frequency, and the damping coefficient of active power-frequency, respectively. The RPC controls the reactive power Q_e , with the reactive power reference given by Q^* , and produces the amplitude of electromotive force of the VSM, E, at its output. The measured reactive power Q_e is also filtered by a LPF with a cutoff frequency of 100 Hz. The other parameters in this block, K, U_n , U and D_q , represent the regulator coefficient of reactive power, the effective value of the rated voltage amplitude, the effective value of the actual voltage amplitude, and the droop coefficient of reactive power voltage, respectively. The parameters θ and E define the reference voltages in the $\alpha\beta$ coordinate system, E_{α} and E_{β} , for the virtual impedance block. This block consists of a virtual resistance, R_V , and a virtual inductance, L_V . The output of this block generates the references $(v_{c\alpha}^*, v_{c\beta}^*)$ for the voltage controller. The capacitor voltage $v_{c\alpha\beta}$ is controlled through a PR

controller G_v , and a function G_{ff} is employed to improve the dynamics of the converter. The voltage controller generates the references $(i_{g\alpha}^*, i_{g\beta}^*)$ for the current controller. The injected current $i_{g\alpha\beta}$ is controlled through a lead compensator G_i , and the functions G_{ad} and G_{cvd} are used to mitigate the effect of f_r and to enhance the inverter's disturbance rejection capability, respectively.

3.6.2 Current Controller Design

As mentioned earlier, $i_{g\alpha\beta}$ is controlled by a lead compensator, whose transfer function is given by (3.28). R_a is the proportional gain, and k_L [96] is the lead gain designed to reduce the effects of computational delay. Figure 3-16 presents the block diagram of the current control loop. The computational delay is T_s , and it is modeled as z^{-1} in discrete time domain. The PWM delay is represented by the zero-order hold (ZOH).

Figure 3-16 – Control block diagram of the current loop.



Source: Author.

$$G_i(z) = \frac{R_a}{1 + k_l z^{-1}} \tag{3.28}$$

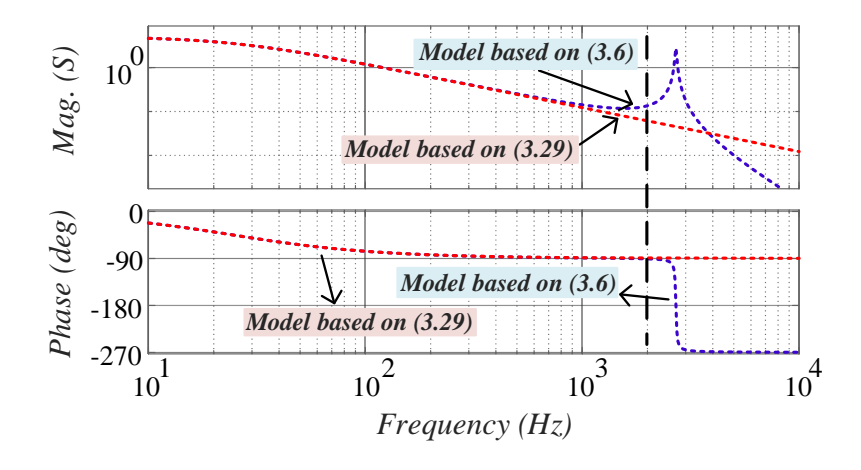
The LCL filter complete transfer function, relating the current i_g to the inverter terminal voltage v_{inv} , is given by (3.6). For easier tuning of R_a , the filter is approximated as an equivalent L-filter, with total inductance $L_T = L_1 + L_2$ and total ESR $R_T = R_1 + R_2$ [92]. The simplified transfer function is given by (3.29).

$$\frac{i_{gT}(s)}{v_{invT}(s)} = \frac{1}{L_T s + R_T}$$
 (3.29)

To validate this approximation, Figure 3-17 shows the frequency response of (3.6) (R_c) is

neglected) and (3.29). It can be noticed that up to a frequency of approximately 2 kHz, the models are equivalent. Therefore, the bandwidth of the current controller will be tuned for a bandwidth of 2 kHz.

Figure 3-17 – Open-loop frequency response of the LCL filter and the equivalent L filter.



Source: Author.

The plant parameters in the discrete-time domain, a and b, are given by (3.30) and (3.31), respectively. The closed-loop transfer function, shown in Figure 3-18, is given by (3.32). Defining the desired natural frequency ω_n and the damping factor ζ for the closed-loop system, the system's dominant poles, p_1 and p_2 , are calculated using (3.33), where $\omega_d = \omega_n \sqrt{1-\zeta^2}$. From these poles, the controller gains are calculated using (3.34) and (3.35) [97].

$$a = e^{-\left(\frac{R_T}{L_T}\right)T_S} \tag{3.30}$$

$$b = \frac{1-a}{R_T} \tag{3.31}$$

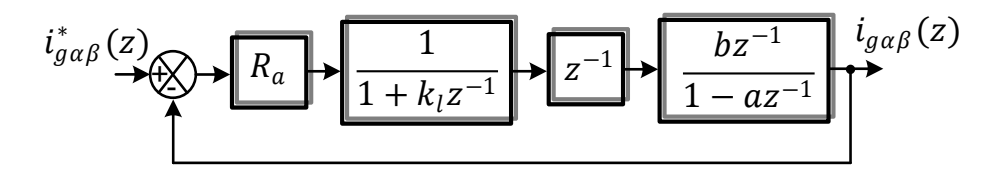
$$\frac{i_{g\alpha\beta}(z)}{i_{g\alpha\beta}^*(z)} = \frac{R_a b}{(z+k_l)(z-a) + R_a b}$$
(3.32)

$$p_{1,2} = e^{-\zeta \omega_n T_s} [\cos(\omega_d T_s) \pm j \sin(\omega_d T_s)]$$
(3.33)

$$k_1 = a - (p_1 + p_2) (3.34)$$

$$R_a = (p_1 p_2 + k_l a)/b (3.35)$$

Figure 3-18 – Closed-loop block diagram used for controlling $i_{g\alpha\beta}$.



As mentioned earlier, the current controller bandwidth was set to 2 kHz, with $\zeta = 0.9$ and $\omega_n = 2\pi \times 1650$ rad/s. The current controller gains are listed in Table 3-2.

Table 3-2 – Current Controller Gains.

Parameter	Value
R_a	5.6
k_l	0.27

Source: Author.

It is well known that achieving high control bandwidth is closely related to the converter power level and, consequently, its f_{sw} . For high-power converters, the f_{sw} is typically lower, and therefore a chosen bandwidth of, for example, 2 kHz may already correspond to the converter's own f_{sw} , making such bandwidth unattainable in practice.

Nevertheless, the lead compensation technique presented can still be applied to high-power converters in order to increase their achievable bandwidth, while respecting the limits imposed by the f_{sw} .

To clarify this effect, Table 3-3 presents the maximum bandwidths for which the closed-loop system exhibits only real poles, both without and with lead compensation. The results are shown for two f_{sw} : 3 kHz and 1 kHz.

The system model is an RL-type plant, with $R = 0.01 \Omega$ and $L = 408 \mu H$. These RL values were chosen to represent typical filter parameters in higher-power converters.

As can be observed, the maximum bandwidth that yields only real closed-loop poles without lead compensation decreases as the f_{sw} decreases (as in high-power systems). However, the use of lead compensation enables an increase in the achievable bandwidth even under such

low-switching-frequency conditions.

Table 3-3 – Comparison of Maximum Closed-Loop Bandwidths With and Without Lead Compensation Under Different Switching Frequencies.

	Without lead compensation	With lead compensation
$f_{sw} = 3 kHz$	370 Hz	817 Hz
$f_{sw} = 1 kHz$	114 Hz	274 Hz

Source: Author.

3.6.3 Capacitor Current Feedback Active Damping Design

To mitigate the LCL resonance, a first-order phase-lead compensator was implemented, and its transfer function is shown in (3.36), where τ_L and α_L are the compensation parameters.

$$G_{ad}(s) = \frac{1 + \tau_L s}{1 + \alpha_L \tau_L s} \tag{3.36}$$

The parameter τ_L is tuned according to (3.37), and the primary objective of $G_{ad}(s)$ is to achieve the maximum phase lead at the filter's resonance angular frequency $\omega_r = 2\pi f_r$. As a result, the value of ω_r is selected based on the filter parameters provided in Table 3-1. Figure 3-19 shows the frequency response of $G_{ad}(s)$ for different values of α_L is shown. As can be seen, as the value of α_L increases, the phase lead from f_r decreases, while the phase lead increases when α_L is decreased. However, decreasing the value of α_L leads to an increase in the gain at high frequencies, which is detrimental since it may amplify high-frequency noise. Taking this into account, $\alpha_L = 0.1$ is chosen as a balance between phase lead and limiting the gain at high frequencies [98], which results in a value of $\tau_L = 1.86 \times 10^{-4}$.

$$\tau_L = \frac{1}{\omega_r \sqrt{\alpha_L}} \tag{3.37}$$

40 $\alpha_L = 0.01$ $\alpha_L = 0.05$ 30 $\alpha_L = 0.1$ $\alpha_L = 0.2$ Mag. (dB) 20 10 0 90 $\Rightarrow f_r = 2.7 \text{ kHz}$ Phase (deg): 78.6 Phase (deg) Phase (deg): 64.8 60 Phase (deg): 54.9 Phase (deg): 41.8 30 0 102 $10^{\overline{3}}$ 10⁵ 104 '10 Frequency (Hz)

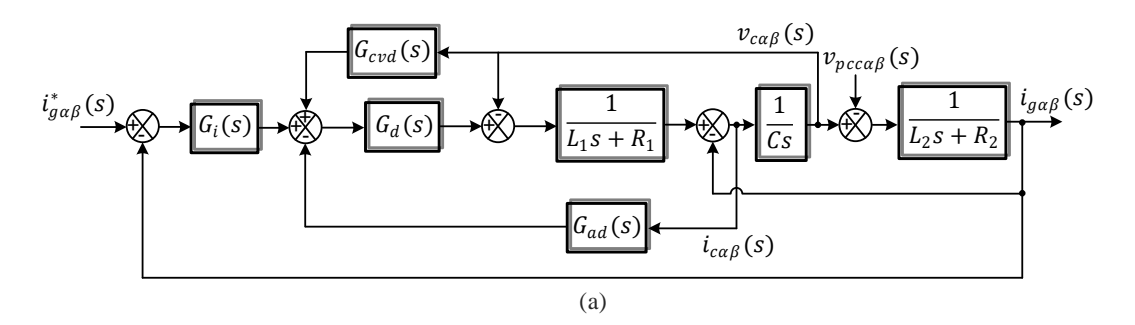
Figure 3-19 – Frequency response of $G_{ad}(s)$.

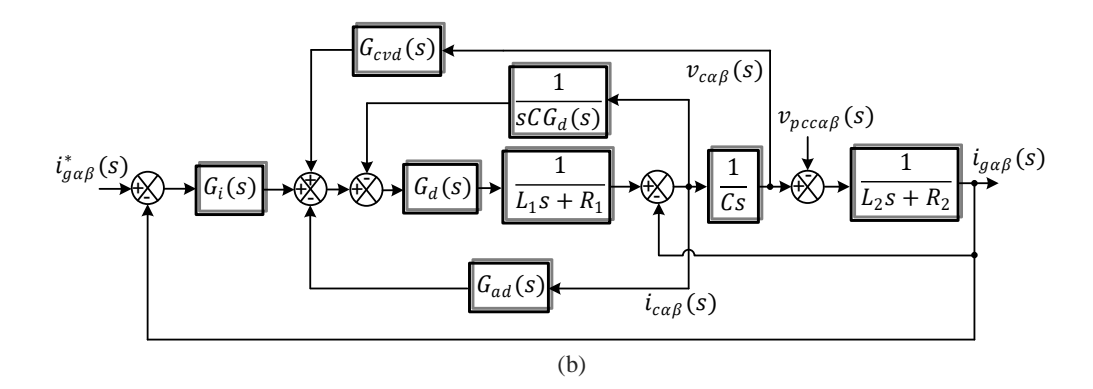
To derive the transfer function $G_{ad}(z)$, the continuous-time transfer function $G_{ad}(s)$ was discretized using the Tustin method, which was chosen to provide a more accurate approximation between the continuous and discrete time domains.

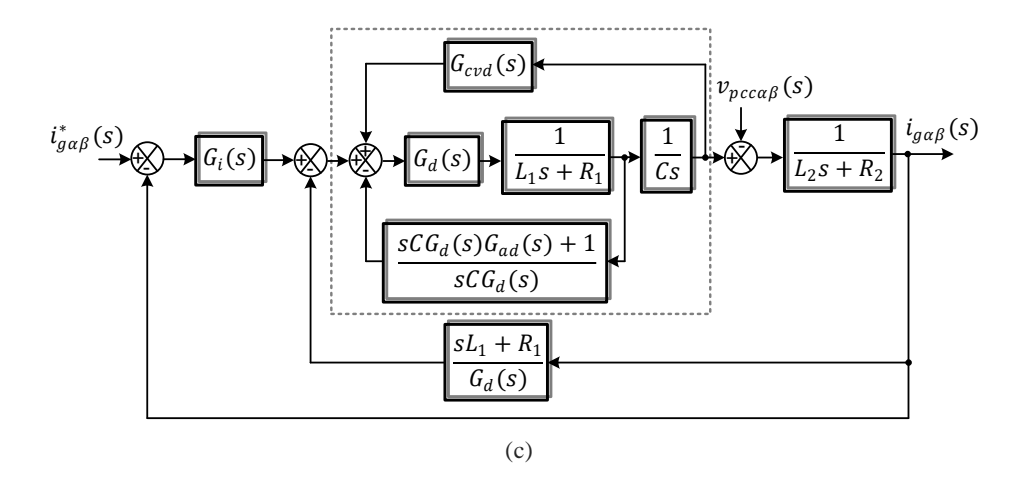
3.6.4 Capacitor Voltage Decoupling Design

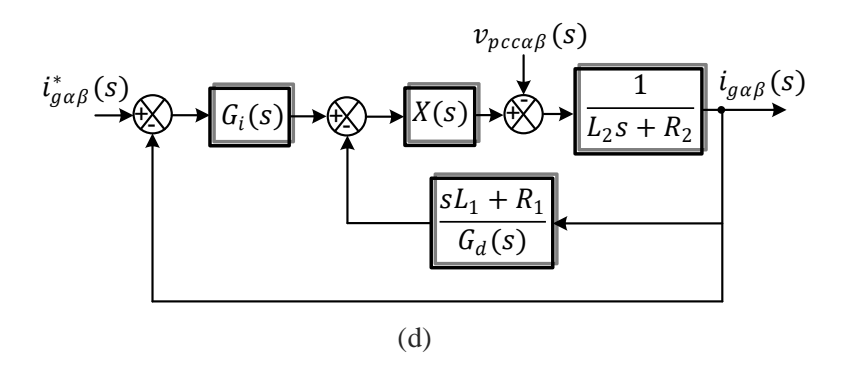
Before proceeding with the CVD design, the expression representing the output impedance of the inverter as seen by the grid, $Z_o(s)$, must be derived, since it is from this expression that the converter's disturbance rejection can be analyzed. This derivation will be carried out in the continuous-time domain, as it provides a simpler approach for obtaining an analytical expression that represents $Z_o(s)$. The function $Z_o(s)$ can be obtained through simplifications in Figure 3-20.

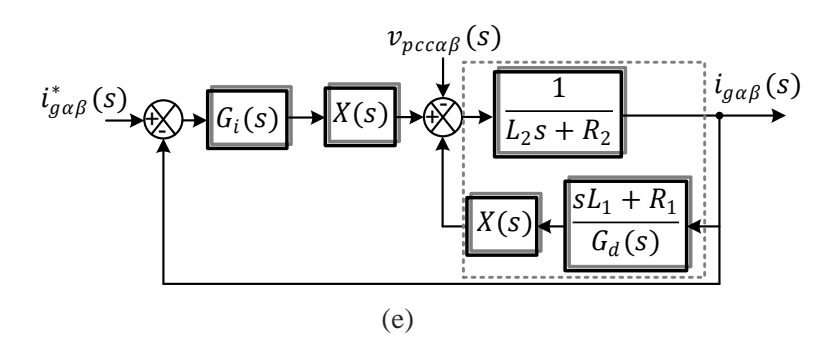
Figure 3-20 – Block diagram simplifications to derive $Z_o(s)$.

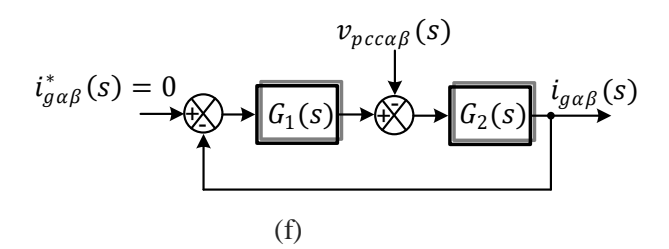












First, the block diagram shown in Figure 3-20 (a) is altered to obtain the block diagram as shown in Figure 3-20 (b). To do that, the feedback of $v_{c\alpha\beta}(s)$ is replaced with $i_{c\alpha\beta}(s)$, and its feedback node is relocated to the output of $G_i(s)$. Then, by combining the two feedback functions of $i_{c\alpha\beta}(s)$ and moving the feedback node of $i_{g\alpha\beta}(s)$ from the output $\frac{1}{L_1s+R_1}$ to the output of $G_i(s)$, Figure 3-20 (c) is obtained. The function X(s) in Figure 3-20 (d) is derived from the simplification of the blocks highlighted in Figure 3-20 (c), and is given by (3.38). Figure 3-20 (d) can be redrawn as Figure 3-20 (e) and simplifying the highlighted area results in Figure 3-20 (f).

The transfer functions $G_1(s)$ and $G_2(s)$ are given by (3.39) and (3.40), respectively. Thus, based on (3.39) and (3.40), $Z_o(s)$ is expressed by (3.41). The coefficients b_7 to b_0 and a_6 to a_1

are shown in Appendix A.

$$X(s) = \frac{G_d(s)}{s^2 L_1 C + s C [R_1 + G_{ad}(s)G_d(s)] + 1 - G_{cvd}(s)G_d(s)}$$
(3.38)

$$G_1(s) = \frac{G_i(s)G_d(s)}{L_1Cs^2 + C(R_1 + G_{ad}(s)G_d(s))s + 1 - G_{cvd}(s)G_d(s)}$$
(3.39)

$$G_2(s) = \frac{L_1 C s^2 + C[R_1 + G_{ad}(s)G_d(s)]s + 1 - G_{cvd}(s)G_d(s)}{L_1 L_2 C s^3 + C(L_2 R_1 + L_2 G_{ad}(s)G_d(s) + L_1 R_2)s^2 + \cdots}$$

$$\dots [L_1 + L_2 - L_2 G_{cvd}(s)G_d(s)]s + R_1 + R_2 - R_2 G_{cvd}(s)G_d(s)$$
(3.40)

$$Z_o(s) = \frac{b_7 s^7 + b_6 s^6 + b_5 s^5 + b_4 s^4 + b_3 s^3 + b_2 s^2 + b_1 s + b_0}{a_6 s^6 + a_5 s^5 + a_4 s^4 + a_3 s^3 + a_2 s^2 + a_1 s}$$
(3.41)

With the expression for $Z_o(s)$ of the inverter established, the following subsections evaluate scenarios without CVD and with CVD under different strategies. Additionally, the designed controller $G_i(z)$ was converted to its continuous-time equivalent $G_i(s)$ using the Tustin method for the analysis presented below.

3.6.4.1 Without Capacitor Current Feedback Active Damping and Capacitor Voltage Decoupling

In this situation, $Z_o(s)$ is analyzed without using CCFAD and CVD. Figure 3-21 (a) shows the frequency response of $Z_o(s)$, where the phase exceeds the 90° and -90° limits starting from a certain frequency. This indicates that the system may become unstable when the converter operates connected to the grid, according to passivity theory.

3.6.4.2 With Capacitor Current Feedback Active Damping as a Lead Compensator and Capacitor Voltage Decoupling as a constant function

A common strategy used in literature is to decouple v_c with a constant function. Figure 3-21 (b) shows the frequency response of $Z_o(s)$ when $G_{cvd}(s) = 0.9$ is used. Figure 3-21 (b) shows that passivity is ensured and disturbance rejection is improved compared to the previous case, as the magnitude of $Z_o(s)$ at low frequencies has increased.

3.6.4.3 With Capacitor Current Feedback Active Damping and Capacitor Voltage Decoupling as a lead compensator

An alternative to improve low-frequency disturbance rejection would be to use a lead compensation, as shown in (3.42). The coefficients τ_z and τ_p are designed to compensate for the delay $G_d(s)$ at the grid frequency f_g , which is approximately 3.2 degrees for 60 Hz. Thus, the designed parameters are $\tau_z = 1.8041 \times 10^{-4}$ and $\tau_p = 3.4354 \times 10^{-5}$. Figure 3-21 (c) shows a significant increase in disturbance rejection; however, the stability limit was exceeded, as the phase dropped below -90 degrees over a certain frequency range.

$$G_{cvd}(s) = \frac{1 + \tau_z s}{1 + \tau_p s} \tag{3.42}$$

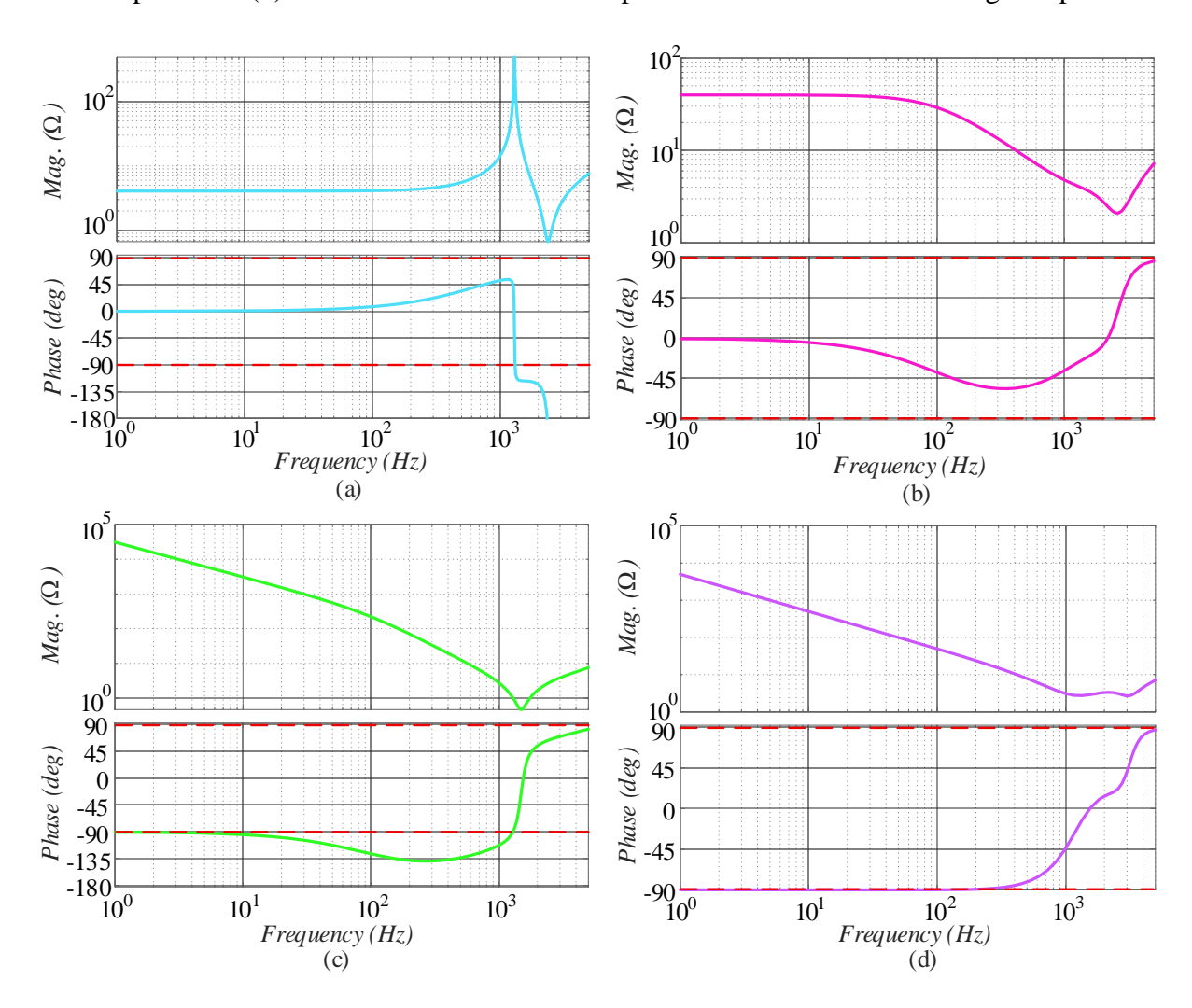
3.6.4.4 With Capacitor Current Feedback Active Damping and Capacitor Voltage Decoupling as a lead-lag compensator

One way to solve this problem is to replace the lead compensator with a lead-lag compensator, which consists of a low-pass Butterworth filter in series with the lead compensation, as shown in (3.43). The cutoff frequency, ω_c , of the filter was set to $2\pi \times 1500$, chosen as a balance between stability and improved disturbance rejection capability. This value was considered to ensure that the system effectively attenuates unwanted disturbances while preserving overall stability. Figure 3-21 (d) shows the frequency response of $Z_o(s)$ using a lead-lag compensator. The disturbance rejection decreased when compared to the previous case but remains higher than in the other cases. Additionally, the system is passive across the entire frequency range, since its phase lies between 90 and -90 degrees.

The lead-lag compensator is discretized utilizing the Tustin method to obtain the discretetime implementation for the same reason presented in the CCFAD design

$$G_{cvd}(s) = \frac{\omega_c}{s + \omega_c} \times \frac{1 + \tau_z s}{1 + \tau_n s}$$
(3.43)

Figure 3-21 – Frequency response of $Z_o(s)$ in four cases. (a) without CCFAD and CVD. (b) with CCFAD as a lead compensator and CVD as a constant function. (c) with CFFAD and CVD as a lead compensator. (d) with CCFAD as a lead compensator and CVD as a lead-lag compensator.



3.6.5 Experimental Results

To confirm the validity of the theoretical analysis and the effectiveness of the current controller, experimental validation was carried out in a lab setup, shown in Figure 3-22. More details about the lab setup are shown in Appendix B. The parameters used to obtain experimental results are listed in Table 3-4. The inverter injects current into the grid (a grid emulator, the Chroma 61830, was used to emulate it), and specifically for the current controller assessment, a PR controller is used. For obtaining these results, a PR controller was chosen because the objective was to ensure that the current had no steady-state error. Furthermore, the control strategy proposed here can also be applied to PI and PR controllers, for example. Finally, it is worth noting that the results to be presented, which evaluate the converter operating with all its control loops, use the lead compensator presented in (3.28) as the current loop controller.



Figure 3-22 – Lab setup for obtaining experimental results.

Table 3-4 – System Parameters.

Parameter	Description	Value
P_n	Nominal power	11 kVA
V_{dc}	DC-link voltage	650 V
L_1	Inverter-side inductor	1 mH
C	LCL filter capacitor	15 μF
L_2	Grid-side inductor	300 μΗ
R_1, R_2	ESR of L_1 and L_2	$0.1~\Omega$
v_g	Grid line voltage (RMS)	380 V
f_g	Grid frequency	60 Hz
T_s/f_s	Sampling period/frequency	100 μs/10 kHz
f_{sw}	Switching frequency	10 kHz

The resonant gain was set to 1000, and a PLL was used to synchronize the inverter to the grid. Four scenarios were tested, as listed below:

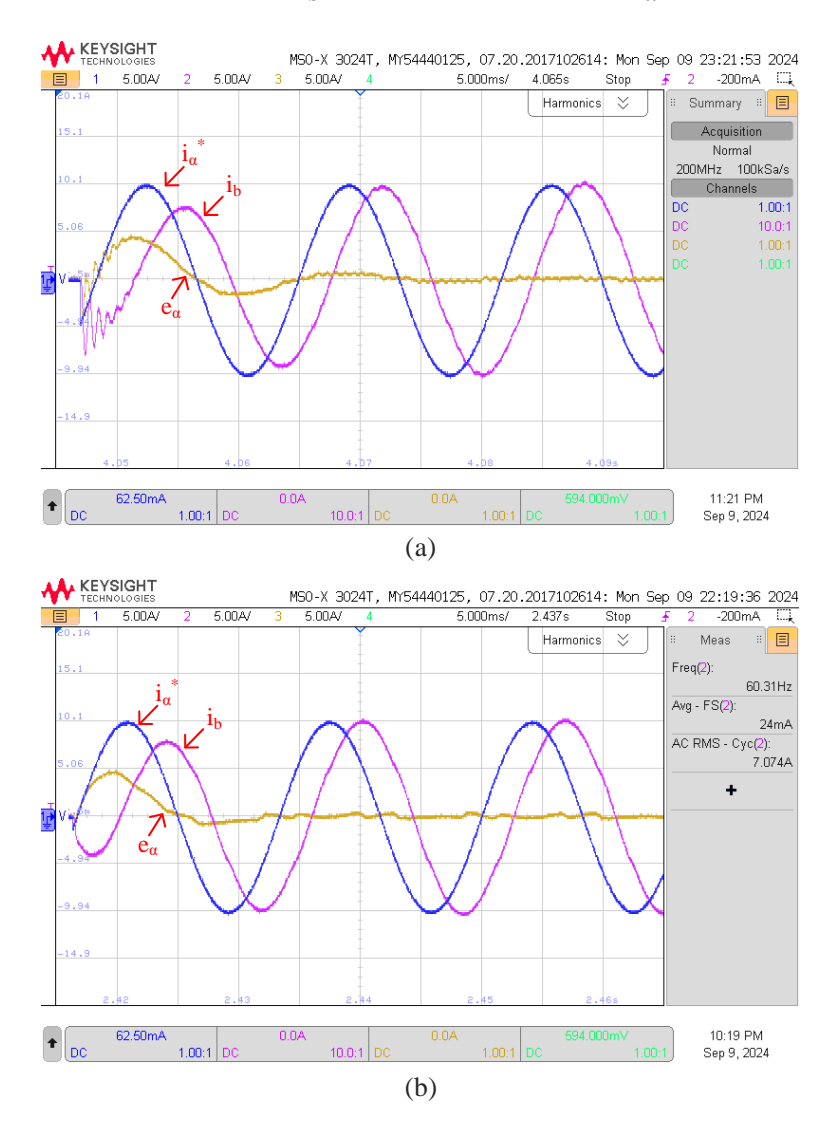
- Dynamic response of the current controller.
- Line impedance variation.
- Inverter operation with the presence of voltage harmonics.
- Inverter operation under voltage sag.

3.6.5.1 Current controller dynamic response assessment

To assess the dynamic response of the current controller, the response to a 10 A peak step was compared in two scenarios. The first scenario corresponds to the current controller tuned for a bandwidth of 2 kHz but without the use of lead compensation. In this case, the gain was $R_a = 9.17$. The second scenario evaluated the proposed strategy, i.e., with lead compensation applied to the proportional part of the current controller. Figure 3-23 (a) shows the result without the proposed strategy. The current reference in alpha-axis, i_{α}^* , obtained internally from the DSP, is

represented by the blue curve; the actual current of the phase 'b' by the lilac curve; and the error in the alpha-axis, e_{α} , also obtained internally from the Digital Signal Processing (DSP), by the yellow curve. Figure 3-23 (b) shows the result with the proposed strategy, where the current reference is also represented by the blue curve, the actual current by the lilac curve, and the error by the yellow curve.

Figure 3-23 – Step response of the current controller. (a) without lead compensation. (b) with lead compensation. Blue curve – current reference in α -axis (i_{α}^*) , lilac curve – injected current of phase 'b' (i_b) , yellow curve – error (e_{α}) .



Source: Author.

By analyzing the figures, it can be observed that the use of lead compensation improved the dynamic response of the inverter. When the lead compensation was not used, the current exhibited higher oscillations during the transient period. Additionally, the settling time without lead compensation was around 25 ms, whereas it decreased to approximately 15 ms when it was applied.

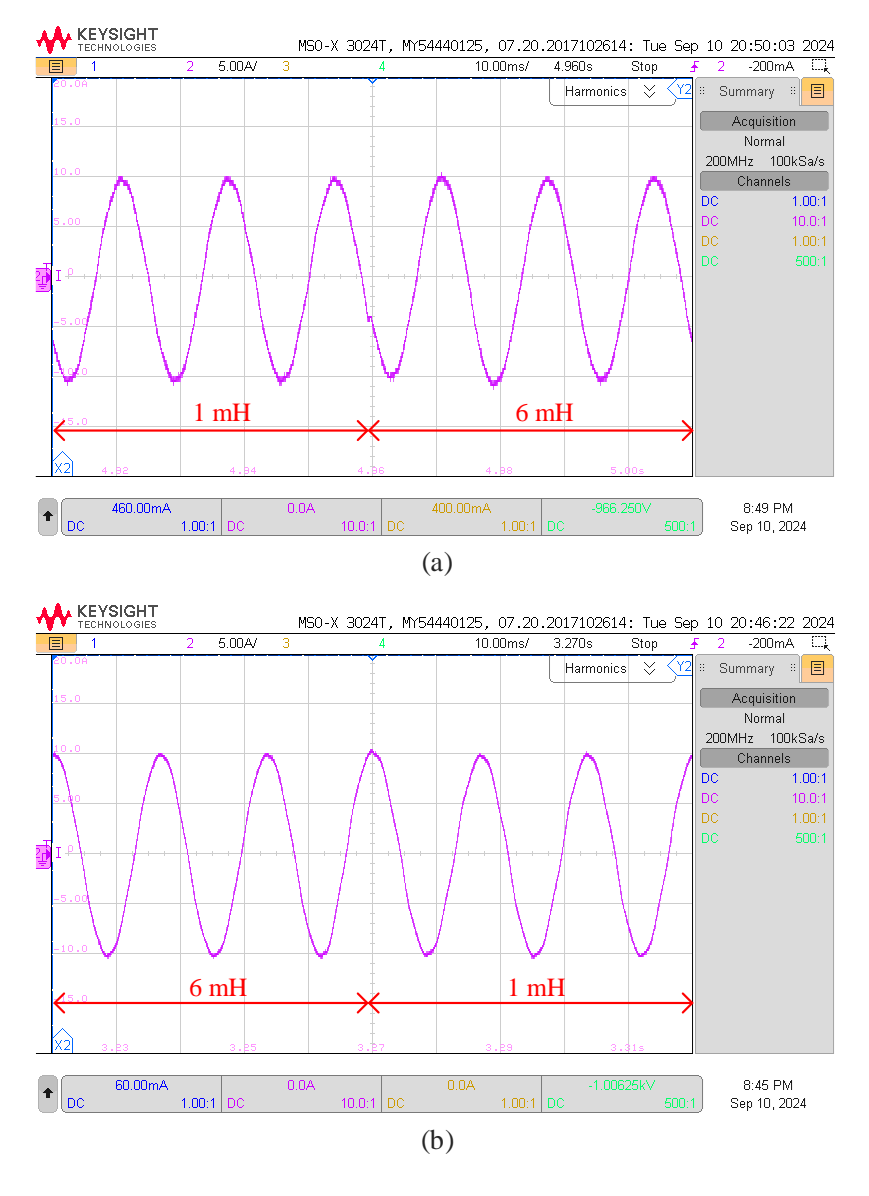
3.6.5.2 Line impedance variation assessment

This section assesses the performance of the CCFAD control strategy under varying line impedance conditions. The current reference was also fixed at a peak of 10 A, and two scenarios were considered to evaluate the system's behavior. In the first scenario, the line inductance was initially set to 1 mH and then increased to 6 mH, as shown in Figure 3-24 (a). In the second scenario, the line inductance started at 6 mH and was reduced to 1 mH, depicted in Figure 3-24 (b).

These inductance values were chosen because, depending on the value of L_g , f_r changes and becomes either greater than $f_s/6$ or smaller than $f_s/6$, which is the critical frequency, and, according to Figure 3-10, defines the stable or unstable operating region of the converter.

From the analysis, it was observed that regardless of the variation in L_g , the inverter operation remained stable, demonstrating that passivity was ensured through a simple and effective strategy.

Figure 3-24 – Injected current of phase 'b'. (a) L_g changes from 1 mH to 6 mH. (b) L_g changes from 6 mH to 1 mH.



3.6.5.3 Disturbance rejection assessment – grid voltage harmonics

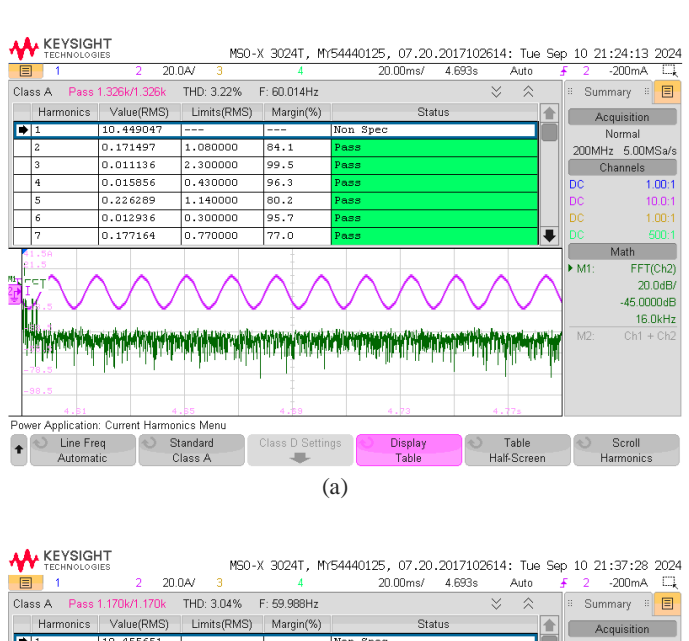
As mentioned earlier, the function of G_{cvd} is to increase the disturbance rejection capability of the inverter. Therefore, this section aims to evaluate the disturbance rejection capability of the inverter in the presence of voltage harmonics in the grid. To achieve this, a grid emulator was used to simulate the electrical grid, which was distorted with the presence of the 5th and 7th harmonics, where the magnitude of each harmonic was set to 2 %.

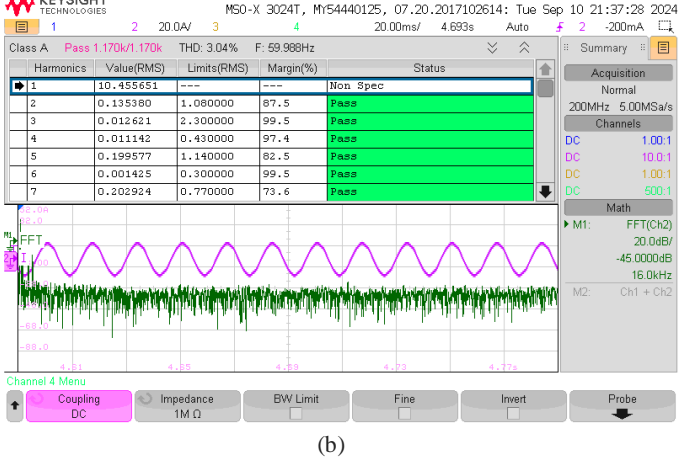
Three strategies were compared in this evaluation:

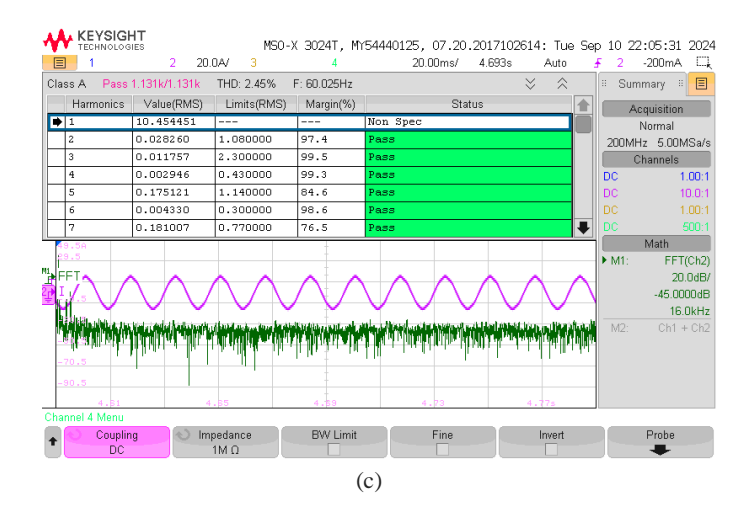
- 1) Without the presence of G_{cvd} .
- 2) G_{cvd} as a constant with a value of 0.9.
- 3) The proposed approach, where G_{cvd} is the designed lead-lag compensation.

In Figure 3-25 (a) - (c), the Total Harmonic Distortion (THD) of the injected currents into the grid are shown under three different strategies. The current reference value was set to 10 A RMS. Figure 3-25 (a) shows the case without G_{cvd} , Figure 3-25 (b) shows the case where G_{cvd} is a constant function with a value of 0.9, and Figure 3-25 (c) shows the case where G_{cvd} is a lead-lag compensation. For the first case, the THD was 3.22 %, for the second case it was 3.04 %, and for the third case it was 2.45 %. These THD values can be seen at the top of each image. Therefore, the proposed strategy demonstrated superior disturbance rejection capability in the presence of harmonics in the grid, confirming the theoretical development presented in the previous section.

Figure 3-25 – THD of the injected current in the presence of voltage harmonics. (a) without G_{cvd} . (b) with G_{cvd} as a constant value. (c) with G_{cvd} as a lead-lag compensator.







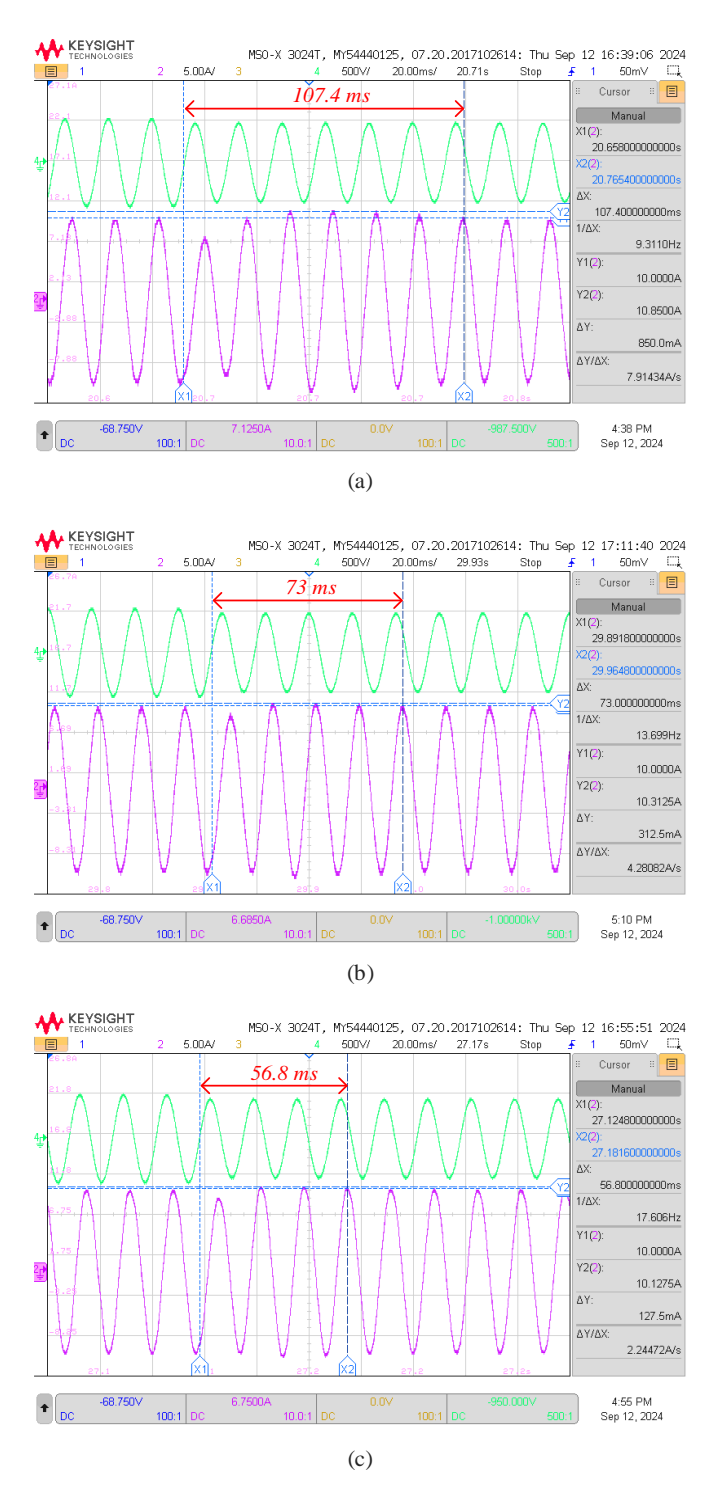
3.6.5.4 Disturbance rejection assessment – grid voltage sag

In this test, the response of the inverter was evaluated under a grid voltage sag. In this situation, the inverter was operating normally, injecting a 10 A peak, when suddenly a 10 % reduction in the nominal line voltage of 380 V was induced (green curve). In Figure 3-26 (a) - (c), the injected currents (lilac curves) into the grid are shown under three different strategies. Figure 3-26 (a) shows the case without G_{cvd} , Figure 3-26 (b) shows the case where G_{cvd} is a constant function with a value of 0.9, and Figure 3-26 (c) shows the case where G_{cvd} is a lead-lag compensation.

Examining the figures, the addition of the decoupling function G_{cvd} improved the system's dynamic response, with significant reductions in both overshoot and settling time. Without G_{cvd} , the overshoot was measured at 850 mA, but with G_{cvd} as a constant function, this overshoot decreased to 312.5 mA. Similarly, the settling time was also improved. Without G_{cvd} , the settling time was recorded at 107.4 ms. With the decoupling function applied, the settling time was reduced to 73 ms. However, among the three strategies, the one that achieved the best performance was the proposed strategy, with the lead-lag compensation. Using this strategy, the overshoot decreased to 127.5 mA, and the settling time was reduced to 56.8 ms, indicating a much faster recovery after the voltage sag.

This considerable decrease in overshoot suggests that the inverter was better able to manage the voltage sag and prevent excessive current fluctuations. Additionally, this reduced settling time implies that the system can respond more quickly to voltage disturbances, enhancing its overall dynamic performance.

Figure 3-26 – Injected current of phase 'b' during a voltage sag. (a) without G_{cvd} . (b) with G_{cvd} as a constant value. (c) with G_{cvd} as a lead-lag compensator. Green curve – line voltage, lilac curve – injected current of phase 'b'.



3.7 Voltage Control Loop Design

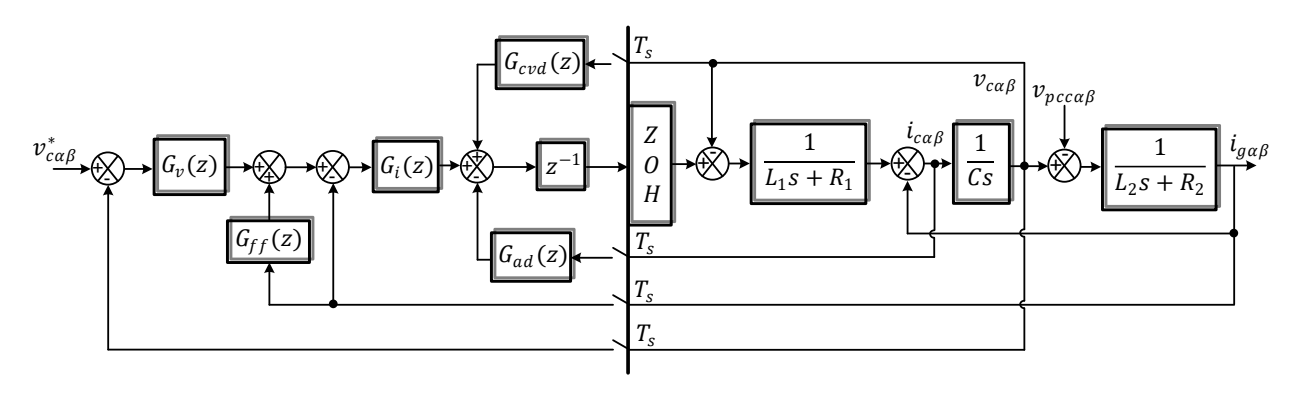
This section presents the modeling of the voltage controller, along with the concept of Disturbance Input Decoupling (DID), to improve its dynamic performance.

3.7.1 Voltage Controller Design

The voltage controller aims to control the voltage $v_{c\alpha\beta}$. A PR controller is used for this purpose, and its transfer function is given by (3.44). K_{pv} , K_{rv} and ω_o are the proportional gain, resonant gain and grid nominal frequency in rad/s, respectively. The control block diagram is shown in Figure 3-27.

$$G_v(z) = K_{pv} + K_{rv}T_s \frac{1 - z^{-1}\cos(\omega_o T_s)}{1 - 2z^{-1}\cos(\omega_o T_s) + z^{-2}}$$
(3.44)

Figure 3-27 – Control block diagram of the voltage loop.



Source: Author.

The bandwidth of the voltage controller was set to 200 Hz. The gain K_{pv} was determined using the root locus method for the open-loop transfer function, which corresponds to the product of the transfer function representing the current control loop (approximated by a first-order equivalent) and the plant transfer function given in equation (3.45). For this, it was assumed that G_{cvd} perfectly decouples the feedback of the capacitor voltage, and that G_{ff} , which will be detailed in the following subsection, perfectly decouples the feedback of the injected current. The closed-loop poles for the chosen bandwidth are shown in Figure 3-28 as red "X" markers.

$$\frac{v_{c\alpha\beta}(s)}{i_{c\alpha\beta}(s)} = \frac{1}{Cs} \tag{3.45}$$

0.5π /T _{0.4π /T} 0.6 /T 0.8 0.2 d.зт /т 0.7π/T 0.6 0.8⊤/T 0.2τ / Imag. Axis (sec.⁻¹) 0.9⊤/T 0. 1π /T 0.2 $1\pi/T$ -0.2 0.9⊤/T 0.1 / -0.4 0.8π/T 0.2π/ -0.6 0.7π/T 0.3⊤/T -0.8 -1 -0.8 -0.6 -1 Real Axis (sec.-1)

Figure 3-28 – Root locus for the voltage control loop.

The gain K_{rv} was chosen according to the guideline outlined in (3.46) [97]. The gain values are shown in Table 3-5.

$$K_{rv} \ge 2K_{pv}\omega_o \tag{3.46}$$

Table 3-5 – Voltage Controller Gains.

Parameter	Value
K_{pv}	0.02
K_{rv}	40

Source: Author.

3.7.2 Disturbance Input Decoupling

To improve the dynamic performance of the voltage controller, a DID approach is employed, as described in [99], [100]. Figure 3-29 presents the block diagram illustrating the DID implementation. Upon examination, it becomes clear that $i_{g\alpha\beta}$ acts as a disturbance to the voltage control loop.

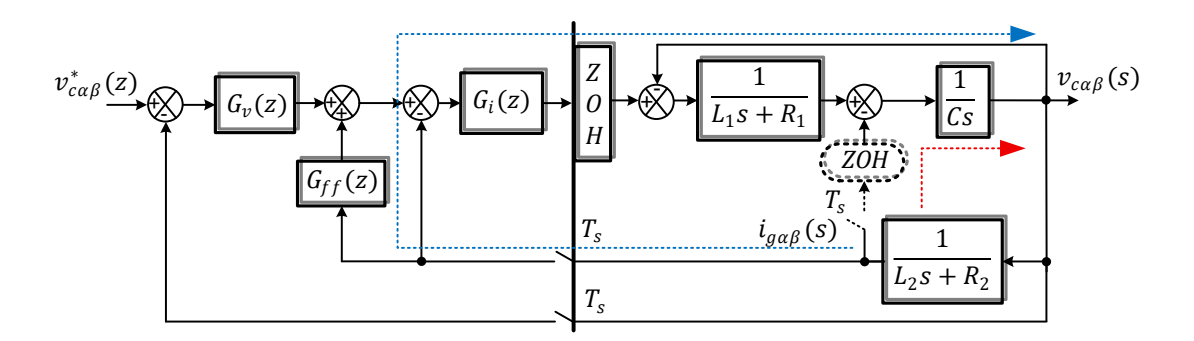
The design principle for the transfer function $G_{ff}(z)$ is to eliminate the effect of $i_{g\alpha\beta}$ in the output at the sampling instants. This method is applicable only when the disturbance dynamics are slower than the sampling period T_s . To satisfy this condition, it is assumed that $i_{g\alpha\beta}$ is modeled using a ZOH block. The expression for determining the transfer function $G_{ff}(z)$ is given in (3.47). Deriving (3.47) requires evaluating the paths (red and blue arrows in Figure 3-29) that include both the disturbance and the DID transfer function.

$$-i_{g\alpha\beta}(z)\mathcal{Z}\left[ZOH\frac{1}{Cs}\right] + i_{g\alpha\beta}(z)G_{ff}(z)\mathcal{Z}\left[ZOHG_{CLi}(s)\frac{1}{Cs}\right] = 0 \tag{3.47}$$

The function $G_{CLi}(s)$ represents the current loop. To simplify the design of the DID function, it can be approximated by an equivalent first-order system that matches the actual system's bandwidth, where $\omega_i = 2\pi \times 2000$ rad/s. As a result, (3.47) can be rewritten as (3.48).

$$G_{ff}(z) = \frac{Z\left[ZOH\frac{1}{Cs}\right]}{Z\left[ZOH\frac{\omega_i}{s+\omega_i}\frac{1}{Cs}\right]} = K_{ff}\frac{z-\delta_z}{z-\delta_p}$$
(3.48)

Figure 3-29 – Closed-loop diagram to assess the effect of $G_{ff}(z)$.



Source: Author.

The parameters δ_z , δ_p and K_{ff} are defined in (3.49) - (3.51), respectively. The calculated values are shown in Table 3-6.

$$\delta_z = e^{-T_S \omega_i} \tag{3.49}$$

$$\delta_p = \frac{\delta_z (T_s \omega_i + 1) - 1}{T_s \omega_i + \delta_z - 1} \tag{3.50}$$

$$K_{ff} = \frac{T_s \omega_i}{T_s \omega_i + \delta_z - 1} \tag{3.51}$$

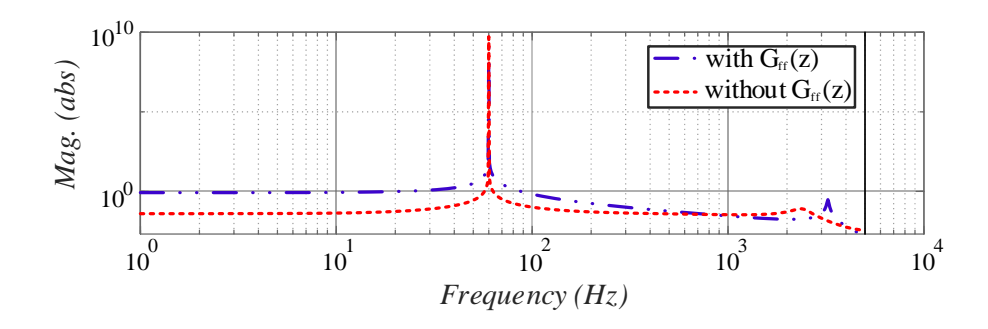
Table 3-6 – DID Control Gains.

Parameter	Value
δ_z	0.2846
δ_p	-0.6609
K_{ff}	2.3217

To assess the impact of incorporating DID, the loop gain of the voltage control system, as depicted in Figure 3-27, is analyzed. Figure 3-30 compares the Bode magnitude plot of the loop gain with and without the proposed DID, with the PR controller tuned for a bandwidth of 200 Hz. As observed, the use of DID improves the loop gain at low frequencies, leading to better system performance in the presence of disturbances.

Before presenting the advantages brought by the proposed DID in the following subsections, the implementation of the virtual impedance and the P_e and Q_e control loops are first described.

Figure 3-30 – Bode magnitude plot of the loop gain with and without $G_{ff}(z)$.



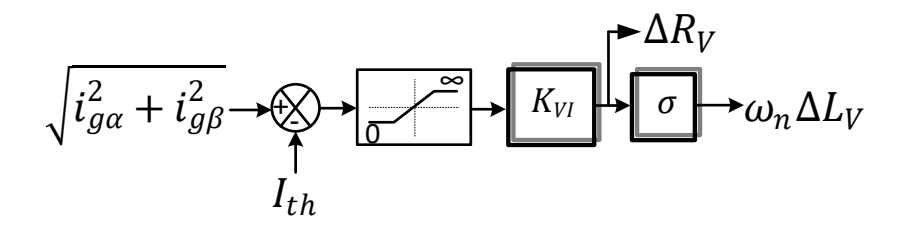
Source: Author.

3.8 Virtual Impedance Loop

The concept of the virtual impedance loop is based on modifying the output impedance characteristics of the inverter. This modification is accomplished by adjusting the voltage reference signals $v_{c\alpha}^*$ and $v_{c\beta}^*$, which are supplied to the inner voltage control loop.

The main goal of virtual impedance is to increase the total output impedance of the inverter during transients (e.g., voltage sags) or fault conditions, thereby limiting the output current. The virtual impedance is composed of a fixed value of virtual resistance R_{Vi} and virtual inductance L_{Vi} (used during the normal operation of the converter), along with an adaptive current-limiting virtual impedance, ΔR_V and ΔL_V [101]. Using Figure 3-15 as a reference, during normal operation, R_V takes the value of R_{Vi} and R_V takes the value of R_V and R_V

Figure 3-31 – Virtual impedance implementation.



Source: Author.

$$\Delta R_V = K_{VI} \left(\sqrt{i_{g\alpha}^2 + i_{g\beta}^2} - I_{th} \right) \tag{3.52}$$

$$\Delta L_V = (\sigma \times \Delta R_V)/\omega_n \tag{3.53}$$

The parameter K_{VI} is a constant that satisfies (3.54), I_{th} is the current-limiting threshold, and σ is a user-defined X/R ratio for the virtual impedance [102]. The maximum expected magnitude difference between the v_{inv} and v_{pcc} , as well as the maximum allowed phase current magnitude, are designated as V_{max} and I_M , respectively.

$$K_{VI}\sqrt{\sigma^2 + 1}(I_M - I_{th}) \ge \frac{V_{max}}{I_M}$$
 (3.54)

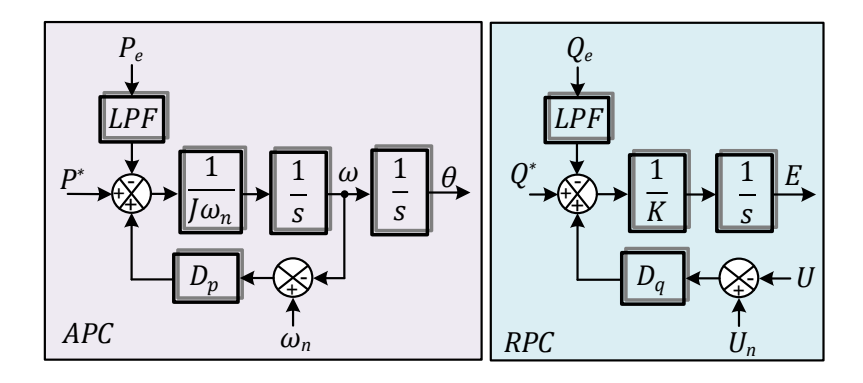
According to [30] and [103], it is recommended that the value of R_{Vi} be around 0.2 pu and X_{Vi} around 0.3 pu, respectively. The value of R_{Vi} was chosen to be 2 Ω , which is equivalent to

0.15 pu, and the value of L_{Vi} was chosen to be 7 mH, which corresponds to an X_{Vi} of 0.2 pu.

3.9 Active and Reactive Power Controllers

As shown in Figure 3-32, the VSM system can be represented by (3.55) [104].

Figure 3-32 – APC and RPC loops.



Source: Author.

$$\begin{cases} P^* - P_e + D_p(\omega_n - \omega) = J\omega_n \frac{d\omega}{dt} \\ Q^* - Q_e + D_q(U_n - U) = K \frac{dE}{dt} \\ \delta = \int (\omega - \omega_n) dt = \Delta\omega \end{cases}$$
 (3.55)

To tune the parameter J, it is necessary to derive the small-signal model of the APC. To do so, it is assumed that a state variable, such as P_e , is equal to its steady-state value P_o plus a small ac variation, ΔP , i.e., $P_e = P_o + \Delta P$.

Substituting $P_e = P_o + \Delta P$ in (3.55), yields to (3.56).

$$P^* - (P_o + \Delta P) + D_p(\omega_n - \omega) = J\omega_n \frac{d\omega}{dt}$$
(3.56)

Considering the steady-state condition, at the operating point $(P_e = P_o, \omega = \omega_n, \frac{d\omega}{dt} = 0)$, (3.56) can be rewritten as (3.57):

$$P^* - P_o + D_p(\omega_n - \omega_n) = 0 \Rightarrow P^* = P_o$$
 (3.57)

The linearized equation is given by (3.58):

$$P^* - P_o - \Delta P - D_p \Delta \omega = J \omega_n \Delta \omega s \Rightarrow \frac{\Delta \omega}{\Delta P} = -\frac{1}{J \omega_n s + D_p}$$
 (3.58)

 D_p is calculated using (3.59), where a 100 % change in active power corresponds to a 2 % change in grid frequency at steady-state.

$$D_p = \frac{\Delta P_{max}}{\Delta \omega_{max}} = \frac{10000}{(2\pi 60) \times 2\%} = 1327$$
 (3.59)

Based on this, (3.60) is used to calculate J so that the bandwidth of the APC (f_{bwP}) is 20 Hz, which is one-tenth of the voltage controller's bandwidth.

$$J = \frac{D_p}{2\pi f_{bwP}\omega_n} = \frac{1327}{2\pi \times 20 \times 377} = 0.028 \tag{3.60}$$

To tune the parameter K, it is necessary to derive the small-signal model of the RPC. Using the same methodology for the APC, substitute $Q_e = Q_o + \Delta Q$ in (3.55), yields to (3.61)

$$Q^* - (Q_o + \Delta Q) + D_q(U_n - U) = K \frac{dE}{dt}$$
 (3.61)

Considering the steady-state condition, at the operating point $(Q_e = Q_o, U = U_n, \frac{dE}{dt} = 0)$, (3.61) can be rewritten as (3.62):

$$Q^* - Q_o + D_q(U_n - U_n) = 0 \Rightarrow Q^* = Q_o$$
 (3.62)

Assuming that $\Delta U = \Delta E$, which is valid if $E_n \approx U_n$, the linearized equation is given by (3.63):

$$-\Delta Q - D_q \Delta U = K \Delta E s$$

$$-\Delta Q = \Delta E (D_q + K s)$$

$$\frac{\Delta E}{\Delta Q} = -\frac{1}{K s + D_q}$$
(3.63)

 D_q is calculated using (3.64), where a 100 % change in reactive power corresponds to a 10 % change in grid nominal voltage at steady-state.

$$D_q = \frac{\Delta Q_{max}}{\Delta V_{max}} = \frac{10000}{220\sqrt{2} \times 10\%} = 321$$
 (3.64)

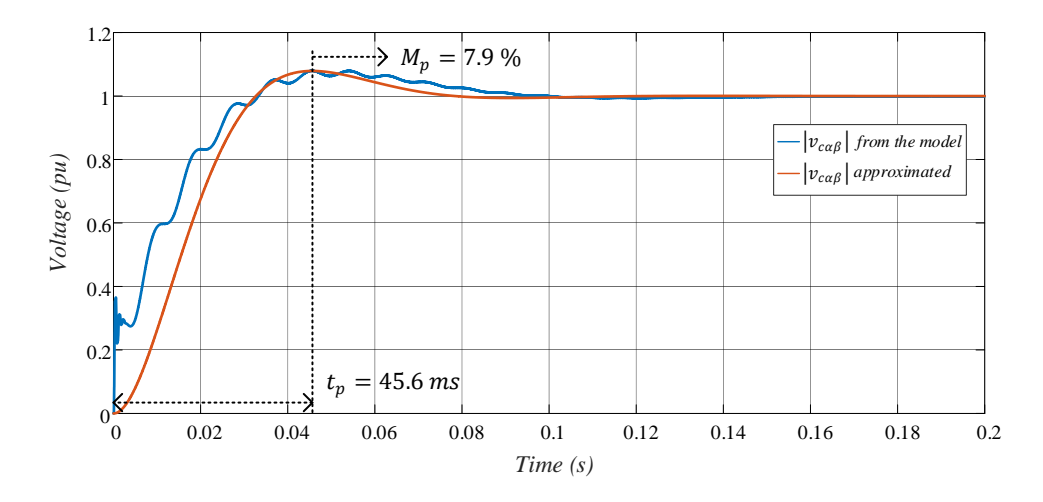
Based on this, (3.65) is used to calculate K so that the bandwidth of the RPC (f_{bwQ}) is 20 Hz.

$$K = \frac{D_q}{2\pi f_{bwQ}} = \frac{321}{2\pi \times 20} = 2.557 \tag{3.65}$$

3.10 Voltage Controller Influence on the Power Control Loops

This section aims to analyses the influence of the voltage control loop on the power control loops. This is necessary to demonstrate, in the next section, the impact of using DID on the experimental results that will be presented shortly. To achieve this, it is first necessary to derive an expression that represents the voltage control loop. Figure 3-33 shows the step response of the voltage control loop (without the use of DID). The resulting dynamics can be approximated by a second-order system using the overshoot M_p and the peak time t_p [76]. Equation (3.66) shows the second-order function used to approximate the voltage control loop along with its corresponding values.

Figure 3-33 – Voltage step responses (blue) and equivalent second-order function (orange).



Source: Author.

$$C_V(s) = \frac{\omega_n^2}{s^2 + 2\zeta\omega_n s + \omega_n^2} = \frac{7832.2}{s^2 + 111.2s + 7832.2}$$
(3.66)

For the modelling of the power control loops, a methodology similar to that used in [76] is adopted. However, the authors employed droop control, whereas the following derivation will consider control based on a VSM. First, let us assume that the inverter voltage is represented by

the phasor $V_i \angle \delta$, and it is connected to the grid, which has a voltage represented by the phasor $V_g \angle 0^\circ$, through an inductance with reactance X_g .

The expressions that represent the exchange of P and Q between the two sources are given by (3.67) [105]:

$$P = \frac{3V_i V_g}{X_g} \sin(\delta)$$

$$Q = \frac{3}{X_g} \left[V_i^2 - V_i V_g \cos(\delta) \right]$$
(3.67)

Linearizing *P* and *Q* at the operating point (V_o, δ_o) yields:

$$V_i = V_o + \Delta V, \, \delta = \delta_o + \Delta \delta, \, \Delta \omega = \frac{d\Delta \delta}{dt}$$

By expanding in a Taylor series, equation (3.68) is obtained:

$$\Delta P = \frac{\partial P}{\partial V_i} \Big|_{o} \Delta V + \frac{\partial P}{\partial \delta} \Big|_{o} \Delta \delta$$

$$\Delta Q = \frac{\partial Q}{\partial V_i} \Big|_{o} \Delta V + \frac{\partial Q}{\partial \delta} \Big|_{o} \Delta \delta$$
(3.68)

By taking the partial derivatives of P and Q with respect to V_i and δ , evaluated at the operating point ($V_i = V_o$, $\delta = \delta_o$), the following expressions are obtained (3.69):

$$K_{PV_{i}} = \frac{\partial P}{\partial V_{i}} \Big|_{o} = \frac{3V_{g}}{X_{g}} \sin(\delta_{o})$$

$$K_{P\delta} = \frac{\partial P}{\partial \delta} \Big|_{o} = \frac{3V_{o}V_{g}}{X_{g}} \cos(\delta_{o})$$

$$K_{QV_{i}} = \frac{\partial Q}{\partial V_{i}} \Big|_{o} = \frac{3}{X_{g}} \left[2V_{o} - V_{g} \cos(\delta_{o}) \right]$$

$$K_{Q\delta} = \frac{\partial Q}{\partial \delta} \Big|_{o} = \frac{3V_{o}V_{g}}{X_{g}} \sin(\delta_{o})$$
(3.69)

The linearized equations are then given by (3.70):

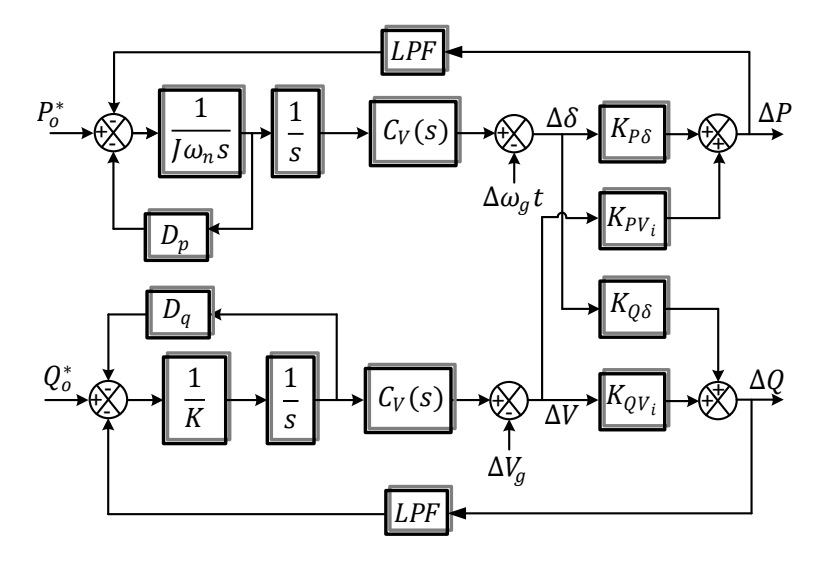
$$\Delta P = K_{PV_i} \Delta V + K_{P\delta} \Delta \delta$$

$$\Delta Q = K_{OV_i} \Delta V + K_{O\delta} \Delta \delta$$
(3.70)

Figure 3-34 shows the linearized system of equations representing the small-signal

dynamics of the active and reactive power control loops, along with the control used for the VSM and the function $C_V(s)$, which represents the voltage control loop.

Figure 3-34 – Small-signal model of the power control loops with VSM control.



Source: Author.

Figure 3-35 shows the step responses of the active power with $C_V(s) = 1$, without the voltage control loop, and with $C_V(s)$ as given by equation (3.66). It can be observed that the response is oscillatory when the voltage loop is considered, and exponential when it is not. Therefore, there is an interaction between the control loops, and for this reason, the voltage control loop using DID was proposed. The following section presents experimental results with and without the use of DID.

 $-C_{V}(s) = 1$ $-C_{V}(s) = 2nd \ order \ transfer \ function$ 0.5 0.1 0.2 0.3 0.4 0.5 0.6 0.7 0.7

Figure 3-35 – Step responses of the active power.

3.11 Experimental Results

To evaluate the influence of using DID, experimental results were carried out. The system parameters used were the same as those presented in Table 3-4. The tests were divided into two scenarios: the first evaluates the inverter operating in islanded mode, and the second evaluates the inverter operating in grid-connected mode. It is worth noting that for both conditions, the current loop controller used was a lead compensator, as shown in Subsection 3.6.2. Additionally, it is assumed that the voltage V_{dc} is regulated directly by a DC source with a constant value. The system and control parameters are shown in Table 3-7.

3.11.1 Grid-Forming Inverter Assessment – Isolated Operation

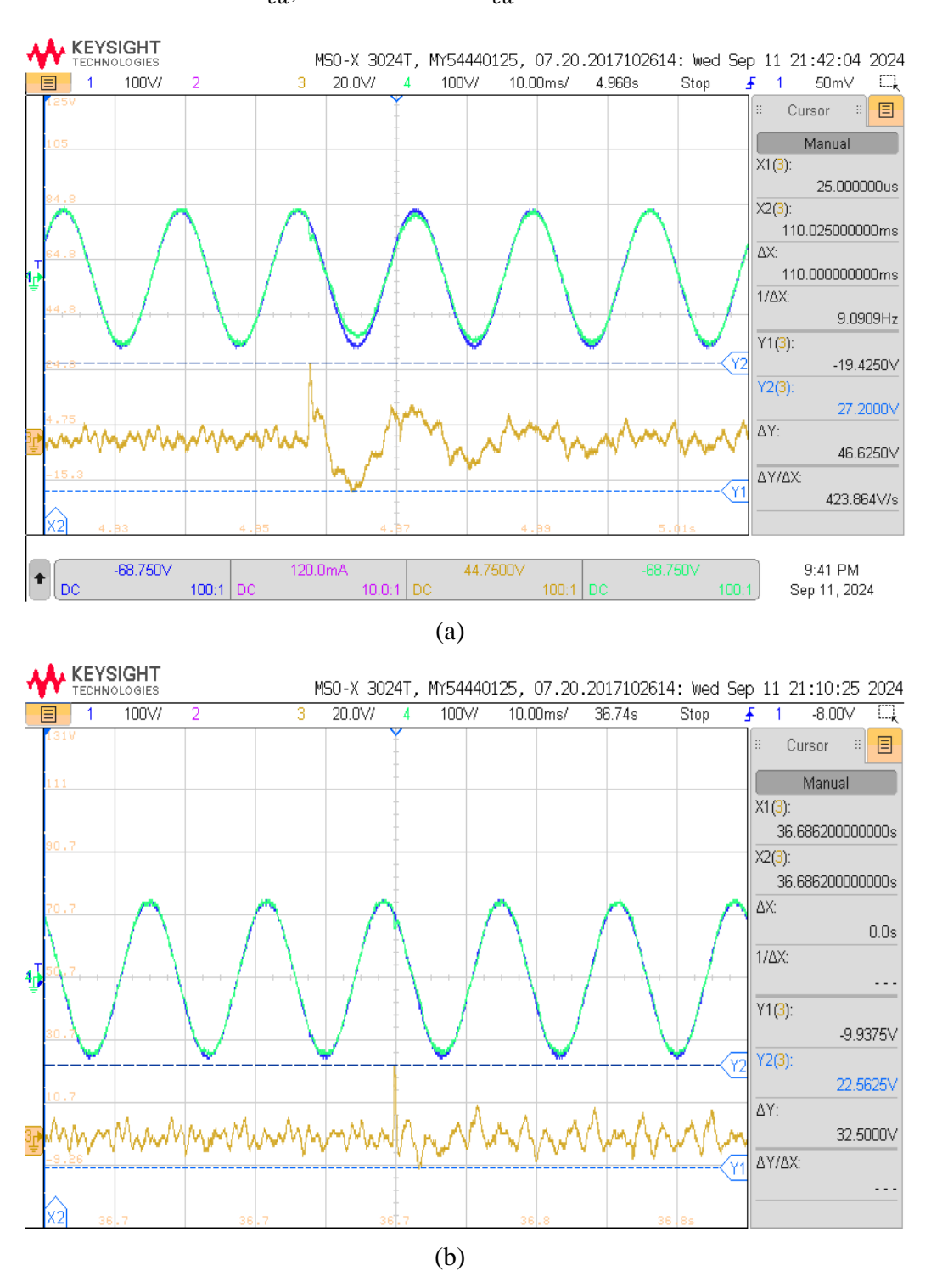
In this scenario, the voltage reference $v_{c\alpha\beta}^*$ is directly imposed without any input from the power control loops. The inverter supplies a three-phase linear load of 17 Ω . At a certain point, an identical load is added to the system. Figure 3-36 (a) - (b) show the α -axis voltage reference (blue curve), with a nominal peak value of 120 V, the voltage across the capacitor in the α -axis (green curve), and the corresponding error signal (yellow curve), without and with DID, respectively.

Table 3-7 – System and Control Parameters.

Parameter	Value	Description
Control parameters of the VSM		
R_a	$5.6~\Omega$	Current controller proportional gain
k_l	0.27	Current controller lead gain
K_{pv}	$0.04~\Omega$	Voltage controller proportional gain
K_{rv}	40 A/V	Voltage controller resonant gain
R_{Vi}	2 Ω	Virtual resistance
L_{Vi}	7 mH	Virtual inductance
K_{VI}	0.51 Ω/A	Constant current-limiting threshold
σ	0.75	X/R ratio
ω_n	$2\pi60 \ rad/s$	Rated angular frequency

J	$0.028Kg\cdot m^2$	Moment of inertia
D_p	1327 $W \cdot s/rad$	Damping coefficient of active power- frequency
D_q	321 Var/V	Droop coefficient of reactive power voltage
K	2.557 <i>A</i> · <i>s</i>	Regulator coefficient of reactive power
U_n	$220\sqrt{2}V$	Effective value of the rated voltage amplitude
Grid parameters		
V_g	380 V	Grid voltage (L-L, RMS)
f_g	60 Hz	Grid frequency

Figure 3-36 – Capacitor voltage during a load variation: (a) without DID; (b) with DID. Blue curves – $v_{c\alpha}^*$; Green curves – $v_{c\alpha}$: Yellow curves – error.



By examining these figures, the introduction of DID leads to a noticeable improvement in the GFM's inverter performance when responding to load changes. For the case without DID, the voltage variation observed was 46.6 V. In contrast, when DID is applied, the voltage variation decreases to 32.5 V, indicating that the GFM inverter has better disturbance rejection capability.

Additionally, without DID, the settling time was approximately 35 ms. With DID, the settling time was reduced to approximately 10 ms, reflecting a much faster recovery to the nominal operating conditions. This reduction in settling time demonstrates the ability of DID to enhance the GFM's inverter dynamic response, ensuring that the system can react more swiftly to changes in load and return to a stable state more efficiently.

3.11.2 Grid-Forming Inverter Assessment – Grid-Connected Operation

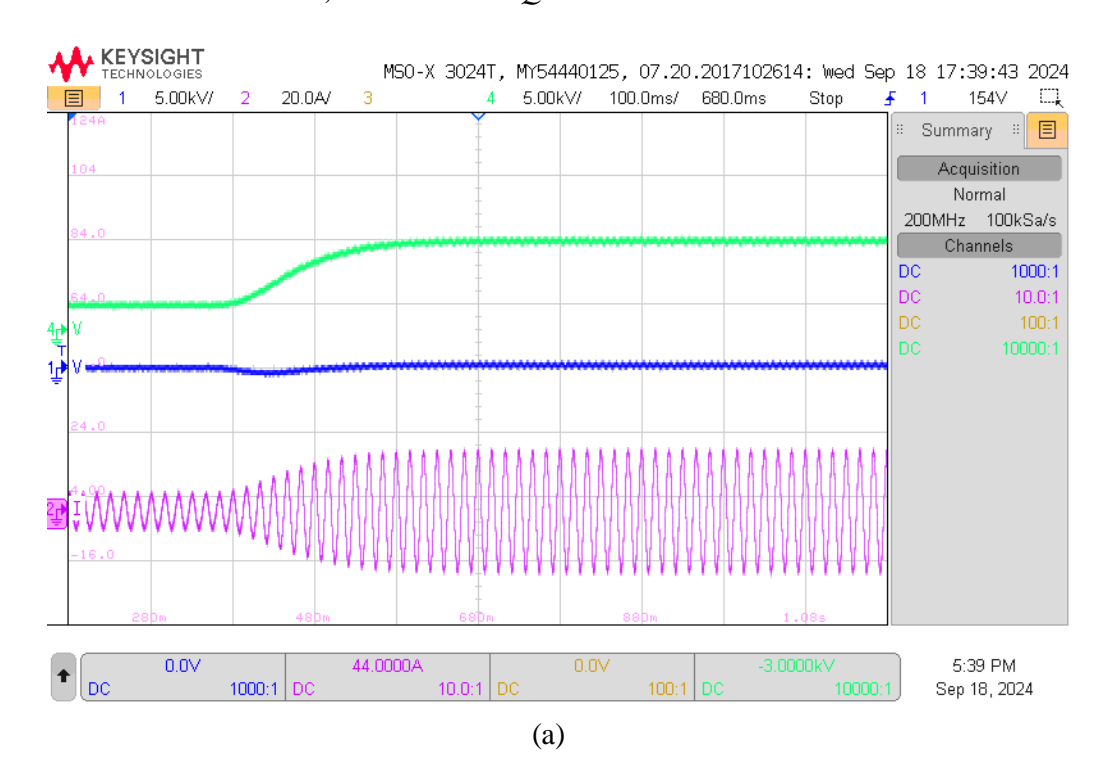
In this scenario, the GFM inverter initially supplies 5 kW of P_e and 0 kVAr of Q_e to the grid. Subsequently, P_e^* is set to 10 kW. Next, different grid SCR conditions are evaluated. In the following figures, P_e (green curve), Q_e (blue curve), and the current injected from one of the phases (lilac curve) are shown.

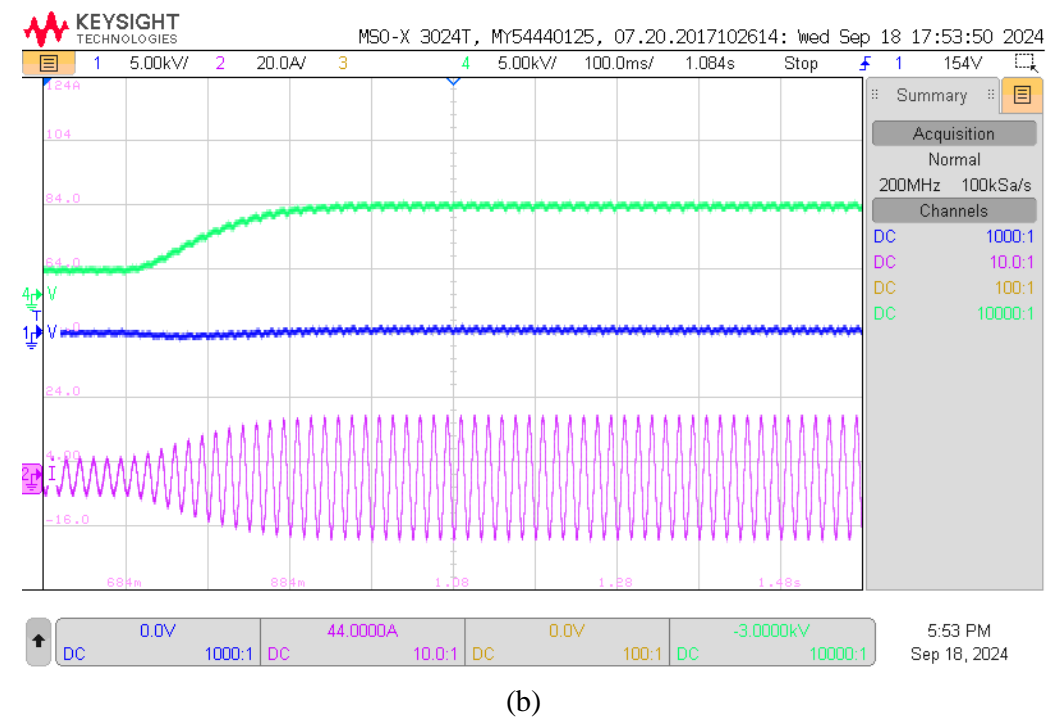
A. SCR = 2.57

Initially, a short circuit ratio (SCR) value of 2.57 was considered, which characterizes a weak grid, as it is lower than 3 [106]. In this case, the value of U_n is reduced to $180\sqrt{2}$ V to reduce the high inductance requirements of the grid. The value of L_g is 10 mH.

Based on Figure 3-37 (a) - (b), it can be observed that the use of DID has little or almost no influence on the response of the electrical variables. This was expected, since a GFM inverter tends to operate more stably in weak grids. In fact, the most challenging scenario for a GFM inverter is its operation in strong grids.

Figure 3-37 – Injected active power, reactive power and current: (a) without DID; (b) with DID. Green curves – P; Blue curves – Q: Lilac curves – current. SCR = 2.57.





B. SCR = 3.85

In this second test, the SCR value is 3.85 to characterize a strong grid. The value of U_n is the same as shown in Table 3-7. The value of L_q is 10 mH.

From Figure 3-38 (a) – (b), it can be observed that when DID is applied, all three parameters – active power, reactive power, and current – exhibit less oscillation at the moment the P_e^* changes. In the case without DID, the overshoot is approximately 6 %, whereas with DID it is reduced to about 4.1 %. The settling time was approximately 400 ms without DID and 250 ms with DID.

C.
$$SCR = 7.7$$

The next test was carried out considering an SCR of 7.7, which represents a stronger grid compared to the previous cases. The value of L_g is 5 mH.

Figure 3-39 (a) - (b) shows that the use of DID significantly improves the dynamic response of the variables in question. In the case without DID, the overshoot was 12.1%, whereas with DID it was reduced to 8%. It can be observed that without DID, the system is highly oscillatory, with oscillations lasting several seconds, while with DID, the settling time is only approximately 400 ms.

D. SCR = 19.25

The final test considers a grid with an SCR of 19.25, and the value of L_g is 2 mH. From Figure 3-40 (a) - (b), it can be observed that the absence of DID significantly deteriorates the dynamic response of the electrical variables. In addition to exhibiting an overshoot of 19 %, subsynchronous oscillations at a frequency of 2.5 Hz emerge (zoom view). In contrast, the implementation of DID effectively mitigates the oscillatory behavior. As a result, the active power shows a reduced overshoot of 13.1 %, and the settling time is approximately 400 ms, when compared to the case without DID.

The presented results confirm what was discussed in the theoretical background, where the use of DID improves the system's open-loop gain and, consequently, the inverter's performance under disturbances. Furthermore, the influence of the voltage control loop on the operation of the power control loops is demonstrated. Therefore, using DID improves the dynamic behavior of the GFM inverter by providing more damping, which helps control fluctuations and ensures the system stabilizes more rapidly

Figure 3-38 – Injected active power, reactive power and current: (a) without DID; (b) with DID. Green curves – P; Blue curves – Q: Lilac curves – current. SCR = 3.85.

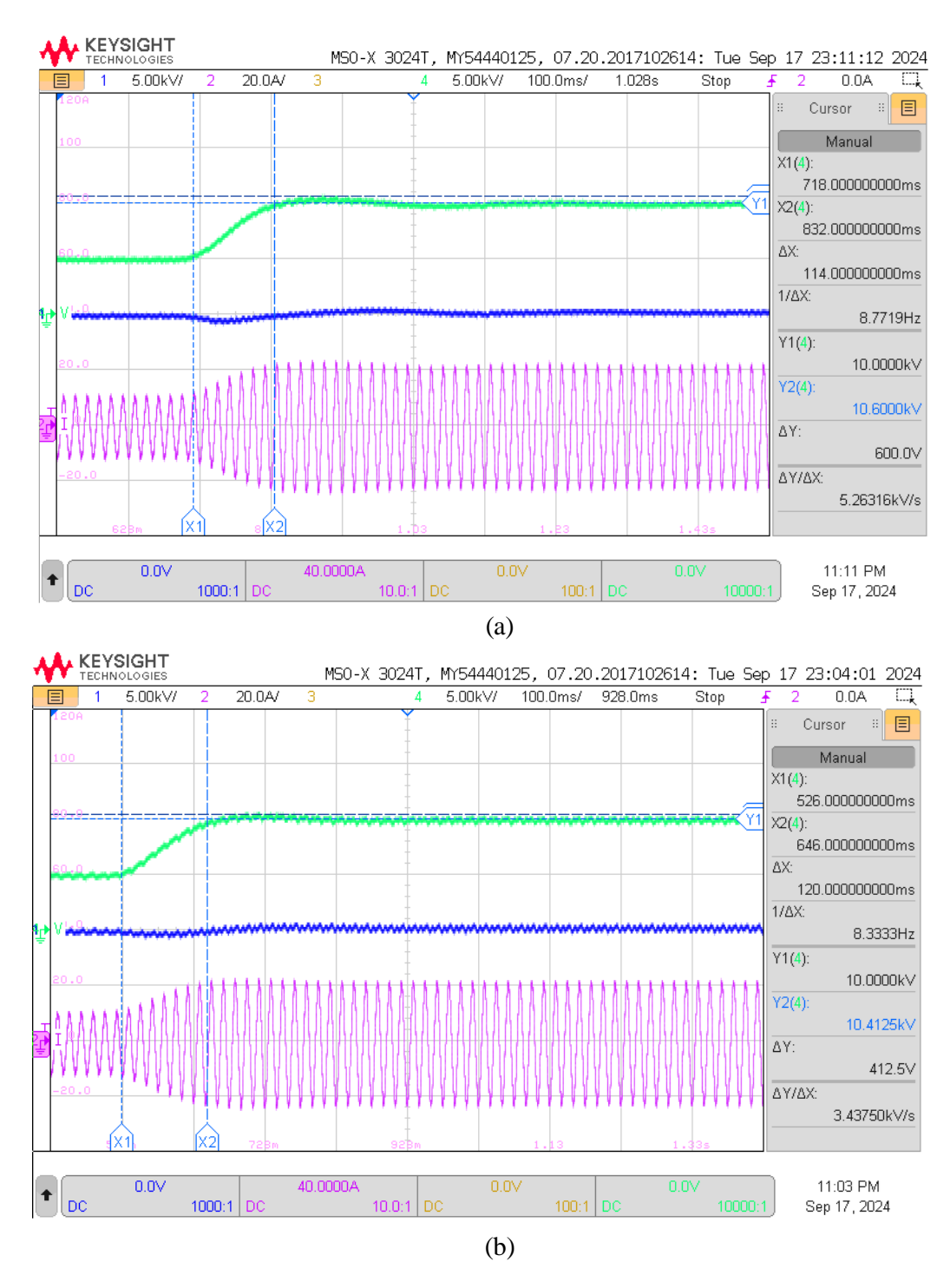


Figure 3-39 – Injected active power, reactive power and current: (a) without DID; (b) with DID. Green curves – P; Blue curves – Q: Lilac curves – current. SCR = 7.7.

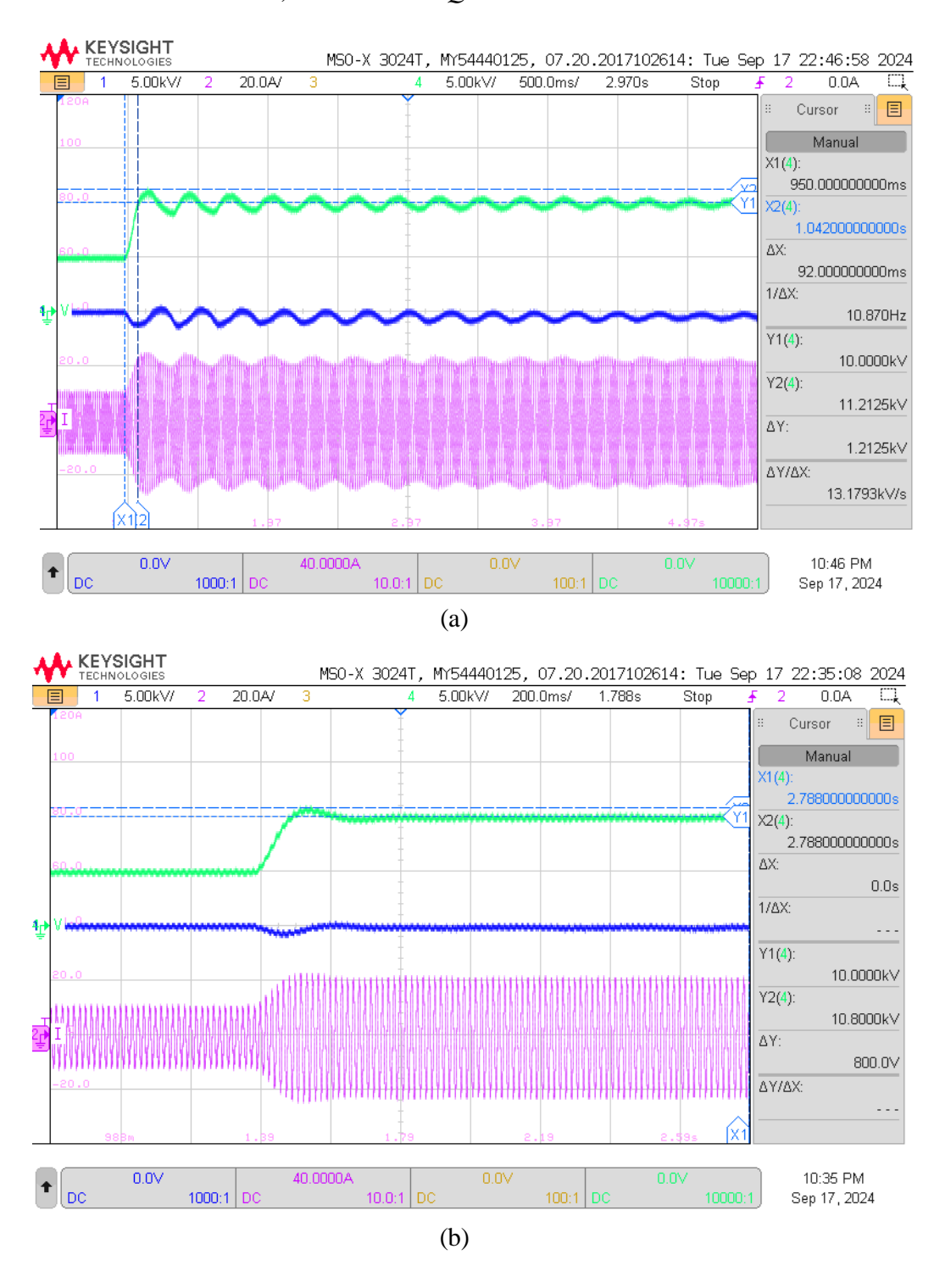
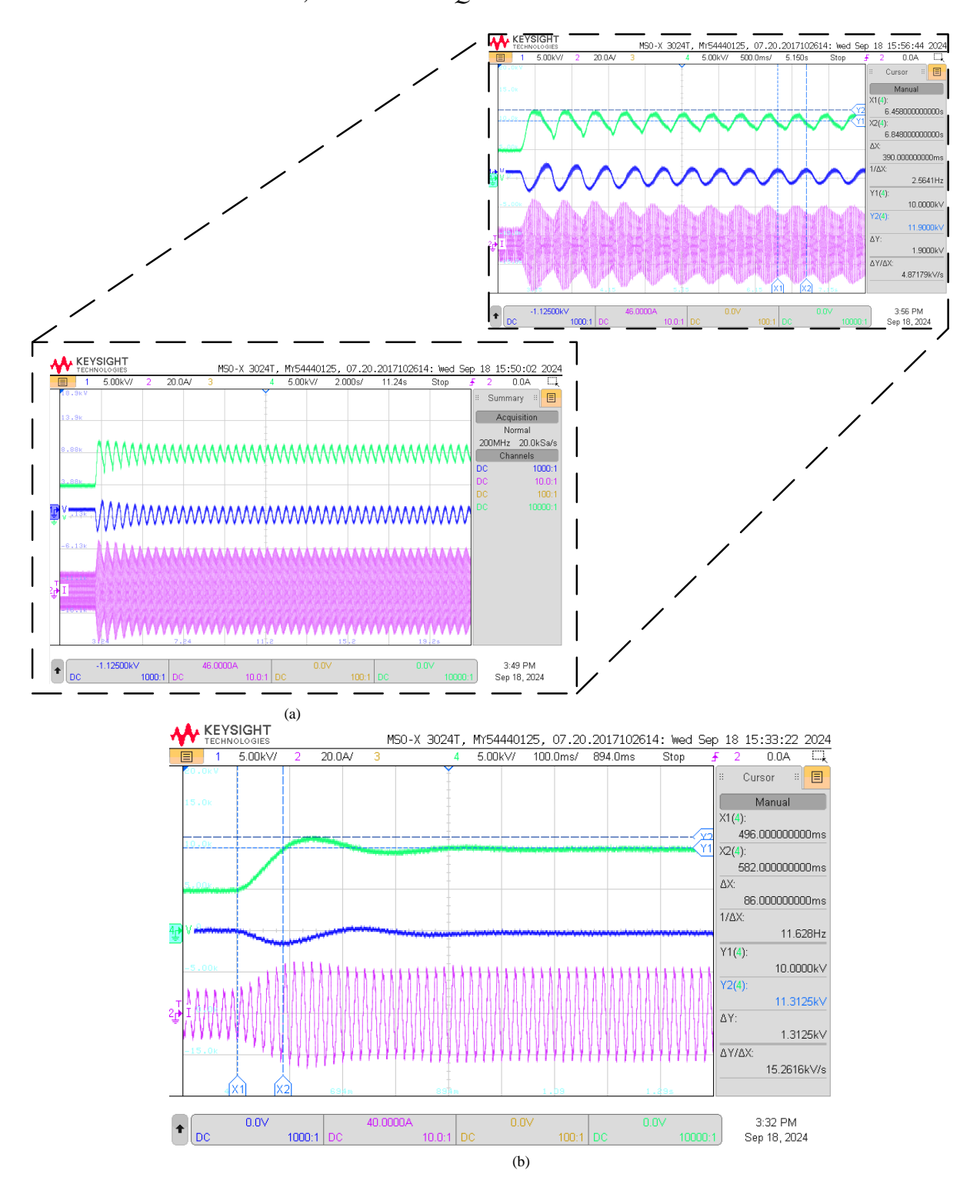


Figure 3-40 – Injected active power, reactive power and current: (a) without DID; (b) with DID. Green curves – P; Blue curves – Q: Lilac curves – current. SCR = 19.25.



3.12 Chapter Summary

This chapter initially presented the mathematical modelling of the LCL filter, which was the subject of study. Next, the effect of resonance, an inherent characteristic of this type of filter, was discussed, along with the existing damping techniques used to mitigate this resonance.

Subsequently, the effect of computational delay on the active damping technique using the capacitor current was presented. It is shown that computational delay has an adverse effect on this technique, which can lead the control system to become unstable within a certain frequency range.

The concept of passivity was also introduced as an alternative to provide sufficient conditions for the stability of a linear system, without depending on the configuration or number of converters connected to the grid.

Then, the design of the proposed current controller was presented, based on a high-bandwidth lead compensator, a CCFAD composed of lead compensation, and a CVD employing lead-lag compensation. Theoretical analyses and experimental results demonstrated the stability and superiority of the proposed technique compared to other strategies.

Next, the design of the proposed voltage controller was presented, which employed a PR controller with a DID function to improve the inverter's dynamic response.

The modelling of the virtual impedance loop and the active and reactive power control loops were also presented. Furthermore, the influence of the voltage control loop on the power control loops was shown.

Finally, experimental results of the VSM operating in both islanded mode and gridconnected mode under different SCR values demonstrated the effectiveness of using DID in providing better dynamic response of the inverter's electrical variables.

CHAPTER IV

4 Virtual Synchronous Machine Control – DC Side

This chapter presents the control strategy for the VSM on the DC side. It includes the modelling of the battery current control and the DC-link voltage control.

4.1 System Description

The DC side stage consists of a battery bank with a bidirectional DC-DC converter. Using

Figure 3-15 as a reference, we have: L_{dc} is the inductance of the DC-DC converter, R_{dc} is the ESR of L_{dc} , C_{dc} is the capacitance of the DC bus, V_B is the battery bank voltage and V_{dc} is the DC bus voltage.

The controller of the DC-DC converter is fundamentally focused on regulating V_{dc} and the current in L_{dc} , I_L . A dual-control loop is used for the DC-DC converter, where a PI controller is employed to bring V_{dc} to the reference value V_{dc}^* . The output of this controller provides the current reference, I_L^* , which is used to regulate I_L , and is also controlled by a PI controller. The output of the PI controller provides the control signal to the PWM block, which will generate the pulses to drive switches Q_I and Q_2 .

4.2 DC-Link Voltage Control

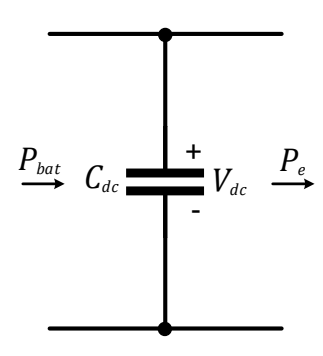
The voltage across the terminals of C_{dc} can be modelled as a function that depends on the difference between the power at the battery bank terminals, P_{bat} , and the output power of the GFM inverter, P_e , as shown in Figure 4-1. Neglecting losses, the power balance equation, given by (4.1), can be used to derive an equation for tuning the control loop of the DC-link voltage [6].

$$P_{bat} - P_e = \frac{1}{2} C_{dc} \frac{dV_{dc}^2}{dt}$$
 (4.1)

Equation (4.1) can be rewritten as (4.2) by making a change of variables such that $w_c = V_{dc}^2$ [107] and $P_{bat} = V_B \times I_L$.

$$\frac{dw_c}{dt} = \frac{2}{C_{dc}} (V_B I_L - P_e) \tag{4.2}$$

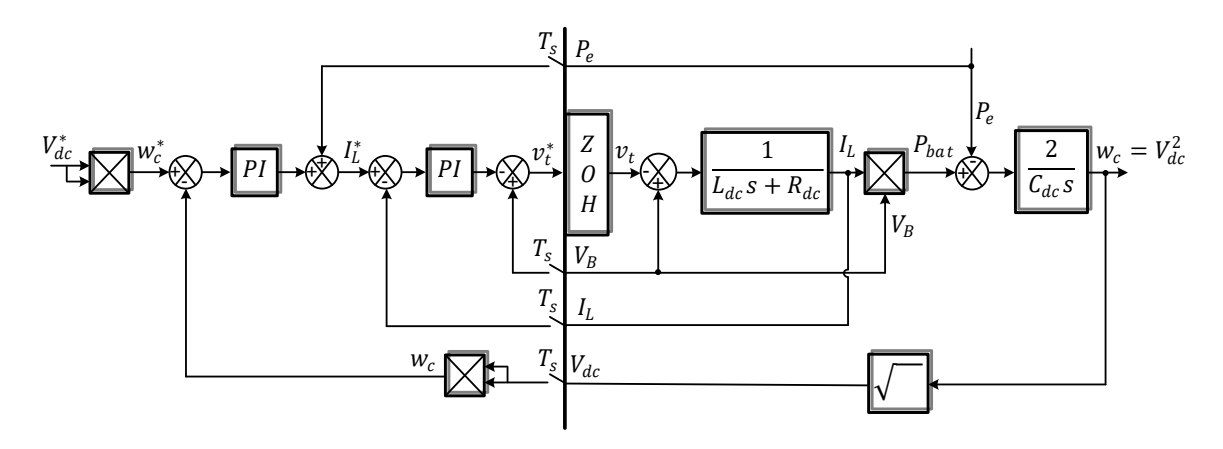
Figure 4-1 – DC-link power flow with ideal conversion.



Following the methodology presented in [6], the state equation of I_L is given by (4.3). Together with (4.2), this yields the block diagram that represents the DC-DC converter, shown in Figure 4-2. The variable v_t represents the average voltage across the collector-emitter terminals of switch Q_2 .

$$L_{dc}\frac{dI_L}{dt} = V_B - R_{dc}I_L - v_t \tag{4.3}$$

Figure 4-2 – Block diagram of the DC-link voltage control.



Source: Author.

4.2.1 Tuning of the Current Controller in L_{dc}

The block diagram of the discretized I_L control loop is shown in Figure 4-3, where K_{piL} is

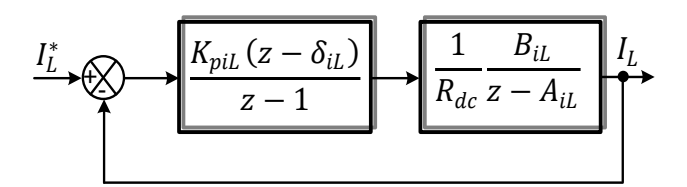
the PI gain, δ_{iL} is the zero of the controller, and B_{iL} and A_{iL} are the plant parameters, given by (4.4). The zero of the controller is tuned to cancel the effect of the pole of the plant. The gain K_{piL} can be calculated using (4.5), where f_{ci} is the bandwidth of the controller, which was chosen to be 300 Hz. The proportional gain, K_{pL} , and the integral gain, K_{iL} , are calculated using (4.6). The controller gains were calculated based on the converter parameters shown in Table 4-1, and their values are also presented in the same table. The computational delay was neglected in the controller tuning, as the small bandwidth made its effect on performance negligible.

$$\begin{cases}
A_{iL} = e^{-\frac{T_s R_{dC}}{L_{dC}}} \\
B_{iL} = 1 - A_{iL}
\end{cases}$$
(4.4)

$$K_{piL} = \frac{(1 - e^{-2\pi f_{ci}T_s})R_{dc}}{B_{iL}}$$
 (4.5)

$$\begin{cases}
K_{pL} = \delta_{iL} K_{piL} \\
K_{iL} = \frac{K_{piL} - K_{pL}}{T_{s}}
\end{cases}$$
(4.6)

Figure 4-3 – Block diagram for I_L control.



Source: Author.

4.2.2 Tuning of the Voltage Controller in V_{dc}

The block diagram for DC-link voltage control is shown in Figure 4-4. The parameters K_{pVdc} and K_{iVdc} are the proportional and integral gains of the PI controller. The parameters G_{iL} , δ_L , δ_V and K_{Vdc} are the plant parameters, which include the I_L control loop, approximated by an equivalent first-order system with a bandwidth of 300 Hz, and are shown in (4.7), where V_{BN} the battery's nominal voltage. The PI parameters were tuned in MATLAB to achieve a 30 Hz bandwidth and a phase margin of 75 degrees (to ensure stability and a well-damped response). All the control parameters are listed in Table 4-1.

$$\begin{cases} \delta_{L} = e^{-2\pi f_{ci}T_{S}} \\ G_{iL} = (1 - \delta_{L})V_{BN} \\ \delta_{V} = \frac{T_{S}\delta_{L} - \frac{(1 - \delta_{L})}{2\pi f_{ci}}}{T_{S} - \frac{(1 - \delta_{L})}{2\pi f_{ci}}} \\ K_{Vdc} = \frac{2}{C_{dc}} \left(\frac{T_{S}}{1 - \delta_{L}} - \frac{1}{2\pi f_{ci}} \right) \end{cases}$$
(4.7)

Figure 4-4 – Block diagram for V_{dc} control.

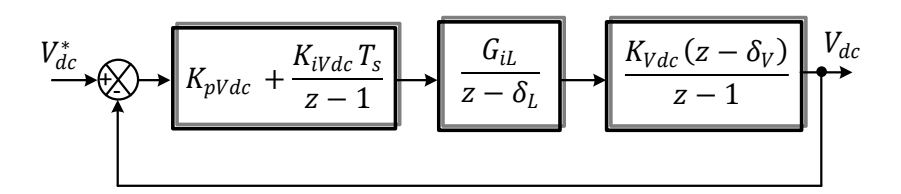


Table 4-1 – System and Control Parameters for the DC-DC Converter.

Parameter	Value	Description
DC-DC converter and battery parameters		
L_{dc}	8.8 mH	DC-DC converter inductance
R_{dc}	0.1 Ω	ESR of L_{dc}
C_{dc}	15 mF	DC bus capacitance
V_{dc}	650 V	DC bus voltage
V_{BN}	540 <i>V</i>	Battery nominal voltage
Control parameters for the DC-DC converter		
K_{pL}	15.6Ω	I_L controller proportional gain
K_{iL}	$171.8 \Omega s^{-1}$	I_L controller integral gain
K_{pVdc}	$0.002 A/V^2$	V_{dc} controller proportional gain
K_{iVdc}	$0.08 (A/V^2)s^{-1}$	V_{dc} controller integral gain

4.3 Simulation Results

To validate the control strategy, simulation results were conducted using the software MATLAB/Simulink. The system parameters are listed in Table 3-7 and Table 4-1. The bidirectional operation of the converter was analyzed, sometimes injecting power into the grid and at other times charging the battery bank. The SCR levels were deliberately chosen to ensure that the grid is strong, which is the most challenging grid type for GFM inverters. Situations without the proposed strategy, i.e., without the DID presented in Section 3.7.2, and with the proposed strategy, i.e., with the DID, were compared.

A. Without the proposed strategy -SCR = 6.38

Figure 4-5 shows the P_e and Q_e curves of the converter for an SCR = 6.38 and without DID. At $t \cong 0.93$ s, P^* and Q^* are set to inject 10 kW and 0 VAr, respectively, into the grid. As observed in the curves, both P_e and Q_e exhibit oscillatory behavior during the transient period. Notably, when power injection begins, P_e reaches a peak of approximately 15.5 kW—representing a 55 % overshoot. Simultaneously, Q_e reaches a minimum of -7.4 kVAr, compared to its steady-state value of -1.9 kVAr, resulting in an undershoot of 289 %. Both signals settle to their steady-state values in about 0.93 s.

At $t=2.5 \, s$, P^* is changed to -10 kW, indicating that the battery bank begins charging. In response, P_e reaches approximately -12 kW, corresponding to a 20 % undershoot. The new steady-state value of Q_e becomes 3.2 kVAr, with a peak of 10 kVAr during the transient, representing an overshoot of 212 %. Both signals settle to their steady-state values in about 0.6 s.

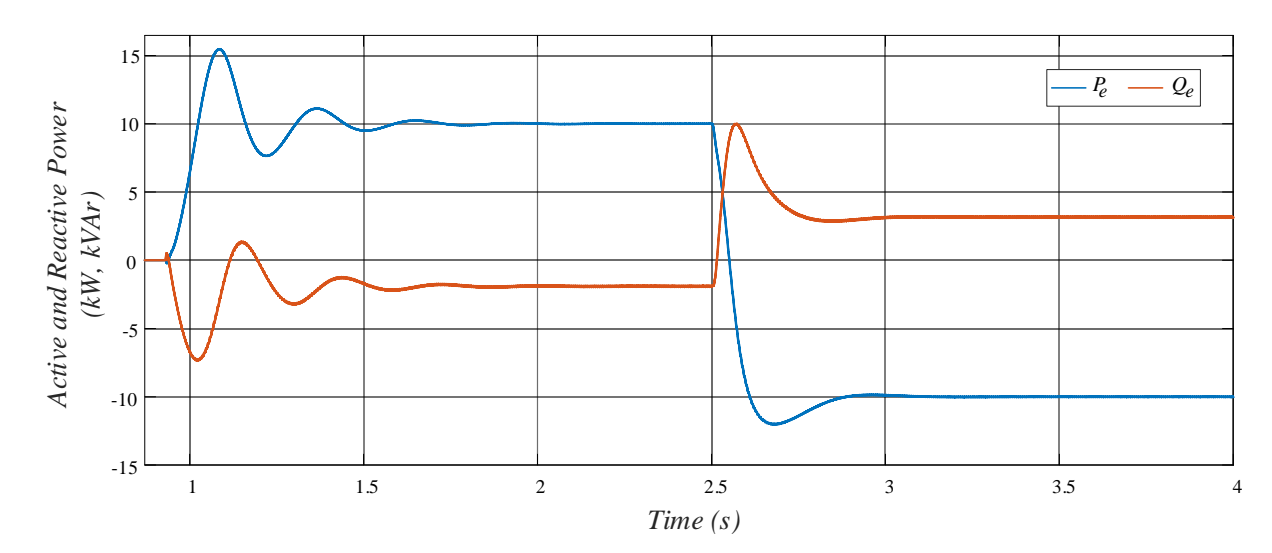


Figure 4-5 – P_e and Q_e curves without the strategy – SCR = 6.38.

B. With the proposed strategy – SCR = 6.38

Figure 4-6 shows the P_e and Q_e curves of the converter for an SCR = 6.38 and with DID. At $t \cong 0.93$ s, P^* is set to inject 10 kW into the grid. When power injection begins, P_e reaches a peak of approximately 10.1 kW—representing a 1.3 % overshoot. Simultaneously, Q_e reaches a minimum of -2.5 kVAr, resulting in an undershoot of 31.58 %. Both signals settle to their steady-state values in about 0.21 s.

At t = 2.5 s, P^* is changed to -10 kW. In response, P_e approaches its steady-state value of -10 kW exponentially. Meanwhile, Q_e peaks at 3.27 kVAr during the transient, representing an overshoot of 2.19 %. Both signals settle to their steady-state values in about 0.22 s.

Active and Reactive Power

White Power is a second of the second of the

Figure $4-6-P_e$ and Q_e curves with the strategy – SCR = 6.38.

C. Without the proposed strategy - SCR = 12.76

Figure 4-7 shows the P_e and Q_e curves of the converter for an SCR = 12.76 and without DID. At $t \cong 0.93$ s, P^* is set to inject 10 kW into the grid. As observed in the curves, both P_e and Q_e exhibit a much more oscillatory behavior than the previous case during the transient period. Notably, when power injection begins, P_e reaches a peak of approximately 20 kW—representing a 100 % overshoot. Simultaneously, Q_e reaches a minimum of -14.4 kVAr, compared to its steady-state value of -3.4 kVAr, resulting in an undershoot of 324 %. Both signals settle to their steady-state values in about 3.14 s.

At t = 4.5 s, P^* is changed to -10 kW. In response, P_e reaches approximately -12.9 kW, corresponding to a 29 % undershoot. The new steady-state value of Q_e becomes 4.2 kVAr, with a peak of 13.2 kVAr during the transient, representing an overshoot of 214 %. Both signals settle to their steady-state values in about 0.7 s.

Figure 4-7 – P_e and Q_e curves without the strategy – SCR = 12.76.

D. With the proposed strategy - SCR = 12.76

Figure 4-8 shows the P_e and Q_e curves of the converter for an SCR = 12.76 and with DID. At $t \cong 0.93$ s, P^* is set to inject 10 kW into the grid. When power injection begins, P_e reaches a peak of approximately 10.75 kW—representing a 7.5 % overshoot. Simultaneously, Q_e reaches a minimum of –4.74 kVAr, resulting in an undershoot of 39.41 %. Both signals settle to their steady-state values in about 0.17 s.

At $t \cong 1.5 \text{ s}$, P^* is changed to -10 kW. In response, P_e reaches approximately -10.2 kW, corresponding to a 2 % undershoot. Meanwhile, Q_e peaks at 4.85 kVAr during the transient, representing an overshoot of 15.48 %. Both signals settle to their steady-state values in about 0.1 s.

Time (s)

Active and Reactive Power

Active and Reactive Power

(KW, KVAT)

(W, KVAT)

(

Figure $4-8 - P_e$ and Q_e curves with the strategy – SCR = 12.76.

The overall results demonstrate that the converter's performance significantly improves when the proposed DID strategy is applied. In both SCR scenarios (6.38 and 12.76), the use of DID leads to a substantial reduction in overshoot and undershoot for both P_e and Q_e , as well as much faster settling times. This improved performance is attributed to the enhanced damping and dynamic response introduced by the DID, which effectively mitigates oscillations during transient events such as power injection or battery charging. Consequently, the system becomes more stable and responsive, especially under stronger grid conditions where oscillations are typically more pronounced.

4.4 Chapter Summary

This chapter presented the proposed control strategy for the DC side of the VSM. PI controllers were employed to regulate the battery current and the DC-link voltage. Prior to controller tuning, the modelling of the plant was carried out to support the control design.

Simulation results under two SCR conditions (6.38 and 12.76) demonstrated the effectiveness of the proposed DID strategy in improving the dynamic response of the converter when injecting power into the grid or charging the battery, significantly reducing overshoot, undershoot, and settling time of the electrical variables.

CHAPTER V

5 Analysis of Converter Operation in a Microgrid

This chapter presents the performance of the VSM operating in a microgrid, analyzed through simulations using MATLAB/Simulink, considering only the grid-connected operation. The components that make up the system are shown in Figure 5-1. As illustrated, the complete microgrid consists of two VSMs, each with its own DC link and control system, along with one GFL inverter, where the DC side of the GFL inverter is modeled as an ideal DC voltage source, and both linear and nonlinear loads are included. The parameters of the GFM inverters and the GFL inverter are the same as those used to obtain the results presented in Chapters 3 and 4. The linear load is a 5 kW three-phase load, and the nonlinear load consists essentially of a rectifier bridge feeding an LC filter (inductor L_{NL} and capacitor C_{NL}), with a resistor R_{NL} in parallel with C_{NL} . The values of L_{NL} , C_{NL} , and R_{NL} are 100 μ H, 470 μ F, and 150 Ω , respectively. The following subsections evaluate several simulation scenarios of the microgrid.

GFM Inverter Load

GFM Inverter Load

GFL Inverter Grid

Figure 5-1 – Microgrid schematic diagram.

Source: Author.

5.1 Scenario 1 – Parallel Operation of GFM and GFL Inverters

In the first scenario, the GFL inverter is configured to inject a peak current of 20 A into the grid. Subsequently, a GFM inverter is connected in parallel with the system and begins injecting power into the grid. Two cases are analyzed: the GFL inverter and the GFM inverter operating

with and without the G_{cvd} function.

In Figure 5-2 (a), the three-phase currents of the GFL inverter without G_{cvd} are shown, and Figure 5-2 (b) provides a zoomed-in view of the injected current. Similarly, Figure 5-3 (a) shows the three-phase currents of the GFL inverter with G_{cvd} , and Figure 5-3 (b) presents a zoomed-in view of the injected current.

By analyzing the figures, it is observed that the current is more oscillatory in the case without G_{cvd} , both at the moment the GFM inverter is connected and during steady-state operation, where it can be clearly seen that the current exhibits greater oscillation.

Figure 5-2 – (a) Injected current of the GFL inverter without G_{cvd} , operating in parallel with a GFM inverter without G_{cvd} ; (b) Zoomed-in view.

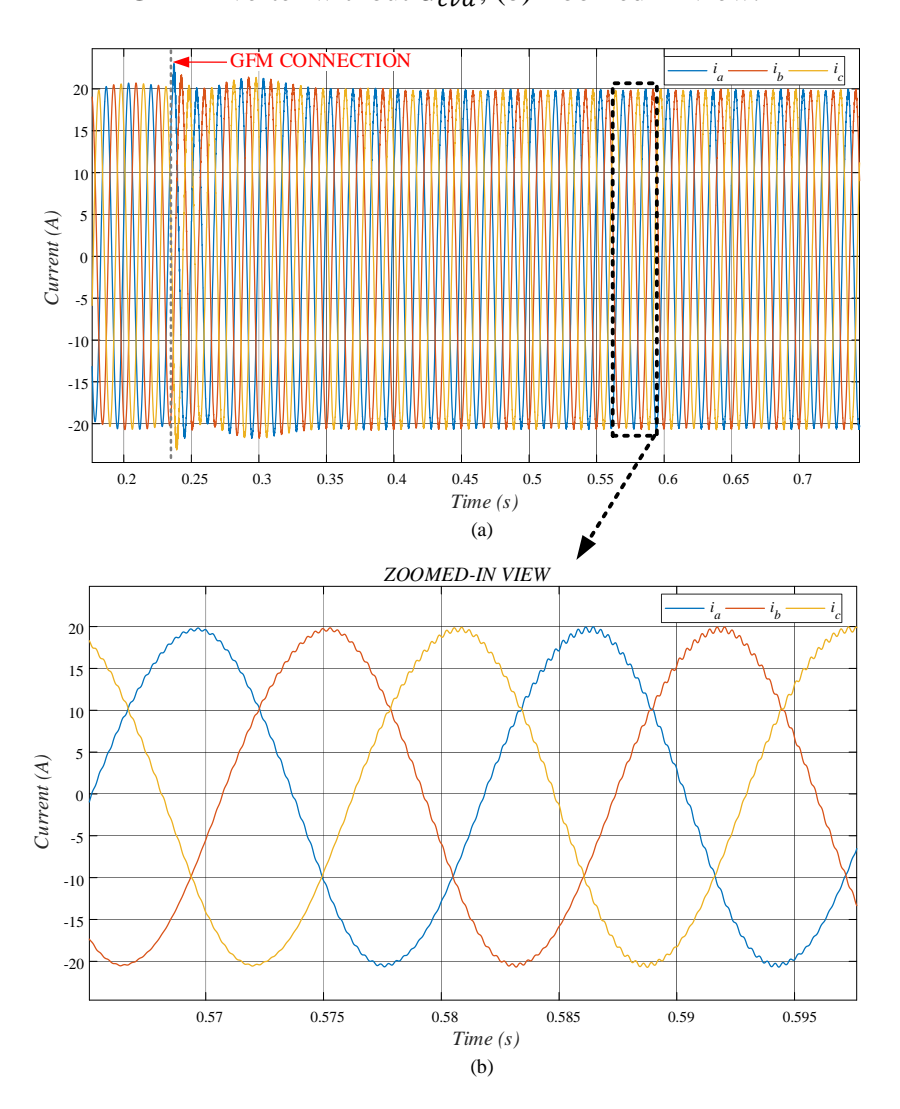


Figure 5-3 – (a) Injected current of the GFL inverter with G_{cvd} , operating in parallel with a GFM inverter with G_{cvd} ; (b) Zoomed-in view.

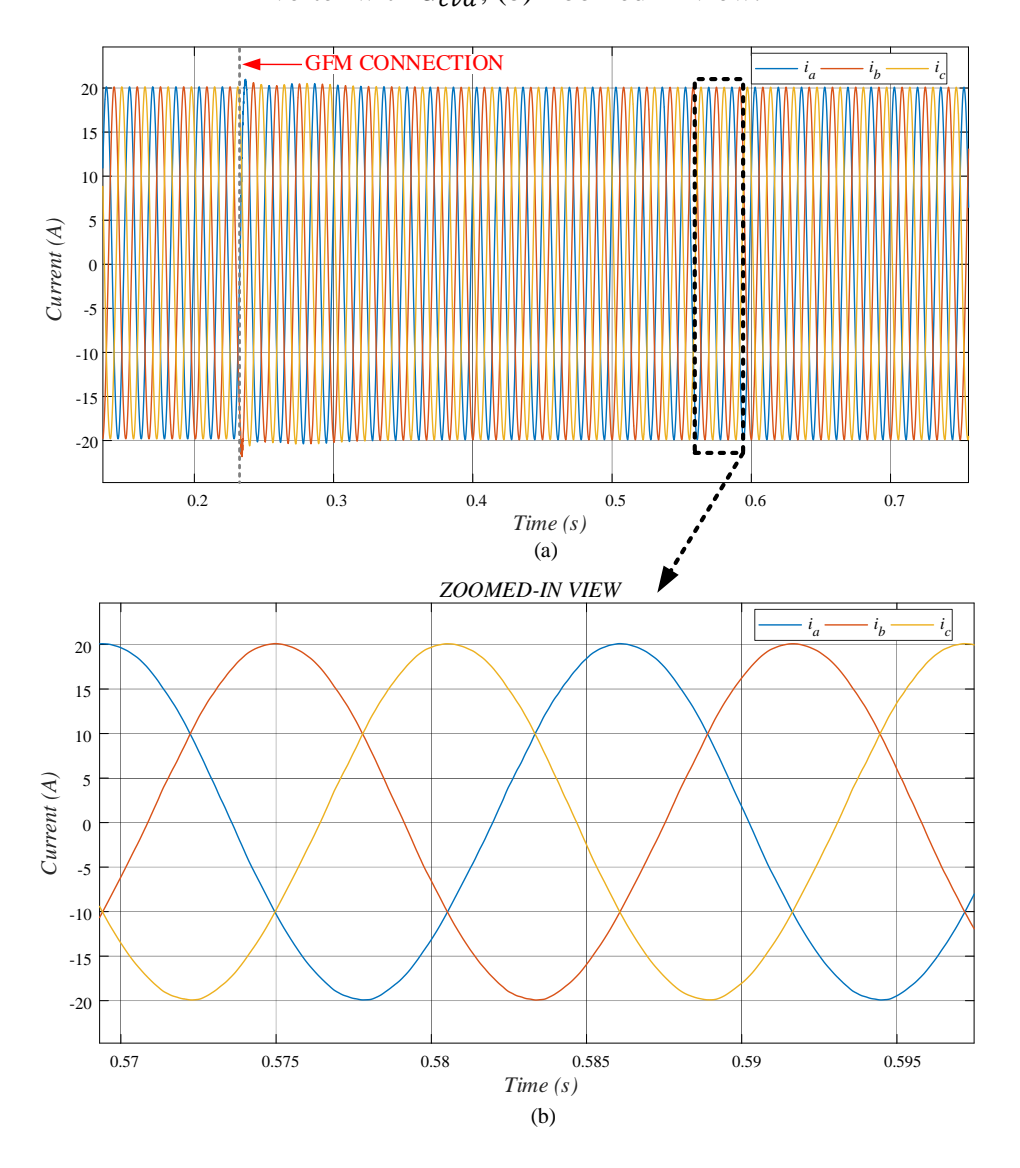


Figure 5-4 (a) and Figure 5-4 (b) show the three-phase currents of the GFM inverter for the case where both inverters operate without G_{cvd} , with the latter providing a zoomed-in view of the current waveform.

Similarly, Figure 5-5 (a) and Figure 5-5 (b) present the GFM inverter currents when both inverters operate with G_{cvd} , again with a zoomed-in detail shown in part (b).

As also observed in the GFL inverter waveforms, the GFM inverter exhibits more oscillatory behavior in steady state when G_{cvd} is not employed.

Figure 5-4 – (a) Injected current of the GFM inverter without G_{cvd} , operating in parallel with a GFL inverter without G_{cvd} ; (b) Zoomed-in view.

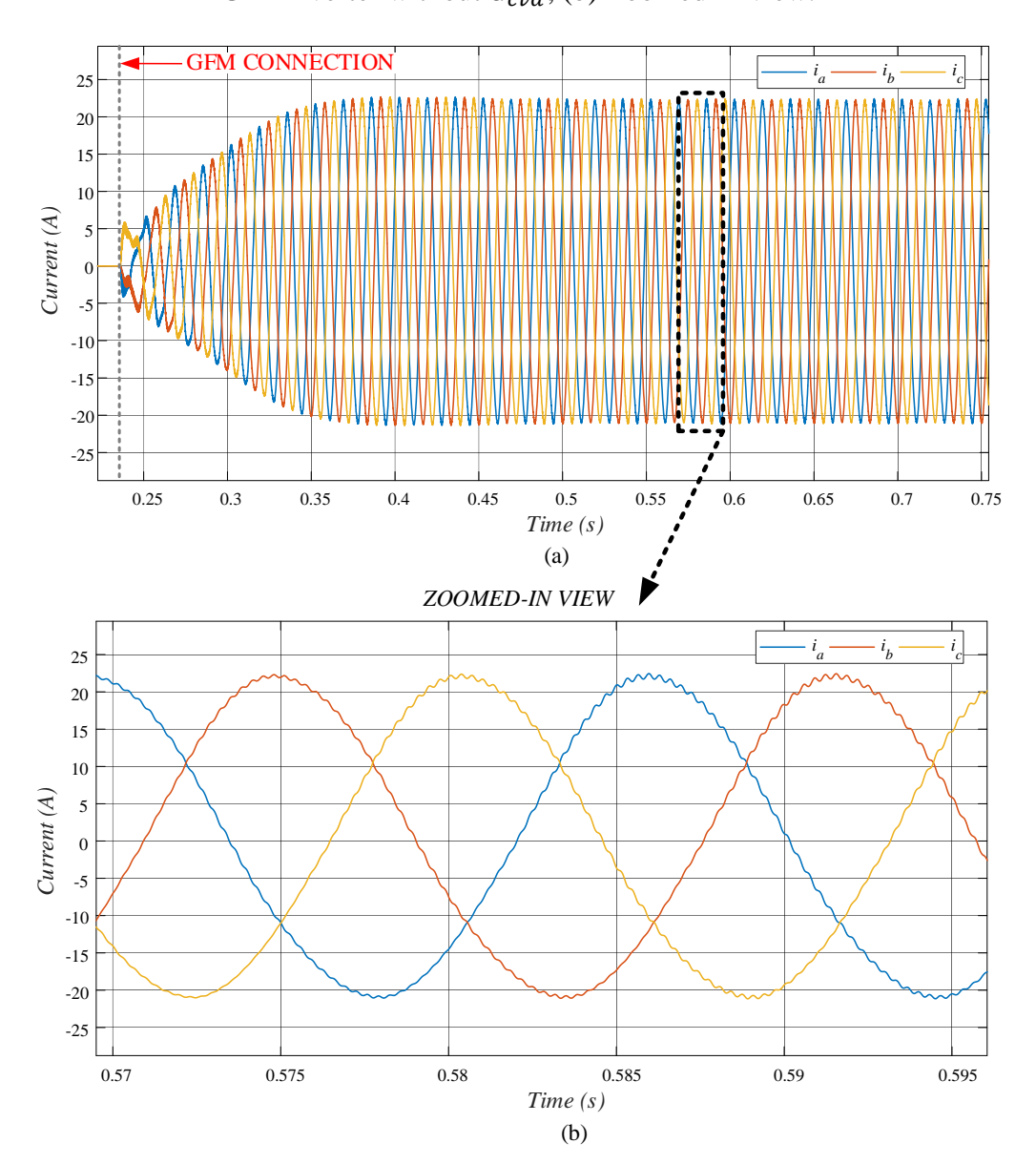
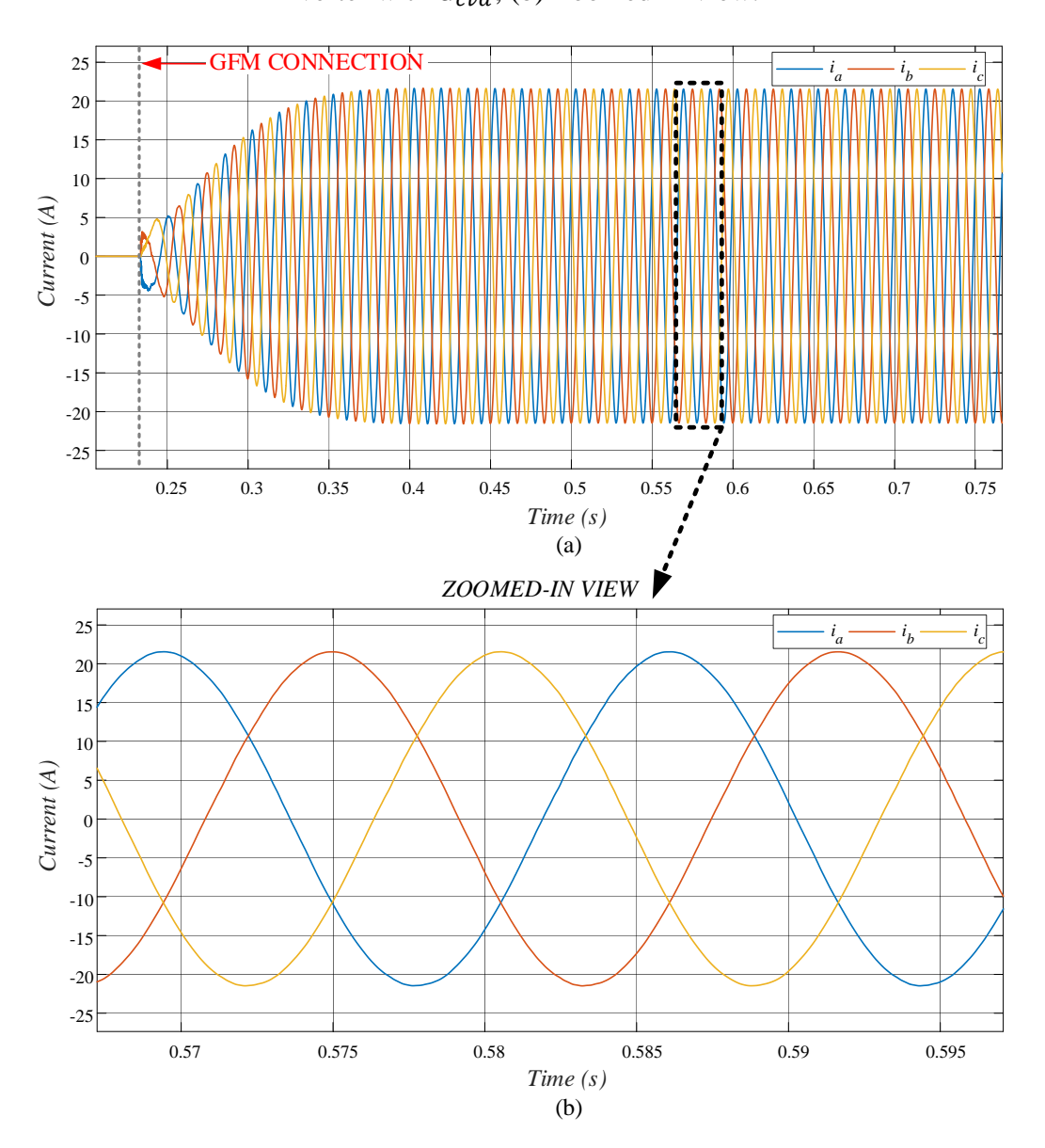


Figure 5-5 – (a) Injected current of the GFM inverter with G_{cvd} , operating in parallel with a GFL inverter with G_{cvd} ; (b) Zoomed-in view.



5.2 Scenario 2 – Low-Voltage Ride-Through Capability Assessment

In this scenario, the GFL inverter operates in parallel with the GFM inverter, and at t = 1.5 s, a 50 % grid voltage sag occurs, lasting for 200 ms. The cases with and without G_{cvd} in the GFL inverter are analyzed. In both cases the GFM inverter operates with G_{cvd} .

Figure 5-6 shows the three-phase currents of the GFL inverter without G_{cvd} . It can be

observed that the current reaches a maximum of 34.8 A and a minimum of -29.9 A at the moment the grid voltage sags. Figure 5-7 presents the three-phase currents of the GFL inverter with G_{cvd} . In this case, the current reaches a maximum of 29.2 A and a minimum of -25.4 A, indicating better performance compared to the previous case.

Furthermore, it is noticeable that when the grid voltage returns to its nominal value, the transient response of the currents in the second case is improved when compared to the first one.

40 34.8 A 30 20 Current (A) 0 -10 -30 **VOLTAGE SAG** -40 1.5 1.55 1.6 1.65 1.7 1.75 1.8 1.85 1.9 Time(s)

Figure 5-6 – Injected current of the GFL inverter without G_{cvd} during a voltage sag.

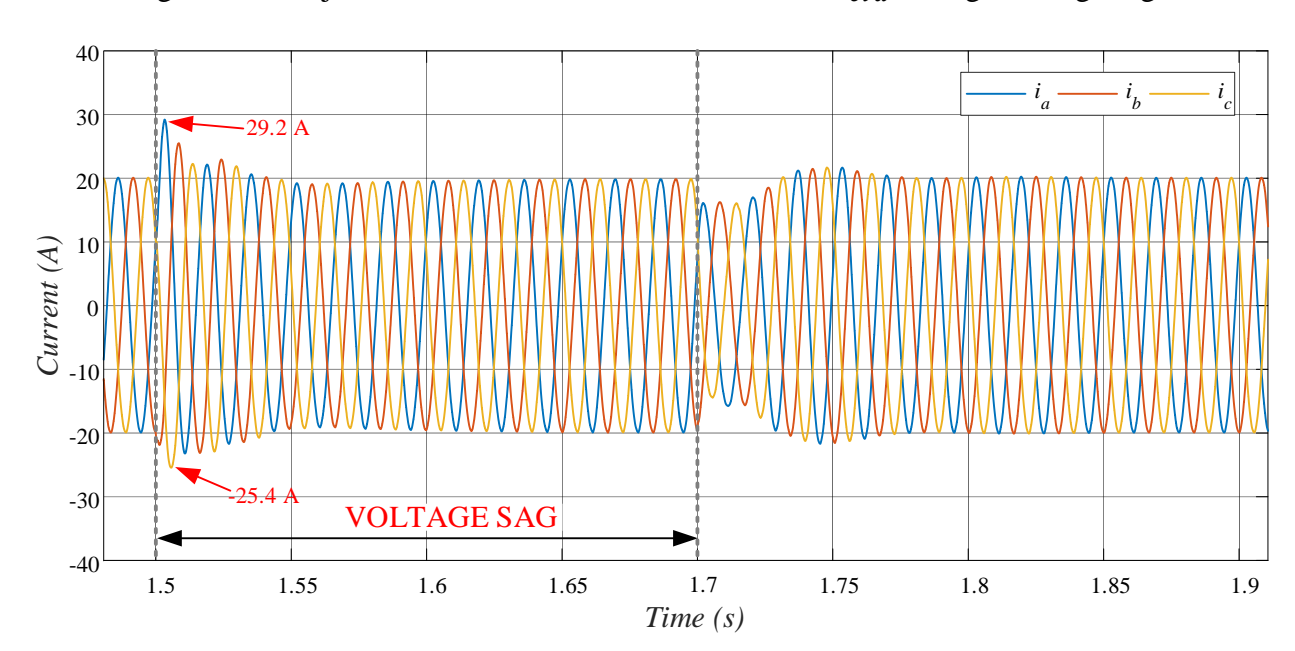


Figure 5-7 – Injected current of the GFL inverter with G_{cvd} during a voltage sag.

Figure 5-8 and Figure 5-9 show the three-phase currents of the GFM inverter, which includes G_{cvd} in both cases, operating in parallel with the GFL inverter, without and with G_{cvd} , respectively. As observed, the use or absence of G_{cvd} in the GFL inverter does not cause significant changes in the response of the GFM inverter.

To limit the current during the transient, the adaptive current-limiting virtual impedance is used. The red dashed lines show the allowed value of I_M for the current during the transient, which is equal to 150 % of the nominal peak current. As can be observed, the current was correctly limited, and after the voltage sag ended, the converter continued to provide the requested current as before the voltage sag event.

Figure 5-8 – Injected current of the GFM inverter during a voltage sag, with the GFL inverter operating without G_{cvd} .

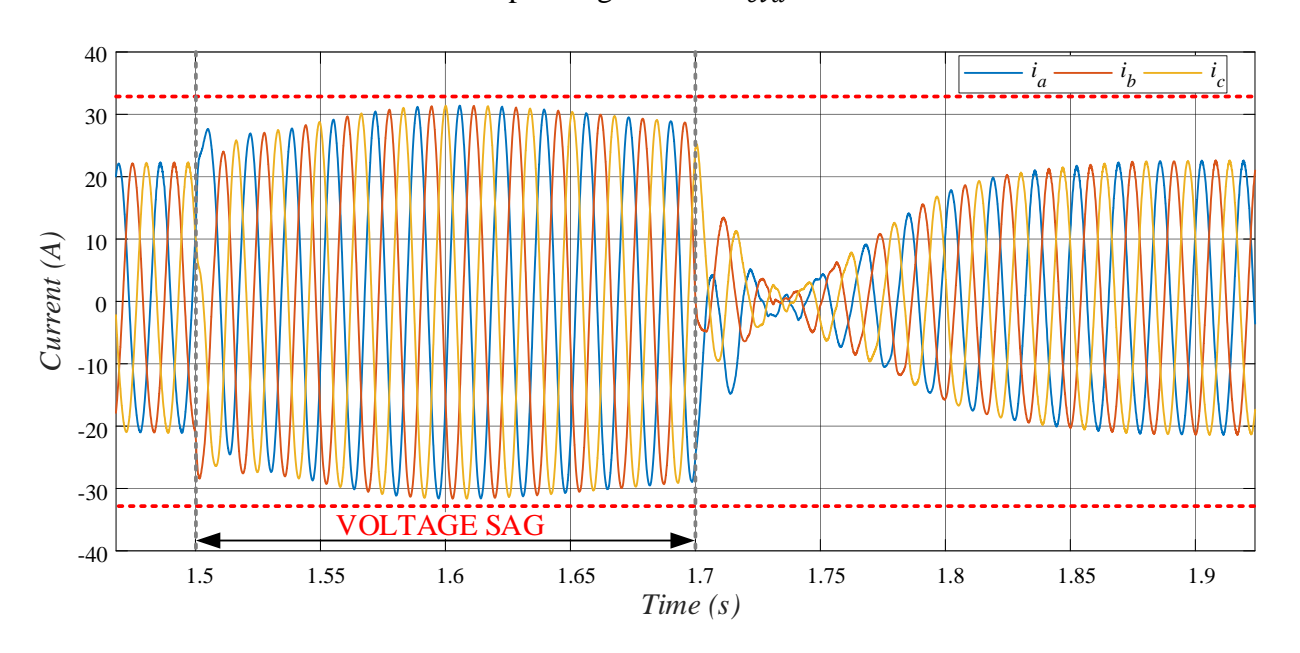
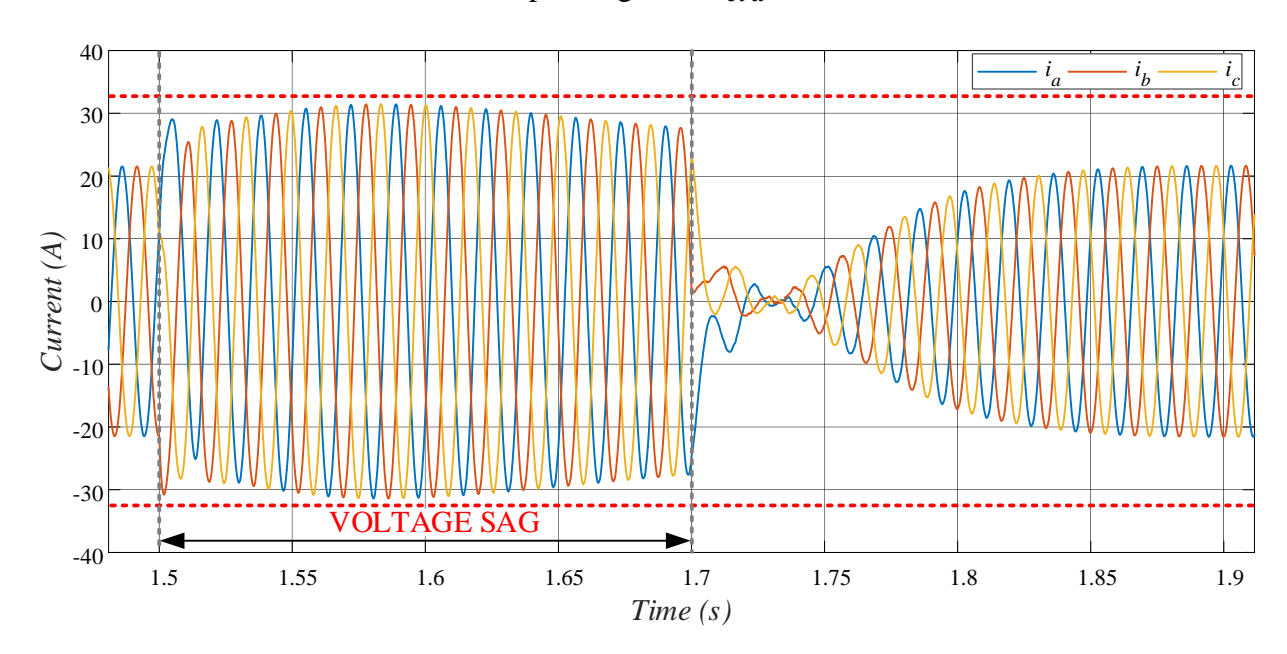


Figure 5-9 – Injected current of the GFM inverter during a voltage sag, with the GFL inverter operating with G_{cvd} .



5.3 Scenario 3 – Parallel Operation of GFM Inverters

The third scenario analyses the parallel operation of two GFM inverters. The SCR value is 3.2. Initially, the GFL inverter and one GFM inverter are already connected to the grid, supplying power to it and to the linear load. Subsequently, the second GFM inverter begins the synchronization process with the grid, and at t = 2 s, it is connected to the grid, injecting 10 kW. Figure 5-10 and Figure 5-11 show the active power responses of both converters, denoted as P_{e1} and P_{e2} , when operating without and with DID, respectively.

As observed, the power peak reached by the second GFM inverter was 16.1 kW without the use of DID, and 13.7 kW with the use of DID. As for the first GFM inverter, at the moment of connection, the power reached 6.9 kW without DID and 7.7 kW with DID, before returning to its nominal value.

It is also noted that the system shown in Figure 5-10 reached steady-state in approximately 0.6 s, while the system in Figure 5-11 took around 1.5 s. Additionally, P_{e1} and P_{e2} were significantly more oscillatory during the transient period when the converters operated without DID.

Therefore, once again, the improvement in the dynamic response of the converters when DID is used becomes evident.

Figure 5-12 shows the THD of the current injected into the grid in one of the phases, which was 0.93 %. It is observed that this value complies with the standards established by IEEE 519-2014 [108].

Figure 5-10 – Active powers of the GFM inverters during parallel operation without DID.

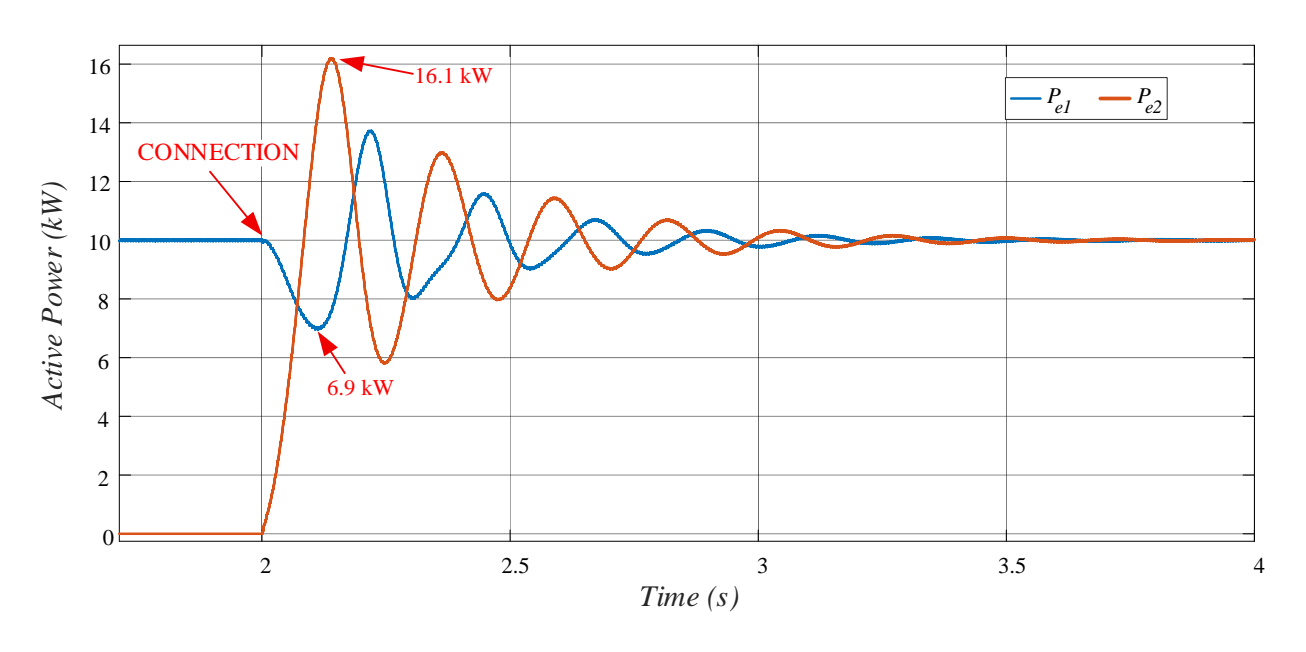
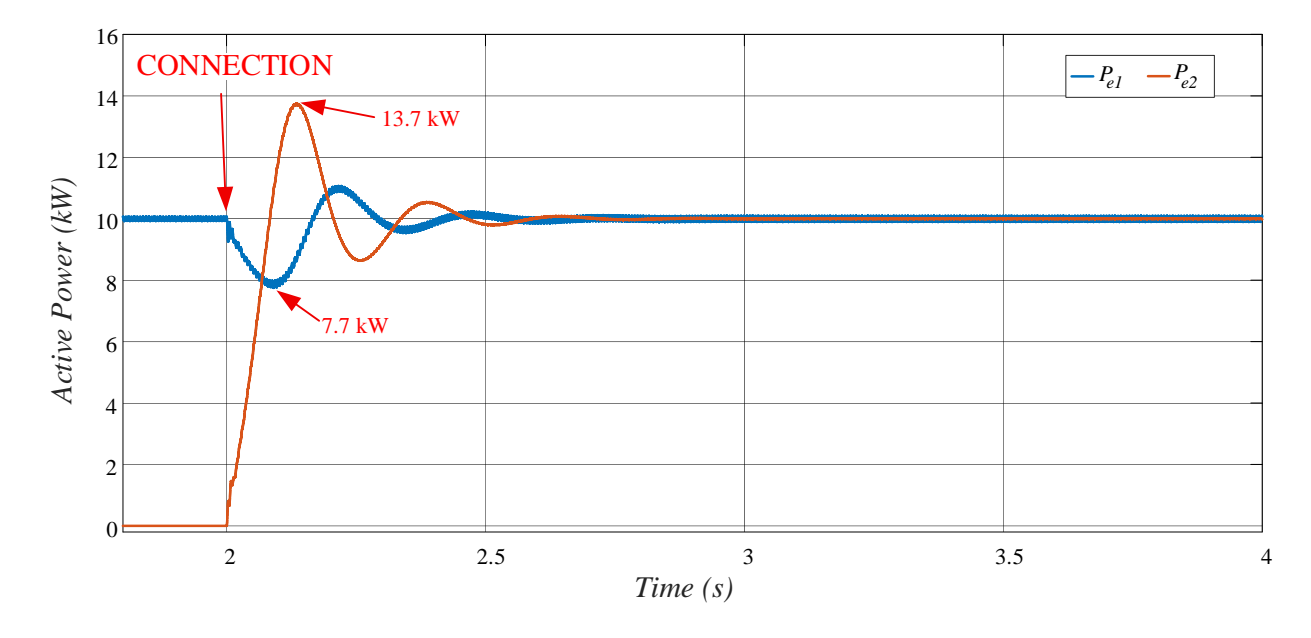


Figure 5-11 – Active powers of the GFM inverters during parallel operation with DID.



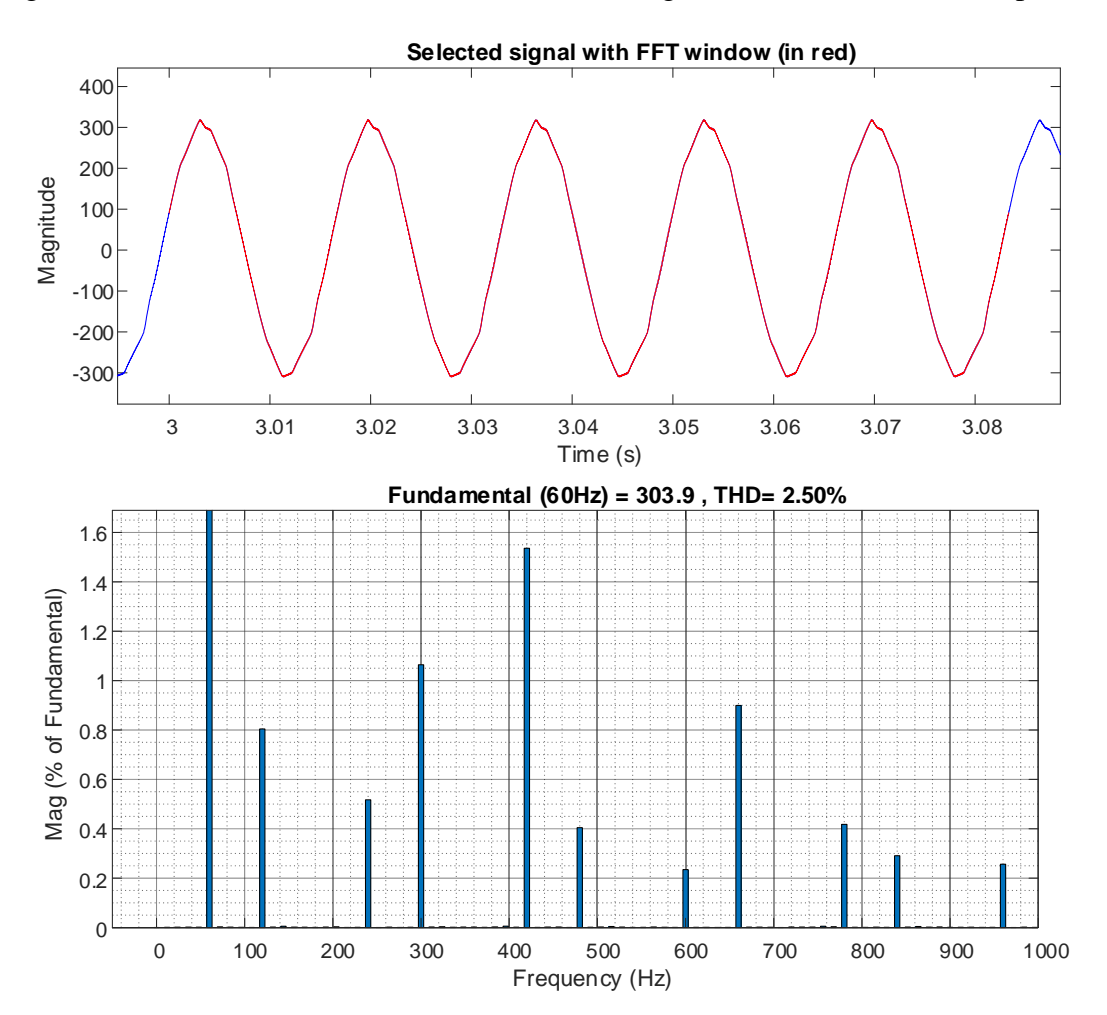
Selected signal with FFT window (in red) 50 Magnitude 3.01 3.07 3.02 3.03 3.04 3.05 3.08 3.09 Time (s) Fundamental (60Hz) = 53.56, THD= 0.93% 0.9 Mag (% of Fundamental) 0.7 0.6 0.5 0.1 0 0 100 200 300 500 600 700 800 900 1000 Frequency (Hz)

Figure 5-12 – Total harmonic distortion of the current injected into the grid in one of the phases.

5.4 Scenario 4 – Power Quality Assessment of the Microgrid

In this scenario, the steady-state operation of the microgrid is analyzed with all its components, including the nonlinear load. Figure 5-13 shows the voltage THD in one of the phases at the PCC, which is 2.5 %, and Figure 5-14 shows the current THD in one of the phases at the PCC, which is 1.73 %. It is observed that both values comply with the standards established by IEEE 519-2014 [108].

Figure 5-13 – Total harmonic distortion of the voltage at the PCC in one of the phases.



Selected signal with FFT window (in red) 40 20 Magnitude -40 -60 -80 3.04 3 3.01 3.02 3.03 3.05 3.06 3.07 3.08 Time (s) Fundamental (60Hz) = 49.55, THD= 1.73% Mag (% of Fundamental) 0 100 200 300 500 600 700 800 900 1000 Frequency (Hz)

Figure 5-14 – Total harmonic distortion of the current at the PCC in one of the phases.

5.5 Chapter Summary

This chapter presents the performance evaluation of a microgrid composed of two VSMs, one GFL inverter, and both linear and nonlinear loads. Four simulation scenarios are analyzed. In Scenario 1, the use of G_{cvd} improved the dynamic response and the quality of the injected current. In Scenario 2, the use of G_{cvd} improved the response of the GFL inverter during a voltage sag, and the application of adaptive current-limiting virtual impedance effectively limited the current of the GFM inverter. In Scenario 3, during the parallel operation of two GFM inverters, the use of DID control enhanced their dynamic performance. Scenario 4 evaluates the power quality of the complete microgrid, showing that the voltage and current THD at the PCC are within the limits established by IEEE 519-2014.

CHAPTER VI

6 Conclusions and Future Works

6.1 Conclusions

The transition toward RES has significantly increased the penetration of IBRs in modern power systems, particularly within microgrids. While IBRs offer numerous advantages, their inherent lack of inertia and damping compared to traditional synchronous generators poses challenges to grid stability, especially during transient events. This thesis addressed these challenges by developing a control strategy for VSMs to enhance power dynamic response and stability in microgrids. The primary focus was on improving the inner control loops (current and voltage controllers) of the VSM, which are critical for improving transient performance, disturbance rejection, and interoperability in diverse grid conditions.

In Chapter III, the work focused on improving the inverter-side current control of the VSM. A current controller was developed to achieve high bandwidth and to address issues such as LCL filter resonance and grid disturbances. Experimental tests confirmed its effectiveness in several scenarios. For voltage control, a DID method was introduced to reduce power and current oscillations when the VSM was connected to the grid under different SCR values. It also enhanced the voltage response in islanded mode during load shifts. This approach proved particularly effective in strong grids, where it minimized power overshoot and eliminated subsynchronous oscillations. Experimental tests further validated its effectiveness.

In Chapter IV, the research addressed DC-side control for bidirectional power flow. A strategy was designed to regulate the DC-link voltage and battery current during both grid export and battery charging. Simulations demonstrated smoother power transitions when the DID method was used.

Chapter V validated the proposed VSM converter improvements in a microgrid environment comprising two VSMs, a GFL inverter, linear load, and nonlinear load. The simulated results confirmed that the enhanced control strategies maintained their effectiveness despite dynamic interactions among all components, ensuring smooth coordination between the converters, continuous operation through grid disturbances and power quality compliance despite

harmonic distortion from nonlinear loads.

6.2 Future Works

To continue the work developed in this thesis, it is suggested that the following points be addressed:

- Analyze the interaction between multiple converters operating in parallel to identify the system's stability limits.
- Compare the converter's performance under more advanced control strategies, such as Model Predictive Control (MPC).
- Analyze the dynamic behaviour and interactions of the DC link with the converter.
- Implement power decoupling strategies in order to assess potential performance improvements.
- Analyze converter operation under more realistic grid conditions, including asymmetrical faults and unbalanced conditions.

References

- [1] M. Shadoul, R. Ahshan, R. S. AlAbri, A. Al-Badi, M. Albadi and M. Jamil, "A Comprehensive Review on a Virtual-Synchronous Generator: Topologies, Control Orders and Techniques, Energy Storages, and Applications," *Energies*, vol. 15, no. 22, pp. 1-21, 10 November 2022.
- [2] REN21, "RENEWABLES 2022 GLOBAL STATUS REPORT," 2022. [Online]. Available: https://www.ren21.net/wp-content/uploads/2019/05/GSR2022_Full_Report.pdf. [Accessed 29 March 2023].
- [3] M. A. Hossain, H. R. Pota, M. J. Hossain and A. M. Haruni, "Active power management in a low-voltage islanded microgrid," *International Journal of Electrical Power & Energy Systems*, vol. 98, pp. 36-48, 2018.
- [4] Office of Electricity Delivery and Energy Reliability Smart Grid R&D Program, "Summary Report: 2012 DOE Microgrid Workshop," 30-31 July 2012. [Online]. Available: https://www.energy.gov/sites/prod/files/2012%20Microgrid%20Workshop%20R eport%2009102012.pdf. [Accessed 31 January 2023].
- [5] M. Khatibi, S. Ahmed and N. Kang, "Multi-Mode Operation and Control of a Z-Source Virtual Synchronous Generator in PV Systems," *IEEE Access*, vol. 9, pp. 53003-53012, 2021.
- [6] J. G. d. Matos, Controle de Potência em Microrredes CA Isoladas com Aerogeradores e Bancos de Baterias Distribuídos (PhD thesis), São Luís: UFMA, 2014.
- [7] Agência Nacional de Energia Elétrica ANEEL, "Procedimentos de Distribuição de Energia Elétrica no Sistema Elétrico Nacional PRODIST Módulo 8 -

- Qualidade da Energia Elétrica," 03 August 2020. [Online]. Available: http://www.aneel.gov.br/modulo-8. [Accessed 08 May 2023].
- [8] IEEE, 2030.7-2017 IEEE Standard for the Specification of Microgrid Controllers, IEEE, 2018.
- [9] U. Tamrakar, D. Shrestha, M. Maharjan, B. P. Bhattarai, T. M. Hansen and R. Tonkoski, "Virtual Inertia: Current Trends and Future Directions," *Applied Sciences MDPI*, vol. 7, no. 7, p. 29, 2017.
- [10] B. Kroposki, B. Johnson, Y. Zhang, V. Gevorgian, P. Denholm, B.-M. Hodge and B. Hannegan, "Achieving a 100% Renewable Grid: Operating Electric Power Systems with Extremely High Levels of Variable Renewable Energy," *IEEE Power and Energy Magazine*, vol. 15, no. 2, p. 13, 2017.
- [11] M. M. Hussein, T. Senjyu, M. Orabi, . M. A. A. Wahab and M. M. Hamada, "Control of a Stand-Alone Variable Speed Wind Energy," *applied sciences*, vol. 3, no. 2, p. 20, 2013.
- [12] R. Yan, T. K. Saha, N. Modi, N.-A. Masood and M. Mosadeghy, "The combined effects of high penetration of wind and PV on power system frequency response," *applied energy*, vol. 145, p. 11, 2015.
- [13] G. Rajendran, R. Raute and C. Caruana, "A Comprehensive Review of Solar PV Integration with Smart-Grids: Challenges, Standards, and Grid Codes," *Energies*, vol. 18, no. 2221, 27 April 2025.
- [14] H. R. Pota, The Essentials of Power System Dynamics and Control, Springer, 2018.
- [15] Nahid-Al-Masood, M. N. H. Shazon, H. M. Ahmed and F. Hasan, "Assessing the Risk of Blackout in a Low Inertia Power System and a Possible Countermeasure," in *IEEE Innovative Smart Grid Technologies Asia (ISGT Asia)*, 2021.

- [16] nationalgrid ESO, "Interim report into the low frequency demand disconnection (LFDD) following Generator Trips and Frequency Excursion on 9 Aug 2019," 2019.
- [17] J. Rocabert, A. Luna, F. Blaabjerg and P. Rodríguez, "Control of Power Converters in AC Microgrids," *IEEE TRANSACTIONS ON POWER ELECTRONICS*, vol. 27, pp. 4734-4749, November 2012.
- [18] B. Wen, D. Boroyevich, R. Burgos, P. Mattavelli and Z. Shen, "Analysis of D-Q Small-Signal Impedance of Grid-Tied Inverters," *IEEE Transactions on Power Electronics*, vol. 31, no. 1, pp. 675-687, January 2016.
- [19] D. Dong, B. Wen, D. Boroyevich, P. Mattavelli and Y. Xue, "Analysis of Phase-Locked Loop Low-Frequency Stability in Three-Phase Grid-Connected Power Converters Considering Impedance Interactions," *IEEE Transactions on Industrial Electronics*, vol. 62, no. 1, pp. 310-321, January 2015.
- [20] NERC, "Grid forming technology: Bulk power system reliability considerations," North American Electric Reliability Corporation (NERC), Atlanta, USA, 2021.
- [21] R. Rosso, X. Wang, M. Liserre, X. Lu and S. Engelken, "Grid-Forming Converters: Control Approaches, Grid-Synchronization, and Future Trends—A Review," *IEEE Open Journal of Industry Applications*, vol. 2, pp. 93-109, 2021.
- [22] M. Chandorkar, D. Divan and R. Adapa, "Control of Parallel Connected Inverters in Standalone AC Supply Systems," *IEEE Transactions on Industry Applications*, vol. 29, no. 1, pp. 136-143, January/February 1993.
- [23] S. D'Arco and J. A. Suul, "Virtual synchronous machines Classification of implementations and analysis of equivalence to droop controllers for microgrids," in *2013 IEEE Grenoble Conference*, Grenoble, 2013.
- [24] R. Heydari, M. Savagheb and F. Blaabjerg, "Virtual inertia operation of

- renewables," in *Control of Power Electronic Converters and Systems*, vol. 3, Academic Press, 2021, pp. 523-540.
- [25] Y. Tian, X. Xu, Y. Wang, Z. Li, Z. Zhang and Y. Gao, "Full-State Feedback Power Decoupling Control for Grid Forming Converter With Improved Stability and Inertia Response," *IEEE Transactions On Power Electronics*, vol. 40, no. 2, pp. 2930-2942, February 2025.
- [26] C. A. P. R., J. R. Pinheiro and M. Mezaroba, "Controle de um Conversor CC-CA para Conexão à Rede com Emulação de Máquina Síncrona," *Eletrônica de Potência*, vol. 24, no. 4, pp. 470-481, December 2019.
- [27] X. Meng, J. Liu and Z. Liu, "A Generalized Droop Control for Grid-Supporting Inverter Based on Comparison Between Traditional Droop Control and Virtual Synchronous Generator Control," *IEEE Transactions on Power Electronics*, vol. 34, no. 6, pp. 5416-5438, June 2019.
- [28] X. Zhao, P. G. Thakurta and D. Flynn, "Grid-forming requirements based on stability assessment for 100% converter-based Irish power system," *IET Renewable Power Generation*, vol. 16, no. 3, pp. 447-458, November 2022.
- [29] F. Zhao, T. Zhu, L. Harnefors, B. Fan, H. Wu, Z. Zhou, Y. Sun and X. Wang, "Closed-Form Solutions for Grid-Forming Converters: A Design-Oriented Study," *IEEE Open Journal of Power Electronics*, vol. 5, pp. 186-200, January 2024.
- [30] F. Zhao, X. Wang and T. Zhu, "Power Dynamic Decoupling Control of Grid-Forming Converter in Stiff Grid," *IEEE Transactions On Power Electronics*, vol. 37, no. 8, pp. 9073-9088, August 2022.
- [31] L. Zhang, L. Harnefors and H.-P. Nee, "Power-Synchronization Control of Grid-Connected Voltage-Source Converters," *IEEE Transactions on Power Systems*, vol. 25, no. 2, pp. 809-820, May 2010.

- [32] M. Colombino, D. Groß, J.-S. Brouillon and F. Dorfler, "Global Phase and Magnitude Synchronization of Coupled Oscillators With Application to the Control of Grid-Forming Power Inverters," *IEEE Transactions on automatic control*, vol. 64, no. 11, pp. 4496-4511, November 2019.
- [33] B. Johnson, M. Rodriguez, M. Sinha and S. Dhople, "Comparison of virtual oscillator and droop control," in *IEEE 18th Workshop on Control and Modeling for Power Electronics (COMPEL)*, Stanford, 2017.
- [34] S. U. Islam and S. Kim, "Comparative Analysis of Sub-Synchronous Oscillations With Various Grid-Forming Control Schemes Under Series-Compensated Line," *IEEE Access*, vol. 12, pp. 132763 132772, August 2024.
- [35] K. R. Vasudevan, V. K. Ramachandaramurthy, T. S. Babu and A. Pouryekta, "Synchronverter: A Comprehensive Review of Modifications, Stability Assessment, Applications and Future Perspectives," *IEEE Access*, vol. 8, pp. 131565 131589, 17 July 2020.
- [36] Q.-C. Zhong and G. Weiss, "Synchronverters: Inverters That Mimic Synchronous Generators," *IEEE Transactions on Industrial Electronics*, vol. 58, no. 4, pp. 1259-1267, 2011.
- [37] C. A. Busada, S. G. Jorge and J. A. Solsona, "Shaping the Transient Behavior of Synchronverters," *IEEE Transactions on Energy Conversion*, vol. 38, no. 1, pp. 735 738, March 2023.
- [38] B. W. França, E. L. v. Emmerik, J. F. Caldeira and M. Aredes, "Sliding Droop Control For Distributed Generation In Microgrids," *Eletrônica de Potência*, vol. 22, no. 4, pp. 429-439, December 2017.
- [39] W. Zhang, A. Tarraso, J. Rocabert, A. Luna, J. I. Candela and P. Rodriguez, "Frequency Support Properties of the Synchronous Power Control for Grid-Connected Converters," *IEEE Transactions on Industry Applications*, vol. 55, no.

- 5, pp. 5178 5189, September-October 2019.
- [40] A. Tarrasó, C. Verdugo, N. B. Lai, J. I. Candela and P. Rodriguez, "Synchronous Power Controller for Distributed Generation Units," in *IEEE Energy Conversion Congress and Exposition (ECCE)*, Baltimore, 2019.
- [41] W. Zhang, A. M. Cantarellas, J. Rocabert, A. Luna and P. Rodriguez, "Synchronous Power Controller With Flexible Droop Characteristics for Renewable Power Generation Systems," *IEEE Transactions on Sustainable Energy*, vol. 7, no. 4, pp. 1572 1582, October 2016.
- [42] H.-P. Beck and R. Hesse, "Virtual synchronous machine," in *9th International Conference on Electrical Power Quality and Utilisation*, 2007.
- [43] B. Muftau and M. Fazeli, "The Role of Virtual Synchronous Machines in Future Power Systems: A Review and Future Trends," *Electric Power Systems Research*, vol. 206, Maio 2022.
- Y. Chen, R. Hesse, D. Turschner and H.-P. Beck, "Improving the Grid Power Quality Using Virtual Synchronous Machines," in *International Conference on Power Engineering, Energy and Electrical Drives*, Málaga, 2011.
- [45] Y. Chen, R. Hesse and D. T.-P. Beck, "Comparison of methods for implementing virtual synchronous machine on inverters," in *International Conference on Renewable Energies and Power Quality*, Santiago de Compostela, 2012.
- [46] Q.-C. Zhong and G. Weiss, "Static Synchronous Generators for Distributed Generation and Renewable Energy," in *IEEE/PES Power Systems Conference and Exposition*, Seattle, 2009.
- [47] Q.-C. Zhong, P.-L. Nguyen, Z. Ma and W. Sheng, "Self-Synchronized Synchronverters: Inverters Without a Dedicated Synchronization Unit," *IEEE Transactions on Power Electronics*, vol. 29, no. 2, pp. 617-630, Fevereiro 2014.

- [48] Z. Kustanovich, S. Shivratri, H. Yin, F. Reissner and G. Weiss, "Synchronverters With Fast Current Loops," *IEEE TRANSACTIONS ON INDUSTRIAL ELECTRONICS*, vol. 70, no. 11, pp. 11357-11367, Novembro 2023.
- [49] S. Dong and Y. C. Chen, "Adjusting Synchronverter Dynamic Response Speed via Damping Correction Loop," *IEEE Transactions on Energy Conversion*, vol. 32, no. 2, pp. 608-619, Junho 2017.
- [50] Y. Hirase, K. Abe, K. Sugimoto and Y. Shindo, "A Grid-Connected Inverter with Virtual Synchronous Generator Model of Algebraic Type," *Electrical Engineering in Japan*, vol. 184, no. 4, 2013.
- [51] K. Sakimoto, Y. Miura and T. Ise, "Stabilization of a power system with a distributed generator by a Virtual Synchronous Generator function," in 8th International Conference on Power Electronics ECCE Asia, Jeju, 2011.
- [52] J. Liu, Y. Miura, H. Bevrani and T. Ise, "Enhanced virtual synchronous generator control for parallel invertes in microgrids," *IEEE Transactions on Smart Grid*, vol. 8, no. 5, pp. 2268-2277, 2017.
- [53] J. Alipoor, Y. Miura and T. Ise, "Stability Assessment and Optimization Methods for Microgrid With Multiple VSG Units," *IEEE Transactions on Smart Grid*, vol. 9, no. 2, pp. 1462-1471, Março 2018.
- [54] P. Rodriguez, I. Candela and A. Luna, "Control of PV generation systems using the synchronous power controller," in *2013 IEEE Energy Conversion Congress and Exposition*, Denver, 2013.
- [55] A. T. Martínez, Virtually Synchronous Power Plant Control (Tese de Doutorado), Barcelona: DEE-UPC, 2022.
- [56] W. Zhang, D. Remon and P. Rodriguez, "Frequency support characteristics of gridinteractive power converters based on the synchronous power controller," *IET*

Renewable Power Generation, vol. 11, no. 4, pp. 470-479, Março 2017.

- [57] W. Zhang, D. Remon, I. Candela, A. Luna and P. Rodriguez, "Grid-connected Converters with Virtual Electromechanical Characteristics: Experimental Verification," *CSEE JOURNAL OF POWER AND ENERGY SYSTEMS*, vol. 3, no. 3, pp. 286-295, Setembro 2017.
- [58] W. Zhang, D. Remon, A. Mir, A. Luna, J. Rocabert, I. Candela and P. Rodriguez, "Comparison of different power loop controllers for synchronous power controlled grid-interactive converters," in *IEEE Energy Conversion Congress and Exposition* (ECCE), Montreal, 2015.
- [59] H. Bevrani, T. Ise and Y. Miura, "Virtual synchronous generators: A survey and new perspectives," *International Journal of Electrical Power & Energy Systems*, vol. 54, pp. 244-254, Janeiro 2014.
- [60] M. v. Wesenbeeck, S. d. Haan, P. Varela and K. Visscher, "Grid tied converter with virtual kinetic storage," in 2009 IEEE Bucharest PowerTech, Bucareste, 2009.
- [61] V. Karapanos, Z. Yuan, S. d. Haan and K. Visscher, "A Control Algorithm for the Coordination of Multiple Virtual Synchronous Generator Units," in *Proceedings* of the IEEE Powertech conference, Trondheim, 2011.
- [62] J. M. Guerrero, L. G. d. Vicuña, J. Matas, M. Castilla and J. Miret, "Output Impedance Design of Parallel-Connected UPS Inverters With Wireless Load-Sharing Control," *IEEE Transactions On Industrial Electronics*, vol. 52, no. 4, pp. 1126-1135, August 2005.
- [63] Y. Zhu, F. Zhuo, F. Wang, B. Liu and Y. Zhao, "A Wireless Load Sharing Strategy for Islanded Microgrid Based on Feeder Current Sensing," *IEEE Transactions On Power Electronics*, vol. 30, no. 12, pp. 6706-6719, December 2015.

- [64] X. Wang, Y. W. Li, F. Blaabjerg and P. C. Loh, "Virtual-Impedance-Based Control for Voltage-Source and Current-Source Converters," *IEEE Transactions On Power Electronics*, vol. 30, no. 12, pp. 7019-7037, December 2015.
- [65] J. He and Y. W. Li, "Analysis and design of interfacing inverter output virtual impedance in a low voltage microgrid," in 2010 IEEE Energy Conversion Congress and Exposition, Atlanta, 2010.
- T. Qoria, F. Gruson, F. Colas, G. Denis, T. Prevost and X. Guillaud, "Critical Clearing Time Determination and Enhancement of Grid-Forming Converters Embedding Virtual Impedance as Current Limitation Algorithm," *IEEE Journal Of Emerging And Selected Topics In Power Electronics*, vol. 8, no. 2, pp. 1050-1061, June 2020.
- [67] X. Wang, F. Blaabjerg and Z. Chen, "Autonomous Control of Inverter-Interfaced Distributed Generation Units for Harmonic Current Filtering and Resonance Damping in an Islanded Microgrid," *IEEE Transactions on Industry Applications*, vol. 50, no. 1, pp. 452-461, January-February 2014.
- [68] Z. Li, J. Hu and K. W. Chan, "A New Current Limiting and Overload Protection Scheme for Distributed Inverters in Microgrids Under Grid Faults," *IEEE Transactions on Industry Applications*, vol. 57, no. 6, pp. 6362 6374, November-December 2021.
- [69] Y. Yu, S. K. Chaudhary, G. D. A. Tinajero, L. Xu, J. C. Vasquez and J. M. Guerrero, "Active Damping for Dynamic Improvement of Multiple Grid-Tied Virtual Synchronous Generators," *IEEE Transactions on Industrial Electronics*, vol. 71, no. 4, pp. 3673-3683, April 2024.
- [70] Y. Yang, J. Xu, C. Li, W. Zhang, Q. Wu, M. Wen and F. Blaabjerg, "A New Virtual Inductance Control Method for Frequency Stabilization of Grid-Forming Virtual Synchronous Generators," *IEEE Transactions on Industrial Electronics*, vol. 70,

- no. 1, pp. 441-451, January 2023.
- [71] F. Zhao, X. Wang and T. Zhu, "Low-Frequency Passivity-Based Analysis and Damping of Power-Synchronization Controlled Grid-Forming Inverter," *IEEE Journal Of Emerging And Selected Topics In Power Electronics*, vol. 11, no. 2, pp. 1542-1554, April 2023.
- [72] G. N. Baltas, N. B. Lai, L. Marin, A. Tarrasó and P. Rodriguez, "Grid-Forming Power Converters Tuned Through Artificial Intelligence to Damp Subsynchronous Interactions in Electrical Grids," *IEEE Access*, vol. 8, pp. 93369-93379, 2020.
- [73] P. Rodríguez, C. Citro, J. I. Candela, J. Rocabert and A. Luna, "Flexible Grid Connection and Islanding of SPC-Based PV Power Converters," *IEEE Transactions on Industry Applications*, vol. 54, no. 3, pp. 2690 2702, May-June 2018.
- [74] Z. Shuai, W. Huang, Z. J. Shen, A. Luo and Z. Tian, "Active Power Oscillation and Suppression Techniques Between Two Parallel Synchronverters During Load Fluctuations," *IEEE Transactions On Power Electronics*, vol. 35, no. 4, pp. 4127-4142, April 2020.
- [75] H. Yin, Z. Kustanovich, J. Lin and G. Weiss, "Synchronverters With Damper Windings to Attenuate Power Oscillations in Grids," *IEEE Journal Of Emerging And Selected Topics In Industrial Electronics*, vol. 5, no. 4, pp. 1376-1387, October 2024.
- [76] H. Deng, J. Fang, Y. Qi, Y. Tang and V. Debusschere, "A Generic Voltage Control for Grid-Forming Converters With Improved Power Loop Dynamics," *IEEE Transactions On Industrial Electronics*, vol. 70, no. 4, pp. 3933-3943, April 2023.
- [77] L. Zhao, X. Wang and Z. Jin, "Impedance-based damping effect analysis for the inner loop of grid-forming VSCs," in 22nd Wind and Solar Integration Workshop (WIW 2023), Copenhagen, 2023.

- [78] X. Wang, M. G. Taul, H. Wu, Y. Liao, F. Blaabjerg and L. Harnefors, "Grid-Synchronization Stability of Converter-Based Resources—An Overview," *IEEE Open Journal of Industry Applications*, vol. 1, pp. 115-134, 31 August 2020.
- [79] Y. Liao, X. Wang, F. Liu, K. Xin and Y. Liu, "Sub-Synchronous Control Interaction in Grid-Forming VSCs with Droop Control," in *4th IEEE Workshop on the Electronic Grid (eGRID)*, Xiamen, 2019.
- [80] R. Teodorescu, M. Liserre and P. Rodríguez, Grid Converters for Photovoltaic and Wind Power Systems, Wiley-IEEE press, 2011, p. 398.
- [81] L. Liu, J. Xu, J. Ye and A. Shen, "Passivity Enhancement and Grid-Current Distortion Mitigation for Inverter-Side Current Controlled LCL-Type Grid-Connected Inverters," *IEEE Access*, vol. 12, pp. 66505-66515, 17 May 2024.
- [82] W. Wu, Y. Zhang, F. Blaabjerg and H. S.-H. Chung, "A New Type of Three-Phase Asymmetric-LCL Power Filter for Grid-Tied Voltage Source Inverter With Step-Up Transformer," *IEEE Transactions On Industrial Electronics*, vol. 69, no. 12, pp. 11936-11945, December 2022.
- [83] X. Ruan, X. Wang, D. Pan, D. Yang, W. Li and C. Bao, Control Techniques for LCL-Type Grid-Connected Inverters, Singapore: Springer Singapore, 2018.
- [84] G. C. Goodwin, S. F. Graebe and M. E. Salgado, CONTROL SYSTEM DESIGN, Upper Saddle River: Prentice Hall, 2000.
- [85] A. Reznik, M. G. Simões, A. Al-Durra and S. M. Muyeen, "LCL Filter Design and Performance Analysis for Grid-Interconnected Systems," *IEEE TRANSACTIONS ON INDUSTRY APPLICATIONS*, vol. 50, no. 2, pp. 1225-1232, Março/Abril 2014.
- [86] R. Pena-Alzola, M. Liserre, F. Blaabjerg, M. Ordonez and T. Kerekes, "A Self-commissioning Notch Filter for Active Damping in a Three-Phase LCL-Filter-

Based Grid-Tie Converter," *IEEE TRANSACTIONS ON POWER ELECTRONICS*, vol. 29, no. 12, pp. 6754-6761, Dezembro 2014.

- [87] A. G. Alves, L. G. Rolim, R. F. Dias and P. T. Santos, "VSC plug-and-play operation using onlinegrid parameter estimation for PI self-tuning," *IET Power Electronics*, vol. 13, no. 18, pp. 4359-4367, Fevreiro 2020.
- [88] S. Li and H. Lin, "A Capacitor-Current-Feedback Positive Active Damping Control Strategy for LCL-Type Grid-Connected Inverter to Achieve High Robustness," *IEEE Transactions on Power Electronics*, pp. 6462-6474, Junho 2022.
- [89] F. D. Freijedo, A. Vidal, A. G. Yepes, J. M. Guerrero, Ó. López, J. Malvar and J. Doval-Gandoy, "Tuning of Synchronous-Frame PI Current Controllers in Grid-Connected Converters Operating at a Low Sampling Rate by MIMO Root Locus," *IEEE Transactions on Industrial Electronics*, vol. 62, no. 8, pp. 5006-5017, Agosto 2015.
- [90] D. Pan, X. Ruan, C. Bao, W. Li and X. Wang, "Capacitor-Current-Feedback Active Damping With Reduced Computation Delay for Improving Robustness of LCL-Type Grid-Connected Inverter," *IEEE Transactions on Power Electronics*, vol. 29, no. 7, pp. 3414-3427, Julho 2014.
- [91] I. Lorzadeh, H. A. Abyaneh, M. Savaghebi, A. Bakhshai and J. M. Guerrero, "Capacitor Current Feedback-Based Active Resonance Damping Strategies for Digitally-Controlled Inductive-Capacitive-Inductive-Filtered Grid-Connected Inverters," *Energies*, vol. 9, no. 8, pp. 1-32, Agosto 2016.
- [92] S. G. Parker, B. P. McGrath and D. G. Holmes, "Regions of Active Damping Control for LCL Filters," in *IEEE Energy Conversion Congress and Exposition* (ECCE), Raleigh, 2012.
- [93] C. Byrnes, A. Isidori and J. Willems, "Passivity, feedback equivalence, and the

- global stabilization of minimum phase nonlinear systems," *IEEE Transactions on Automatic Control*, vol. 36, no. 11, pp. 1228 1240, November 1991.
- [94] L. Harnefors, L. Zhang and M. Bongiorno, "Frequency-domain passivity-based current controller design," *IET Electric Power Applications*, vol. 1, no. 4, pp. 455-465, Dezembro 2008.
- [95] L. Harnefors, A. G. Yepes, A. Vidal and J. Doval-Gandoy, "Passivity-Based Controller Design of Grid-Connected VSCs for Prevention of Electrical Resonance Instability," *IEEE Transactions On Industrial Electronics*, vol. 62, no. 2, pp. 702-710, Fevereiro 2015.
- [96] F. d. Bosio, L. A. d. S. Ribeiro, F. D. Freijedo, M. Pastorelli and J. M. Guerrero, "Discrete-Time Domain Modeling of Voltage Source Inverters in Standalone Applications: Enhancement of Regulators Performance by Means of Smith Predictor," *IEEE Transactions on Power Electronics*, vol. 32, no. 10, pp. 8100-8114, Outubro 2017.
- [97] L. A. d. S. Ribeiro, F. D. Freijedo, F. d. Bosio, M. S. Lima, J. M. Guerrero and M. Pastorelli, "Full Discrete Modeling, Controller Design, and Sensitivity Analysis for High-Performance Grid-Forming Converters in Islanded Microgrids," *IEEE Transactions on Industry Applications*, vol. 54, no. 6, pp. 6267-6278, November-December 2018.
- [98] G. F. Franklin, J. D. Powell and A. Emami-Naeini, Feedback Control of Dynamic Systems, 6 ed., Prentice-Hall, 2010.
- [99] R. D. Lorenz, ME 547 Design of Computer Control Systems (lecture notes), Madison, Wisconsin: University of Wisconsin-Madison, 2005.
- [100] J. G. d. Matos, F. S. F. e. Silva and L. A. d. S. Ribeiro, "Power Control in AC Isolated Microgrids With Renewable Energy Sources and Energy Storage Systems," *IEEE Transactions on Industrial Electronics*, vol. 62, no. 6, pp. 3490-

3498, June 2015.

- [101] A. D. Paquette and D. M. Divan, "Virtual Impedance Current Limiting for Inverters in Microgrids With Synchronous Generators," *IEEE Transactions On Industry Applications*, vol. 51, no. 2, pp. 1630-1638, March/April 2015.
- [102] B. Fan, T. Liu, F. Zhao, H. Wu and X. Wang, "A Review of Current-Limiting Control of Grid-Forming Inverters Under Symmetrical Disturbances," *IEEE Open Journal of Power Electronics*, vol. 3, pp. 955-969, 07 December 2022.
- [103] M. G. Taul, X. Wang, P. Davari and F. Blaabjerg, "Current Limiting Control with Enhanced Dynamics of Grid-Forming Converters during Fault Conditions," *IEEE Journal of Emerging and Selected Topics in Power Electronics*, vol. 8, no. 2, pp. 1062 1073, June 2020.
- [104] K. Shi, W. Song, H. Ge, P. Xu, Y. Yang and F. Blaabjerg, "Transient Analysis of Microgrids With Parallel Synchronous Generators and Virtual Synchronous Generators," *IEEE Transactions On Energy Conversion*, vol. 35, no. 1, pp. 95-105, March 2020.
- [105] J. J. Grainger and W. D. S. Jr., Power System Analysis, New York: McGraw-Hill, 1994, p. 787.
- [106] IEEE, "IEEE Guide for Planning DC Links Terminating at AC Locations Having Low Short-Circuit Capacities, Standard 1204-1997," IEEE, New York, 1997.
- [107] R. Ottersten, On Control of Back-to-Back Converters and Sensorless Indution Machine Drives (Doctoral Thesis), Göteborg: Chalmers University of Technology, 2003.
- [108] Institute of Electrical and Electronics Engineers, "IEEE Recommended Practice and Requirements for Harmonic Control in Electric Power Systems," New York, 2014.

APPENDIX A

A. Coefficients of the transfer function of $Z_o(s)$

The equivalent of the function $G_i(z)$ in the continuous-time domain is given by (A.1).

$$G_i(s) = \frac{k_1 s + k_2}{k_3 s + k_4} \tag{A.1}$$

The coefficients representing the transfer function of $Z_o(s)$ are presented below:

$$b_7 = CL_1L_2T_d\alpha_Lk_3\tau_L\tau_p$$

$$\begin{split} b_6 &= CL_1L_2T_dk_3\tau_p - CL_2T_dk_3\tau_L\tau_p + CL_1L_2T_d\alpha_Lk_3\tau_L + 2CL_1L_2\alpha_Lk_3\tau_L\tau_p \\ &+ CL_1L_2T_d\alpha_Lk_4\tau_L\tau_p + CL_1R_2T_d\alpha_Lk_3\tau_L\tau_p + CL_2R_1T_d\alpha_Lk_3\tau_L\tau_p \end{split}$$

$$b_{5} = 2CL_{1}L_{2}k_{3}\tau_{p} - CL_{2}T_{d}k_{3}\tau_{L} - CL_{2}T_{d}k_{3}\tau_{p} + 2CL_{2}k_{3}\tau_{L}\tau_{p} + CL_{1}L_{2}T_{d}k_{3} + CL_{1}L_{2}T_{d}k_{4}\tau_{p}$$

$$+ CL_{1}R_{2}T_{d}k_{3}\tau_{p} + CL_{2}R_{1}T_{d}k_{3}\tau_{p} + 2CL_{1}L_{2}\alpha_{L}k_{3}\tau_{L} - CL_{2}T_{d}k_{4}\tau_{L}\tau_{p}$$

$$+ L_{1}T_{d}\alpha_{L}k_{3}\tau_{L}\tau_{p} + L_{2}T_{d}\alpha_{L}k_{3}\tau_{L}\tau_{p} + L_{2}T_{d}\alpha_{L}k_{3}\tau_{L}\tau_{z} + CL_{1}L_{2}T_{d}\alpha_{L}k_{4}\tau_{L}$$

$$+ CL_{1}R_{2}T_{d}\alpha_{L}k_{3}\tau_{L} + CL_{2}R_{1}T_{d}\alpha_{L}k_{3}\tau_{L} + 2CL_{1}L_{2}\alpha_{L}k_{4}\tau_{L}\tau_{p} + 2CL_{1}R_{2}\alpha_{L}k_{3}\tau_{L}\tau_{p}$$

$$+ 2CL_{2}R_{1}\alpha_{L}k_{3}\tau_{p} + CL_{1}R_{2}T_{d}\alpha_{L}k_{4}\tau_{L}\tau_{p} + CL_{2}R_{1}T_{d}\alpha_{L}k_{4}\tau_{L}\tau_{p}$$

$$b_{4} = 2CL_{1}L_{2}k_{3} - CL_{2}T_{d}k_{3} + 2CL_{2}k_{3}\tau_{L} + 2CL_{2}k_{3}\tau_{p} + L_{1}T_{d}k_{3}\tau_{p} + L_{2}T_{d}k_{3}\tau_{p} + L_{2}T_{d}\tau_{z}$$

$$+ 2CL_{1}L_{2}k_{4}\tau_{p} + 2CL_{1}R_{2}k_{3}\tau_{p} + 2CL_{2}R_{1}k_{3}\tau_{p} - CL_{2}T_{d}k_{4}\tau_{L} - CL_{2}T_{d}k_{4}\tau_{p}$$

$$+ L_{1}T_{d}\alpha_{L}k_{3}\tau_{L} + 2L_{2}T_{d}\alpha_{L}k_{3}\tau_{L} + 2CL_{2}k_{4}\tau_{L}\tau_{p} + 2L_{1}\alpha_{L}k_{3}\tau_{L}\tau_{p} + 2\alpha_{L}k_{3}\tau_{L}\tau_{p}$$

$$- 2L_{2}\alpha_{L}k_{3}\tau_{L}\tau_{z} - T_{d}\alpha_{L}k_{1}\tau_{L}\tau_{p} + CL_{1}L_{2}T_{d}k_{4} + CL_{1}R_{2}T_{d}k_{3} + CL_{2}R_{1}T_{d}k_{3}$$

$$+ CL_{1}R_{2}T_{d}k_{4}\tau_{p} + CL_{2}R_{1}T_{d}k_{4}\tau_{p} + 2CL_{1}L_{2}\alpha_{L}k_{4}\tau_{L} + 2CL_{1}R_{2}\alpha_{L}k_{3}\tau_{L}$$

$$+ 2CL_{2}R_{1}\alpha_{L}k_{3}\tau_{L} + L_{1}T_{d}\alpha_{L}k_{4}\tau_{L}\tau_{p} + L_{2}T_{d}\alpha_{L}k_{4}\tau_{L}\tau_{p} + L_{2}T_{d}\alpha_{L}k_{4}\tau_{L}\tau_{z}$$

$$+ R_{1}T_{d}\alpha_{L}k_{3}\tau_{L}\tau_{p} + R_{2}T_{d}\alpha_{L}k_{4}\tau_{L}\tau_{p} + R_{2}T_{d}\alpha_{L}k_{3}\tau_{L}\tau_{z} + CL_{1}R_{2}T_{d}\alpha_{L}k_{4}\tau_{L}$$

$$+ CL_{2}R_{1}T_{d}\alpha_{L}k_{4}\tau_{L} + 2CL_{1}R_{2}\alpha_{L}k_{4}\tau_{L}\tau_{p} + 2CL_{2}R_{1}\alpha_{L}k_{4}\tau_{L}\tau_{p}$$

$$+ CL_{2}R_{1}T_{d}\alpha_{L}k_{4}\tau_{L} + 2CL_{1}R_{2}\alpha_{L}k_{4}\tau_{L}\tau_{p} + 2CL_{2}R_{1}\alpha_{L}k_{4}\tau_{L}\tau_{p}$$

$$b_{3} = 2CL_{2}k_{3} + L_{1}T_{d}k_{3} + 2L_{2}T_{d}k_{3} + 2L_{1}k_{3}\tau_{p} + 2L_{2}k_{3}\tau_{p} - 2L_{2}k_{3}\tau_{z} - T_{d}k_{1}\tau_{p} + 2\alpha_{L}k_{1}\tau_{L}\tau_{p} \\ + 2CL_{L}k_{2}k_{4} + 2CL_{1}R_{2}k_{3} + 2CL_{2}R_{1}k_{3} - CL_{2}T_{d}k_{4} + 2CL_{2}k_{4}\tau_{L} + 2CL_{2}k_{4}\tau_{p} \\ + L_{1}T_{d}k_{4}\tau_{p} + L_{2}T_{d}k_{4}\tau_{p} + L_{2}T_{d}k_{4}\tau_{z} + R_{1}T_{d}k_{3}\tau_{p} + R_{2}T_{d}k_{3}\tau_{z} \\ + 2L_{1}\alpha_{L}k_{3}\tau_{L} - T_{d}\alpha_{L}k_{1}\tau_{L} + 2CL_{1}R_{2}k_{4}\tau_{p} + 2CL_{2}R_{1}k_{4}\tau_{p} + L_{1}T_{d}\alpha_{L}k_{4}\tau_{L} \\ + 2L_{2}T_{d}\alpha_{L}k_{4}\tau_{L} + R_{1}T_{d}\alpha_{L}k_{3}\tau_{L} + 2R_{2}T_{d}\alpha_{L}k_{3}\tau_{L} + 2L_{1}\alpha_{L}k_{4}\tau_{L}p + 2L_{2}\alpha_{L}k_{4}\tau_{L}p \\ - 2L_{2}\alpha_{L}k_{4}\tau_{L}\tau_{z} + 2R_{1}\alpha_{L}k_{3}\tau_{L}\tau_{p} + 2R_{2}\alpha_{L}k_{3}\tau_{L}\tau_{p} - 2R_{2}\alpha_{L}k_{3}\tau_{L}\tau_{z} - T_{d}\alpha_{L}k_{2}\tau_{L}\tau_{p} \\ + CL_{1}R_{2}T_{d}k_{4} + CL_{2}R_{1}T_{d}k_{4} + 2CL_{1}R_{2}\alpha_{L}k_{4}\tau_{L} + 2CL_{2}R_{1}\alpha_{L}k_{4}\tau_{L} \\ + R_{1}T_{d}\alpha_{L}k_{4}\tau_{L}\tau_{p} + R_{2}T_{d}\alpha_{L}k_{4}\tau_{L}\tau_{p} + R_{2}T_{d}\alpha_{L}k_{4}\tau_{L}\tau_{p} \\ + 2L_{2}k_{4}\tau_{p} - 2L_{2}k_{4}\tau_{z} + 2R_{1}k_{3}\tau_{p} + 2R_{2}k_{3}\tau_{p} - 2R_{2}k_{3}\tau_{z} - T_{d}k_{2}\tau_{p} + 2\alpha_{L}k_{4}\tau_{p} \\ + 2\alpha_{L}k_{2}\tau_{L}\tau_{p} + 2CL_{1}R_{2}k_{4} + 2CL_{2}R_{1}k_{4} + R_{1}T_{d}k_{3} + 2R_{2}T_{d}k_{3} + 2L_{1}k_{4}\tau_{p} \\ + 2\alpha_{L}k_{2}\tau_{L}\tau_{p} + 2CL_{1}R_{2}k_{4} + 2CL_{2}R_{1}k_{4} + R_{1}T_{d}k_{4}\tau_{p} + R_{2}T_{d}k_{3}\tau_{p} + 2R_{2}k_{4}\tau_{p} \\ + 2\alpha_{L}k_{2}\tau_{L}\tau_{p} + 2CL_{1}R_{2}k_{4} + 2CL_{2}R_{1}k_{4} + R_{1}T_{d}k_{4}\tau_{p} + R_{2}T_{d}k_{4}\tau_{p} + 2R_{2}k_{d}k_{4}\tau_{p} \\ + 2R_{1}\alpha_{L}k_{4}\tau_{L} + 2R_{1}\alpha_{L}k_{3}\tau_{L} - T_{d}\alpha_{L}k_{2}\tau_{L} + R_{1}T_{d}\alpha_{L}k_{4}\tau_{L} + 2R_{2}T_{d}k_{4}\tau_{L} \\ + 2R_{1}\alpha_{L}k_{4}\tau_{L}\tau_{p} + 2R_{2}\alpha_{L}k_{4}\tau_{L}\tau_{p} - 2R_{2}\alpha_{L}k_{4}\tau_{L}\tau_{p} \\ - 2R_{2}k_{4}\tau_{z} + 2\alpha_{L}k_{2}\tau_{L} + 2R_{1}\alpha_{L}k_{3}\tau_{L}\tau_{p} + 2CL_{1}\alpha_{L}k_{3}\tau_{L}\tau_{p} + CL_{1}T_{d}\alpha_{L}k_{4}\tau_{L}\tau_{p} \\ + 2R_{1}\alpha_{L}k_{3}\tau_{L}\tau_{p} + CT_{d}k_{3}\tau_{L}\tau_{p} + 2CL_{1}\alpha_{L}k_{3}\tau_{L}\tau_{p} + CL_{1}T_{d}\alpha_{L}k_{4}\tau_{L}\tau_{p} \\ + 2R_{1}\alpha_{L}k_{3}\tau_{L} + 2CL_{1}\alpha_{$$

$$\begin{aligned} a_2 &= \ 2Ck_3 + 2T_dk_3 + 2k_3\tau_p - 2k_3\tau_z + 2CL_1k_4 + 2CR_1k_3 - CT_dk_4 + 2Ck_4\tau_L + 2Ck_4\tau_p \\ &+ T_dk_4\tau_p + T_dk_4\tau_z + 2\alpha_Lk_4\tau_L\tau_p - 2\alpha_Lk_4\tau_L\tau_z + CR_1T_dk_4 + 2CR_1k_4\tau_p \\ &+ 2T_d\alpha_Lk_4\tau_L + 2CR_1\alpha_Lk_4\tau_L \end{aligned}$$

$$a_1 &= 2Ck_4 + 2T_dk_4 + 2k_4\tau_p - 2k_4\tau_z + 2CR_1k_4 \end{aligned}$$

APPENDIX B

B. Experimental setup

For the acquisition of the experimental results, it was necessary to assemble a test bench containing four inverters and their respective filters, although only one was used in this phase of the research. The schematic diagram of the experimental setup is shown in Figure B-1, and its components are listed below:

- 1. Danfoss inverters, model FC 302
- 2. dSPACE MicroLabBox for controlling the inverters
- 3. Bi-directional Power Supply, model EA-PSB 10750-120 4U
- 4. Inductors and capacitors forming the LCL filter
- 5. Circuit breakers and contactors (controlled by dSPACE)
- 6. Inductors simulating the line impedance
- 7. Chroma 61830 grid emulator for simulating the grid
- 8. An isolation transformer for direct connection of the inverter to the grid (if needed)
- 9. Linear loads

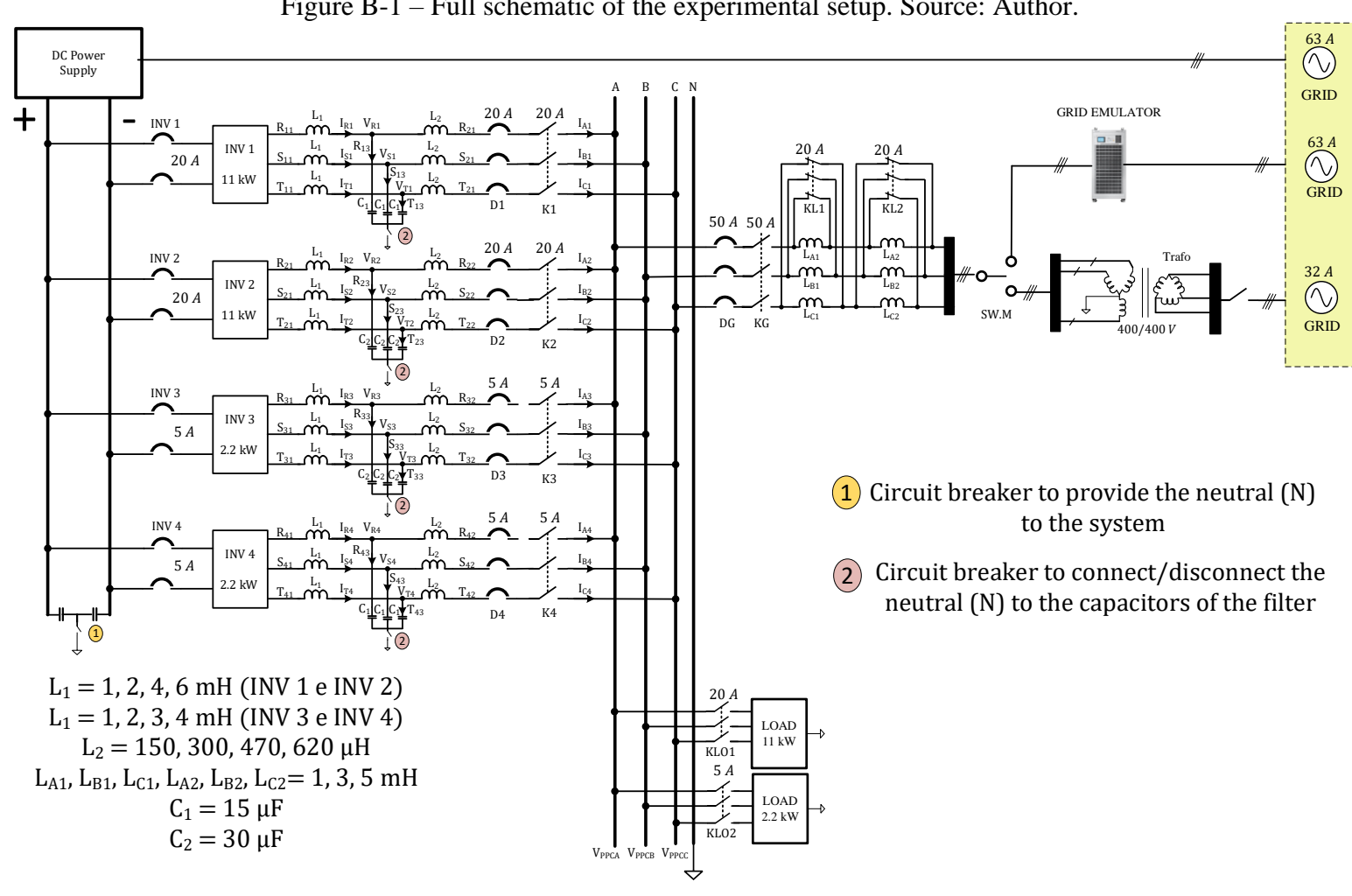
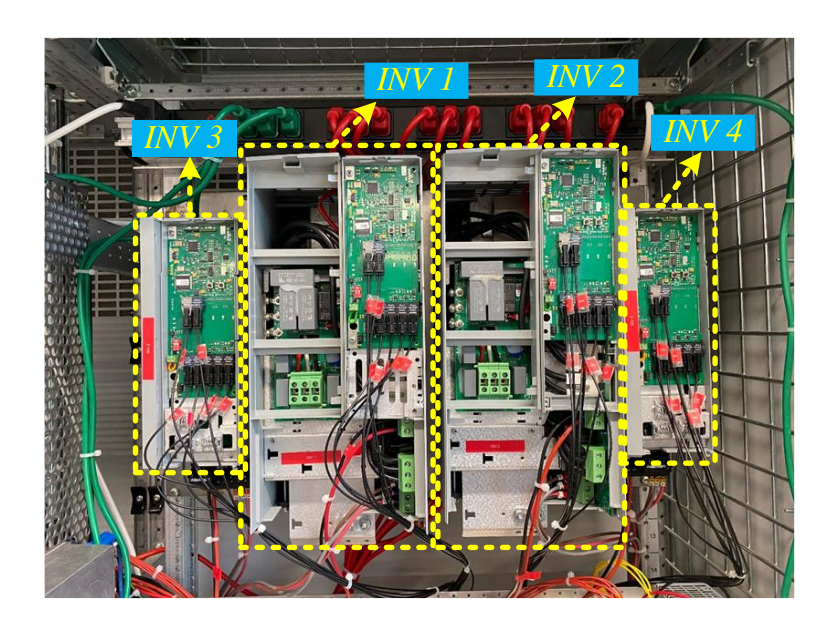


Figure B-1 – Full schematic of the experimental setup. Source: Author.

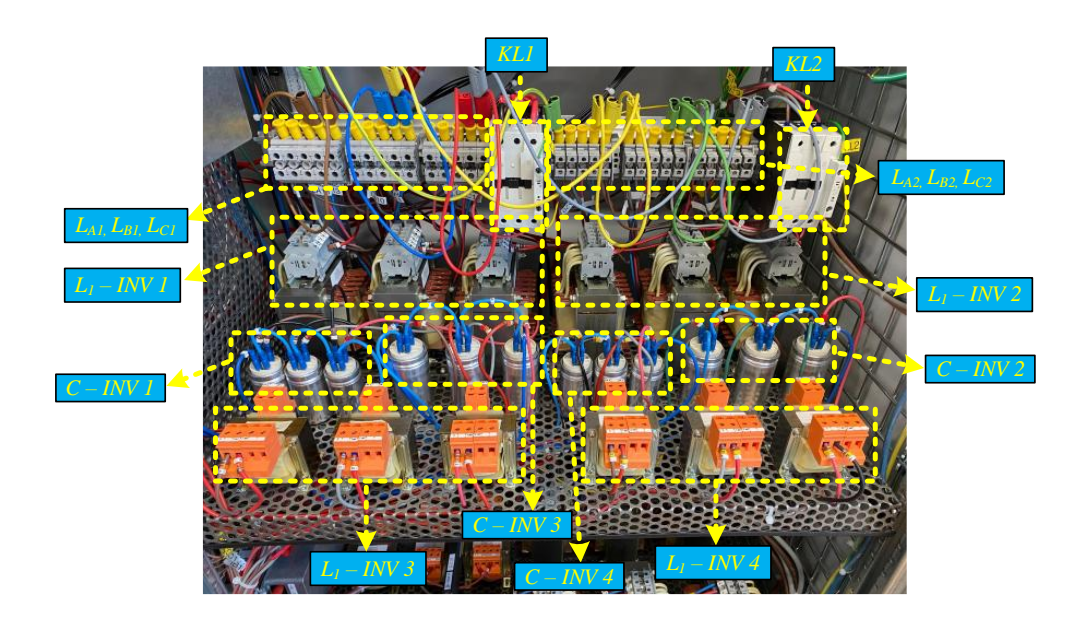
Some photos of the experimental setup are shown below:

Figure B-2 – Inverters used in the experimental setup.



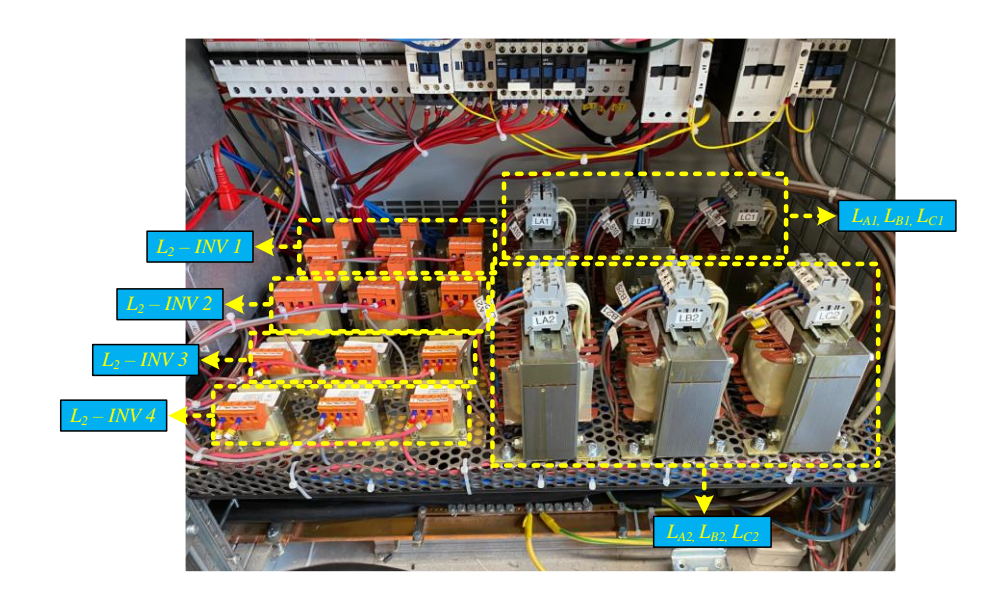
Source: Author.

Figure B-3 – L_1 , $\mathcal C$ of the LCL filter and grid impedance connectors.



Source: Author.

Figure B-4 – L_2 and grid impedance inductors.



Source: Author.

Figure B-5 – DC voltage source.



Source: Author.